COMPUTATIONAL SIMULATIONS OF FLOW PAST A ROTATING ARRANGEMENT OF THREE CYLINDERS USING HYBRID TURBULENCE MODELS

A Thesis
Submitted to the Graduate Faculty
of the
North Dakota State University
of Agriculture and Applied Science

By

Nick Leonard Thomas

In Partial Fulfillment of the Requirements
for the Degree of
MASTER OF SCIENCE

Major Department:
Mechanical Engineering

November 2020

Fargo, North Dakota

NORTH DAKOTA STATE UNIVERSITY

Graduate School

Title

COMPUTATIONAL SIMULATIONS OF FLOW PAST A ROTATING ARRANGEMENT OF THREE CYLINDERS USING HYBRID TURBULENCE MODELS

By

Nick Leonard Thomas

The supervisory committee certifies that this thesis complies with North Dakota State University's regulations and meets the accepted standards for the degree of

MASTER OF SCIENCE

SUPERVISORY COMMITTEE:

Dr. Y. Bora Suzen
Chair

Dr. Jordi Estevadeordal

Dr. Yan Zhang

Dr. Om Yadav

Dr. Forrest Ames

Approved:

11/20/20
Date

Dr. Alan Kallmeyer
Department Chair

ABSTRACT

Over the past 25 years, advances in the field of turbulence modeling have been made in an effort to resolve more scales, preserving unsteadiness within a flow. In this research two hybrid models, Scale-Adaptive Simulation (SAS) and Stress-Blended Eddy Simulation (SBES) are implemented in solving the highly unsteady flow over a rotating arrangement of three cylinders. Results are compared to those from wind tunnel experiments carried out at North Dakota State University. Both models show close agreement with first and second order turbulence quantities, and SBES shows much greater flow structure detail due to its ability to resolve smaller scales. The Strouhal number for the flow is found to be a function of the rotational speed of the arrangement with von Kármán-like structures resulting from each cylinder's wake over a full rotation. SAS shows a constant computational cost as Re increases while the SBES's computational cost increases relatively linearly.

ACKNOWLEDGEMENTS

First, I would like to thank my advisor Dr. Y. Bora Suzen for his guidance on this research and for introducing me to the world of CFD. His assistance has been invaluable over the past several years.

I would like to thank Dr. Jordi Estevadeordal, Dr. Yan Zhang, Dr. Om Yadav, and Dr. Forrest Ames for taking the time to be on my graduate committee.

I would also like to thank Al Habib Ullah and Charles Fabijanic for their work on the flow experiments used in validation of these simulations as well as their insights throughout this research.

Finally, I would like to thank my parents for their constant love and support throughout the years.

TABLE OF CONTENTS

ABSTRACT iii

ACKNOWLEDGEMENTS iv

LIST OF TABLES viii

LIST OF FIGURES ix

LIST OF ABBREVIATIONS xiii

LIST OF SYMBOLS xiv

1. INTRODUCTION AND RESEARCH OBJECTIVES 1

2. REVIEW OF TURBULENCE AND TRANSITION 3

2.1. Turbulent Flow 3

2.1.1. Introduction to Turbulent Flow 3

2.1.2. Turbulent Scales 3

2.2. Laminar to Turbulent Transition 4

2.2.1. Modes of Transition 6

2.2.2. Factors Affecting Transition 7

3. TURBULENCE MODELING 9

3.1. Governing Equations of Fluid Motion 9

3.2. Reynolds-Averaging 11

3.3. Reynolds-averaged Navier-Stokes Equations 13

3.4. Filtering and the Large Eddy Simulation Decomposition 15

3.5. Large Eddy Simulation Equations 16

4. TURBULENCE MODELS 19

4.1. Direct Numerical Simulation 19

4.2. Reynolds-averaged Navier-Stokes Models 20

4.2.1. k-ϵ Model 21

4.2.2. k-ω Model 22

4.2.3. Shear Stress Transport Model . . . 23
4.3. Large Eddy Simulation Models . . . 24
4.3.1. Wall-Adapted Local Eddy Viscosity Model . . . 25
4.4. Hybrid Models . . . 26
4.4.1. Scale-Adaptive Simulation . . . 26
4.4.2. Detached Eddy Simulation . . . 27
4.4.3. Delayed and Shielded Detached Eddy Simulation . . . 28
4.4.4. Stress-Blended Eddy Simulation . . . 29
5. FLOW EXPERIMENTS . . . 30
5.1. Wind Tunnel Characteristics . . . 30
5.2. Three-Cylinder Experiments . . . 31
6. CFD COMPUTATION METHODS . . . 33
6.1. Software . . . 33
6.2. Hardware . . . 33
6.3. Fluid Domain Geometry . . . 33
6.4. Mesh Generation and Refinement . . . 36
6.5. Boundary Conditions and Setup . . . 37
6.5.1. Boundary Conditions . . . 37
6.5.2. Solver and Timestep Options . . . 38
7. RESULTS AND DISCUSSION . . . 39
7.1. Statistical Reynolds Stresses . . . 40
7.1.1. Re=57 . . . 41
7.1.2. Re=858 . . . 43
7.1.3. Re=7150 . . . 45
7.2. Time Averaged Velocity . . . 49
7.2.1. Re=57 . . . 49

7.2.2. Re=858 50
7.2.3. Re=7150 52
7.3. Time Averaged Velocity and Statistical Reynolds Stress Error 53
7.4. Turbulence Intensity 55
7.4.1. Re=57 55
7.4.2. Re=858 56
7.4.3. Re=7150 59
7.5. Lift and Drag 60
7.5.1. Re=57 62
7.5.2. Re=858 62
7.5.3. Re=7150 69
7.6. Vorticity and Flow Structure Analysis 71
7.7. Computational Cost Analysis 80
8. CONCLUSIONS AND FUTURE WORK 83
8.1. Conclusions 83
8.2. Future Work 83
BIBLIOGRAPHY 85

LIST OF TABLES

Table Page

5.1. Hotwire measurement point locations 31

6.1. Mesh parameters 37

6.2. Timesteps used 38

7.1. Freestream velocity values for CFD and PIV 39

7.2. Percent error of average flow properties on an extracted line across the x-axis with lowest the lowest values of $\overline{u}$ and R_{xx} for each combination of Re and f underlined 54

7.3. Strouhal number and time-averaged C_D for each cylinder at Re=57, f=0 Hz 63

7.4. Strouhal number and time-averaged C_D for each cylinder at Re=858, f=25 Hz 66

7.5. Strouhal number and time-averaged C_D for each cylinder at Re=858, f=50 Hz 68

7.6. Strouhal number and time-averaged C_D for each cylinder at Re=7150, f=50 Hz 70

7.7. Kolmogorov length scales 72

7.8. Calculated vs. experimental Strouhal number 72

7.9. Computational cost analysis 81

LIST OF FIGURES

Figure Page

2.1. Richardson energy cascade (P. A. Davidson, 2013) 5

2.2. Turbulent energy spectrum (Sinha, 2013) 5

2.3. Process of natural transition (White, 2006) 6

2.4. Process of separated-flow transition (Zilli et al., 2017) 7

3.1. Illustration of the average and fluctuating quantities for steady (left) and unsteady (right) flows (Hoffmann & Chiang, 2000) 12

4.1. Hierarchy of CFD turbulence models considering resolved vs. modeled structure and computational cost (Xiao & Cinnella, 2019) 19

5.1. FloTek 1440 wind tunnel 30

5.2. Three-cylinder setup (a) geometry and (b) wind tunnel setup (Ullah et al., 2020) 31

5.3. Hotwire measurement locations 32

6.1. Original geometry 34

6.2. Final geometry 35

6.3. Final mesh 36

6.4. Boundary conditions 37

7.1. Statistical Reynolds stresses R_{xx} for Re=57, f=0 Hz using a. PIV, b. SAS, and c. SBES 41

7.2. Statistical Reynolds stresses R_{yy} for Re=57, f=0 Hz using a. PIV, b. SAS, and c. SBES 41

7.3. Statistical Reynolds stresses R_{xy} for Re=57, f=0 Hz using a. PIV, b. SAS, and c. SBES 42

7.4. Statistical Reynolds stresses R_{zz} for Re=57, f=0 Hz using a. SAS, and b. SBES 43

7.5. Statistical Reynolds stresses R_{xx} for Re=858, f=25 Hz using a. PIV, b. SAS, and c. SBES 44

7.6. Statistical Reynolds stresses R_{yy} for Re=858, f=25 Hz using a. PIV, b. SAS, and c. SBES 44

7.7. Statistical Reynolds stresses R_{xy} for Re=858, f=25 Hz using a. PIV, b. SAS, and c. SBES 44

7.8. Statistical Reynolds stresses R_{zz} for Re=858, f=25 Hz using a. SAS, and b. SBES . . . 45

7.9. Statistical Reynolds stresses R_{xx} for Re=858, f=50 Hz using a. PIV, b. SAS, c. SBES, and d. SST 45

7.10. Statistical Reynolds stresses R_{yy} for Re=858, f=50 Hz using a. PIV, b. SAS, c. SBES, and d. SST 46

7.11. Statistical Reynolds stresses R_{xy} for Re=858, f=50 Hz using a. PIV, b. SAS, c. SBES, and d. SST 46

7.12. Statistical Reynolds stresses R_{zz} for Re=858, f=50 Hz using a. SAS, b. SBES, and c. SST 47

7.13. Statistical Reynolds stresses R_{xx} for Re=7150, f=50 Hz using a. PIV, b. SAS, and c. SBES 47

7.14. Statistical Reynolds stresses R_{yy} for Re=7150, f=50 Hz using a. PIV, b. SAS, and c. SBES 48

7.15. Statistical Reynolds stresses R_{xy} for Re=7150, f=50 Hz using a. PIV, b. SAS, and c. SBES 48

7.16. Statistical Reynolds stresses R_{zz} for Re=7150, f=50 Hz using a. SAS, and b. SBES . . 48

7.17. Average velocity $\overline{u}$ for Re=57, f=0 Hz using a. PIV, b. SAS, and c. SBES 49

7.18. Velocity u profile for Re=57, f=0 Hz at downstream distances of a. X=1 and b. X=4 . 49

7.19. Average velocity $\overline{u}$ for Re=858, f=25 Hz using a. PIV, b. SAS, and c. SBES 50

7.20. Velocity u profile for Re=858, f=25 Hz at downstream distances of a. X=1, b. X=4, and c. X=7 51

7.21. Average velocity $\overline{u}$ for Re=858, f=50 Hz using a. PIV, b. SAS, c. SBES, and d. SST . 51

7.22. Velocity u profile for Re=858, f=50 Hz at downstream distances of a. X=1, b. X=4, and c. X=7 52

7.23. Average velocity $\overline{u}$ for Re=7150, f=50 Hz using a. PIV, b. SAS, and c. SBES 52

7.24. Velocity u profile for Re=7150, f=50 Hz at downstream distances of a. X=1, b. X=4, and c. X=7 53

7.25. R_{xx} along x-axis downstream of the cylindrical arrangement for a. Re=57, f=0 Hz, b. Re=858, f=25 Hz, c. Re=858, f=50 Hz, and d. Re=7150, f=50 Hz 54

7.26. Turbulence intensity (in %) for Re=57, f=0 Hz using a. PIV, b. SAS, and c. SBES . . 56

7.27. Turbulence intensity along x-axis downstream of the cylindrical arrangement for Re=57, f=0 Hz 56

7.28. Turbulence intensity (in %) for Re=858, f=25 Hz using a. PIV, b. SAS, and c. SBES . 57

7.29. Turbulence intensity along x-axis downstream of the cylindrical arrangement for Re=858, f=25 Hz 57

7.30. Turbulence intensity (in %) for Re=858, f=50 Hz using a. PIV, b. SAS, c. SBES, and d. SST 58

7.31. Turbulence intensity along x-axis downstream of the cylindrical arrangement for Re=858, f=50 Hz 58

7.32. Turbulence intensity (in %) for Re=7150, f=50 Hz using a. PIV, b. SAS, and c. SBES 59

7.33. Turbulence intensity along x-axis downstream of the cylindrical arrangement for Re=7150, f=50 Hz 59

7.34. Drag coefficient over a circular cylinder as compiled from various experiments at different Re (White, 2006) 61

7.35. Strouhal numbers as compiled from various experiments at different Re (White, 2006) . 61

7.36. Coefficient of lift for Re=57, f=0 Hz using a. SAS and b. SBES 62

7.37. Coefficient of drag for Re=57, f=0 Hz using a. SAS and b. SBES 63

7.38. Coefficient of lift for Re=858, f=25 Hz using a. SAS and b. SBES 64

7.39. Coefficient of drag for Re=858, f=25 Hz using a. SAS and b. SBES 64

7.40. Cylinder locations throughout rotation cycle 64

7.41. Vorticity Z contours for Re=858, f=25 Hz using a. SAS and b. SBES 65

7.42. Relative freestream adjusted coefficient of drag for Re=858, f=25 Hz using a. SAS and b. SBES 66

7.43. Coefficient of lift for Re=858, f=50 Hz using a. SAS and b. SBES 67

7.44. Coefficient of drag for Re=858, f=50 Hz using a. SAS and b. SBES 67

7.45. Relative freestream adjusted coefficient of drag for Re=858, f=50 Hz using a. SAS and b. SBES 68

7.46. Coefficient of lift for Re=7150, f=50 Hz using a. SAS and b. SBES 69

7.47. Coefficient of drag for Re=7150, f=50 Hz using a. SAS and b. SBES 69

7.48. Relative freestream adjusted coefficient of drag for Re=7150, f=50 Hz using a. SAS and b. SBES 70

7.49. Frequency spectra for Cylinder 3 at Re=7150, f=50 Hz, SBES 71

7.50. Instantaneous spanwise (Z) vorticity frames from $\theta = 0.3°$ to $\theta = 105.1°$ for Re=858, f=50 Hz, and SBES 73

7.51. Instantaneous spanwise (Z) vorticity frames from $\theta = 120.1°$ to $\theta = 224.9°$ for Re=858, f=50 Hz, and SBES 74

7.52. Instantaneous spanwise (Z) vorticity frames from $\theta = 239.9°$ to $\theta = 344.7°$ for Re=858, f=50 Hz, and SBES 75

7.53. Q-Criterion iso-surfaces of $Q = 2$ colored by spanwise velocity for Re=57, f=0 Hz using a. SAS and b. SBES 76

7.54. Q-Criterion iso-surfaces of $Q = 10$ colored by spanwise velocity for Re=858, f=50 Hz using SBES 77

7.55. Q-Criterion iso-surfaces of $Q = 10$ colored by spanwise velocity near the cylinder walls for Re=858, f=50 Hz using SBES a. viewed from the top and b. viewed from the bottom 78

7.56. SDES/SBES blending function for Re=858, f=50 Hz 78

7.57. Q-Criterion iso-surfaces of $Q = 10$ colored by spanwise velocity near the cylinder walls for Re=858, f=50 Hz using SBES 79

7.58. Q-Criterion iso-surfaces of $Q = 10$ colored by spanwise velocity for Re=858, f=50 Hz using SBES 80

7.59. Q-Criterion iso-surfaces of $Q = 10$ colored by spanwise velocity for Re=7150, f=50 Hz using SBES 80

7.60. Computational cost vs. Reynolds number 82

LIST OF ABBREVIATIONS

API	application programming interface
CCAST	Center for Computationally Assisted Science and Technology
CFD	computational fluid dynamics
CPU	central processing unit
DNS	direct numerical simulation
EbFVM	Element based Finite Volume Method
FFT	Fast Fourier Transform
FOV	field-of-view
LES	large eddy simulation
NDSU	North Dakota State University
PIV	particle image velocimetry
RAM	random access memory
RANS	Reynolds-averaged Navier-Stokes
RPM	rotations per minute
SAS	Scale-Adaptive Simulation
SBES	Stress-Blended Eddy Simulation
SST	Shear Stress Transport
URANS	Unsteady Reynolds-averaged Navier-Stokes

LIST OF SYMBOLS

b	cylinder span
c_p	constant pressure specific heat
d	distance to nearest wall node
e	internal energy
$\boldsymbol{g}$	acceleration due to gravity
h	enthalpy
f	frequency
l_m	Prandtl mixing length
ℓ	mean free path
k	turbulent kinetic energy
p	pressure
r	cylinder radius
s	strain-rate tensor
t	time
u	x velocity
u_i	i velocity
v	y velocity
w	z velocity
x	x direction
x_i	i direction
y	y direction
z	z direction

C_{ij} . . . . . cross stresses

C_D . . . . . drag coefficient

C_L . . . . . lift coefficient

CFL . . . . . Courant number

D . . . . . three cylinder arrangement diameter

F_D . . . . . drag force

F_{DDES} . . . . . DDES shielding function

F_L . . . . . lift force

F_{SBES} . . . . . SDES and SBES shielding function

G . . . . . filter function

Kn . . . . . Knudsen number

L . . . . . characteristic length

L_{ij} . . . . . Leonard stresses

L_t . . . . . turbulent length scale

L_{vK} . . . . . von Kármánlength scale

P_k . . . . . viscous turbulence production

Q . . . . . Q-Criterion

R_{ij} . . . . . Reynolds stresses

Re . . . . . Reynolds number

Re_θ . . . . . transition momentum thickness Reynolds number

S . . . . . cylinder spacing ratio

St . . . . . Strouhal number

T . . . . . temperature

TI . . . . . turbulence intensity

$\boldsymbol{U}$ . . . . . velocity

U_∞ . . . . . freestream velocity

V . . . . . volume

X . . . . . streamwise direction

Y . . . . . vertical direction

Z . . . . . spanwise direction

γ . . . . . intermittency

δ_{ij} . . . . . Kronecker delta

ϵ . . . . . eddy dissipation rate

η_k . . . . . Kolmogorov length scale

θ . . . . . phase angle

κ . . . . . thermal conductivity

μ . . . . . dynamic viscosity

μ_b . . . . . bulk viscosity

μ_t . . . . . turbulent (eddy) dynamic viscosity

ν . . . . . kinematic viscosity

ν_t . . . . . turbulent (eddy) kinematic viscosity

ν_{SGS} . . . . . subgrid-scale kinematic viscosity

ξ . . . . . spatial field

ρ . . . . . density

τ . . . . . shear stress

τ_l . . . . . laminar shear stress

τ_t . . . . . turbulent shear stress

τ_k . . . . . Kolmogorov time scale

$\boldsymbol{\tau}_{SGS}$	subgrid-scale shear stress
v_k	Kolmogorov velocity scale
ϕ	dissipative function
ω	specific eddy dissipation rate
$\Delta_{\max}$	maximum cell edge length
Λ	largest turbulent length scale
\$	computational cost

1. INTRODUCTION AND RESEARCH OBJECTIVES

One of the most challenging aspects of computational fluid dynamics (CFD) is accurately solving turbulent flows. A number of strategies have been used to do so, ranging from using an extremely fine grid and resolving all scales of turbulence (Direct Numerical Solution, DNS), to applying averaging to the entire flow and modeling all turbulent scales (Reynolds-averaged Navier-Stokes, RANS), as well as compromises in-between those "extremes" (e.g. Large Eddy Simulation, LES, and hybrid models). In this thesis, two recently developed scale-resolving models (Stress-Adaptive Simulation, SAS and Stress-Blended Eddy Simulation, SBES) are implemented in the simulation of an unsteady flow over three equilaterally spaced cylinders rotating about a common central axis.

Flows over cylinders, arrangements of cylinders, and other bluff bodies are of great interest for engineering and research applications. The present arrangement of three equilaterally spaced cylinders has been studied both experimentally and computationally, but without rotation (Bao et al., 2010; Lam & Cheung, 1988; Tatsuno et al., 1998; Zdravkovich, 1968). These studies have identified flow patterns as a function of cylinder spacing and arrangement angle. For example, at small cylinder spacings the overall flow acts similarly to a blunt body of the arrangement's size while large cylinder spacings results in the individual wakes of the cylinders being represented. Intermediate spacings show a combination of the two effects. PIV has also been performed on this rotating arrangement of cylinders, but this study uses a very large cylinder spacing in comparison to this research (Rostad, 2018).

There are several objectives for this work. First, a greater understanding of the aforementioned scale-resolving models including best practices, limitations, and benefits is desired. While SAS is slightly older and versions of it have existed for ~15 years, SBES is an exciting new development in the world of turbulence modeling, and there is still much to learn about using it practically. Additionally, the flow problem being computed has not been studied computationally with rotation in previous research. In fact, there has been very limited research with such models on highly unsteady flows with rotation or other motion present, a situation that they would be

well-suited for. Finally, insight and characterization of the physics of the present flow problem are desired for future research and possible implementation for applications such as airfoil testing.

2. REVIEW OF TURBULENCE AND TRANSITION

2.1. Turbulent Flow

Fluid flows are often categorized as being within one of two broad categories—laminar or turbulent. Laminar flow is characterized as being smooth and well-ordered with little to no mixing between 'layers' in the flow. In contrast, turbulent flow is random and chaotic in nature, with fluctuations in the flow properties such as velocity and pressure. In reality however, nearly all real flows are turbulent to a degree and often need to be treated as such during analysis.

2.1.1. Introduction to Turbulent Flow

While turbulence is often described as random and chaotic, a more comprehensive definition is more difficult to find. Osborne Reynolds described turbulence as "eddying about in sinuous paths the most indirect possible" as opposed to laminar flow "following one another along lines of motion which lead in the most direct manner to their destination" (Reynolds, 1883). Similar to calling turbulence "random and chaotic", this description is effective intuitively, but lacks in comprehension of a true definition. Another attempt to define turbulence is given by Hinze as "an irregular condition of the flow in which the various quantities show a random variation with time and space coordinates, so that statistically distinct average values can be discerned" (Hinze, 1959). Although these random variations exist, there is a structure to the chaos as well. Frank White describes five separate characteristics of turbulent flows, including fluctuations in flow properties, eddies of a large range of sizes, random variations in flow properties, self-sustaining motion, and strong mixing within the flow (White, 2006).

2.1.2. Turbulent Scales

In White's description of turbulence, he describes eddies as fluid 'packets' intermingling with each other. The behavior of eddies can be informally described as in the famous poem of English meteorologist Lewis Fry Richardson (Richardson, 1922),

> Big whorls have little whorls
> Which feed on their velocity,

And little whorls have lesser whorls

And so on to viscosity.

Eddies exist in a large, continuous range of scales, with larger eddies producing larger random fluctuations of flow properties. Eddies go through a process of stretching and pulling called vortex stretching where increases in the rotational velocity of the eddies accompany decreases in the size, or diameter of the eddies in order to conserve angular momentum. This results in a transfer in kinetic energy from the largest to smallest scales until the smallest scales result in viscous dissipation and is coined the energy cascade, visualized in Figure 2.1 (Pope, 2000). Figure 2.2 shows the turbulent energy spectrum, which displays the distribution of low wave-numbers to high wave-numbers within a flow. The smallest scales possible can be determined using Kolmogorov's universal equilibrium theory, which states that the smallest scales are receiving kinetic energy from larger scales and dissipating viscous heat at an equal rate. Based on this premise, the Kolmogorov length (η_k), time (τ_k), and velocity (υ_k) scales are developed using dimensional analysis to be

$$\eta_k \equiv \left(\frac{\nu^3}{\epsilon}\right)^{\frac{1}{4}}, \tag{2.1a}$$

$$\tau_k \equiv \left(\frac{\nu}{\epsilon}\right)^{\frac{1}{2}}, \text{ and} \tag{2.1b}$$

$$\upsilon_k \equiv (\nu\epsilon)^{\frac{1}{4}}, \tag{2.1c}$$

where the quantities ϵ and ν are the rate of energy transfer and kinematic viscosity, respectively (Wilcox, 2006). As these represent the smallest possible scales for eddies, η_k can be compared to the mean free path, ℓ using the Knudsen number by

$$Kn = \frac{\ell}{\nu}. \tag{2.2}$$

ν is indeed small, but still orders of magnitude larger than ℓ (Tennekes & Lumley, 1972). Thus, a continuum approach is valid for the modeling of turbulence.

2.2. Laminar to Turbulent Transition

Treating a flow as fully turbulent or fully laminar is advantageous in simplification for modeling, but the reality is that many flows undergo a transition from laminar to turbulent flow.

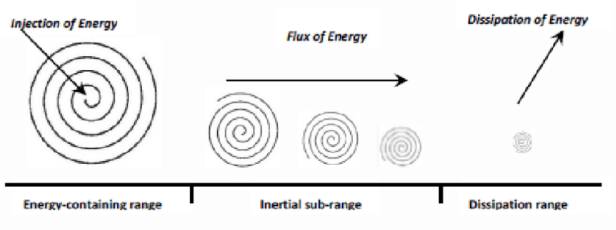

Figure 2.1. Richardson energy cascade (P. A. Davidson, 2013)

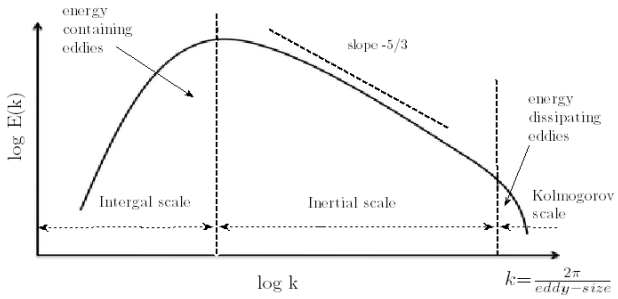

Figure 2.2. Turbulent energy spectrum (Sinha, 2013)

While this transition can be of negligible effect for some flows, it plays a significant role in others. Therefore, understanding the transition within a flow is necessary for effective and accurate modeling.

A good starting point for determining the degree of turbulence within a flow is found using the Reynolds number,

$$Re = \frac{\rho U_\infty L}{\mu}, \tag{2.3}$$

where ρ is density, U_∞ is freestream velocity, L is characteristic length, and μ is dynamic viscosity. The Reynolds number relates the significance of a flow's inertial forces to its viscous forces. While guidelines exist for estimating turbulence of certain types of flows (external flows, pipe flows, etc.) based on the Reynolds number, they are merely guidelines, and vary largely under different conditions. Furthermore, even a flow that is highly turbulent may contain a region of transition before turbulence is achieved.

2.2.1. Modes of Transition

Generally, the transition to turbulence can be categorized in one of three modes—natural transition, bypass transition, or separated-flow transition. Additionally, periodic-unsteady transition can exist in some flows with interaction of wakes between wall boundaries.

2.2.1.1. Natural Transition

Natural transition, as the name implies, is the natural and gradual transition to turbulence that occurs when not accelerated by some external factor. This is often demonstrated as it occurs on a flat plate, seen in Figure 2.3. For the initially laminar flow, the boundary layer grows until a critical value of the Reynolds number based on the momentum thickness is reached. The boundary layer becomes unstable, and 2-D disturbances known as Tollmien-Schlicting waves begin to form. Flow instability continues to grow, resulting in the formation of 3-D eddies and vortices. The eddies and vortices break down into large fluctuations, and then progress to turbulent spots, or arrowhead-shaped "packets" of fluid. Finally, fully turbulent flow is reached, the end of transition (White, 2006).

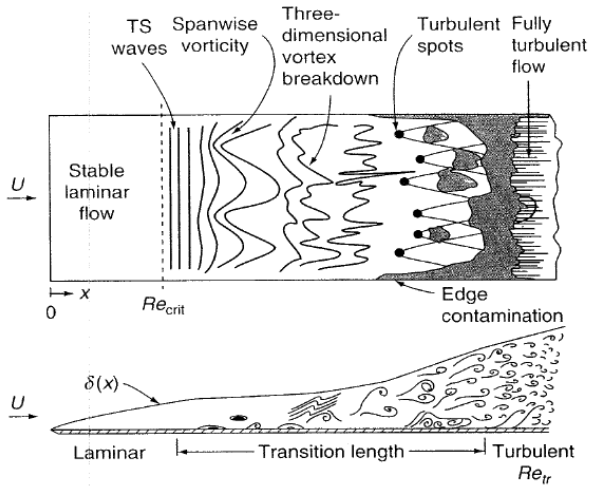

Figure 2.3. Process of natural transition (White, 2006)

2.2.1.2. Bypass Transition

Bypass transition is similar to natural transition, but the early stages (formation of Tollmien-Schlicting waves, initial formation of 3-D vortices) are bypassed due to some external factor. Typ-

ically, factors such as a high surface roughness, noisy freestream, or vibrations within the flow can cause bypass transition (White, 2006).

2.2.1.3. Separated-Flow Transition

Separated-flow transition is common in the flow over bluff bodies such as cylinders as presented in this thesis. When the laminar boundary layer separates from a body, possibly due to a tripping mechanism or adverse pressure gradient, a separation bubble of recirculating flow forms and likely reattaches as turbulent flow (White, 2006). This separation and reattachment is illustrated in Figure 2.4. Depending on the situation, separated-flow transition may contain some or all of the steps of natural transition.

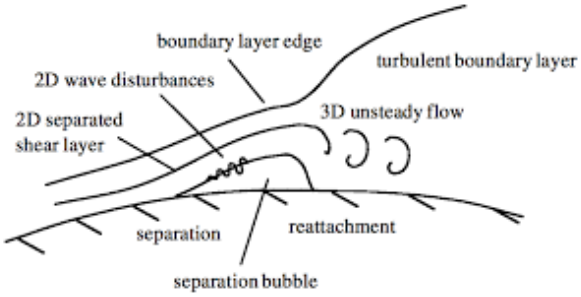

Figure 2.4. Process of separated-flow transition (Zilli et al., 2017)

2.2.1.4. Periodic-Unsteady Transition

Periodic-unsteady transition, also known as "wake-induced transition", occurs when there is an interaction of wakes within a flow, resulting in sudden transitions to turbulence. One example of this is the flow within a gas turbine, where the wakes from an upstream blade row interacts with the next stage of blades downstream (Mayle, 1991). In this research, the rotation of an arrangement of cylinders means at different points throughout the rotation, the wake of an upstream cylinder may affect a cylinder downstream.

2.2.2. Factors Affecting Transition

Many different factors can affect a flow's transition to turbulence. A few of these most applicable to the flow in question are explored below, including pressure gradient, the existence of freestream turbulence, and surface curvature.

2.2.2.1. Pressure Gradient

Depending on the freestream turbulence intensity, TI, pressure gradient can have a large impact on a flow's transition to turbulence. Generally, the lower TI is, aka the "more laminar" the freestream is, the greater the impact of pressure gradient will be. For low TI, a favorable pressure gradient in the flow can delay or prevent transition, while an adverse pressure gradient can accelerate transition (Mayle, 1991). For high TI ($TI > 1\%$), pressure gradient is of less importance and other factors dominate in significance (White, 2006).

2.2.2.2. Freestream Turbulence

Several aspects of the freestream turbulence have a significant effect on transition. Most noteworthy is the turbulence level or intensity, TI, which directly affects the rate of turbulent spot production. This in turn accelerates the process of natural transition, even to the point of causing bypass transition (Mayle, 1991).

2.2.2.3. Surface Curvature

Convex and concave surfaces can affect the transition to turbulence. At low TI, a slight delay in transition can be induced on a convex surface. Concave surfaces can either slow or speed transition depending on TI and the severity of the curvature. While finite, these effects pale in comparison to the effects of pressure gradient and freestream turbulence on transition.

3. TURBULENCE MODELING

3.1. Governing Equations of Fluid Motion

A logical starting point for modeling turbulence is the basic conservation equations of fluid motion. These three equations include the conservation of mass, conservation of momentum, and conservation of energy. The conservation of mass simply states that mass can not be created or destroyed, and can be written by

$$\frac{\partial \rho}{\partial t} + \left[\frac{\partial(\rho u)}{\partial x} + \frac{\partial(\rho v)}{\partial y} + \frac{\partial(\rho w)}{\partial z} \right] = 0 \tag{3.1}$$

for a compressible, three-dimensional flow field.

The conservation of momentum originates from Newton's second law, stating that forces on an object must balance with its mass times its acceleration. The three momentum equations (one for each dimension),

$$\frac{\partial u}{\partial t} + u\frac{\partial u}{\partial x} + v\frac{\partial u}{\partial y} + w\frac{\partial u}{\partial z} = \frac{1}{\rho}\left[-\frac{\partial p}{\partial x} + \frac{\partial \tau_{xx}}{\partial x} + \frac{\partial \tau_{yx}}{\partial y} + \frac{\partial \tau_{zx}}{\partial z} \right], \tag{3.2a}$$

$$\frac{\partial v}{\partial t} + u\frac{\partial v}{\partial x} + v\frac{\partial v}{\partial y} + w\frac{\partial v}{\partial z} = \frac{1}{\rho}\left[-\frac{\partial p}{\partial y} + \frac{\partial \tau_{xy}}{\partial x} + \frac{\partial \tau_{yy}}{\partial y} + \frac{\partial \tau_{zy}}{\partial z} \right], \tag{3.2b}$$

$$\frac{\partial w}{\partial t} + u\frac{\partial w}{\partial x} + v\frac{\partial w}{\partial y} + w\frac{\partial w}{\partial z} = \frac{1}{\rho}\left[-\frac{\partial p}{\partial z} + \frac{\partial \tau_{xz}}{\partial x} + \frac{\partial \tau_{yz}}{\partial y} + \frac{\partial \tau_{zz}}{\partial z} \right], \tag{3.2c}$$

are also known as the Navier-Stokes equations, named after their 19^{th} century derivers. For the sake of condensing these equations, the conservation of mass and momentum can be cast into a more generalized vector form by

$$\frac{D\rho}{Dt} + \rho \nabla \cdot \boldsymbol{U} = 0, \tag{3.3}$$

$$\rho \frac{D\boldsymbol{U}}{Dt} = \rho \boldsymbol{g} - \nabla p + \frac{\partial}{\partial x_j}\left[\mu \left(\frac{\partial v_i}{\partial x_j} + \frac{\partial v_j}{\partial x_i} \right) + \delta_{ij}\mu_b \nabla \cdot \boldsymbol{U} \right] \tag{3.4}$$

Finally, many flow problems use several common assumptions to reduce and simplify these equations. For a flow with constant density (incompressible) and constant viscosity, (3.3) and (3.4) can

be simplified to

$$\nabla \cdot \boldsymbol{U} = 0, \text{ and} \tag{3.5}$$

$$\rho \frac{D\boldsymbol{U}}{Dt} = \rho \boldsymbol{g} - \nabla p + \mu \nabla^2 \boldsymbol{U}. \tag{3.6}$$

It should be noted that using the above assumption of constant density and viscosity for the continuity and Navier-Stokes equations removes their effect on temperature (White, 2006). However, the conservation of energy can still be used to solve for temperature within the flow. The conservation of energy uses the First Law of Thermodynamics and balances the energy change of a system with the net flux of energy and work through the boundaries. For a compressible, 3-D flow this can be written as

$$\rho \frac{D}{Dt}\left(e + \frac{p}{\rho}\right) = \frac{Dp}{Dt} + \nabla \cdot (\kappa \nabla T) + \tau'_{ij} \frac{\partial u_i}{\partial x_j}. \tag{3.7}$$

Again, certain assumptions can greatly simplify this equation. First, substitutions can be made by replacing the internal energy with enthalpy by

$$h = e + \frac{p}{\rho}, \tag{3.8}$$

and the final term of (3.7) by the dissipative function, ϕ,

$$\phi = \tau'_{ij} \frac{\partial u_i}{\partial x_j} \tag{3.9}$$

resulting in

$$\rho \frac{Dh}{Dt} = \frac{Dp}{Dt} + \nabla \cdot (\kappa \nabla T) + \phi. \tag{3.10}$$

If the flow is assumed incompressible as above, (3.10) can be rewritten as

$$\rho c_p \frac{DT}{Dt} = \nabla \cdot (\kappa \nabla T). \tag{3.11}$$

Finally, thermal conductivity can be assumed constant if there are very small changes in temperature within the flow (White, 2006). By doing so, (3.11) becomes

$$\rho c_p \frac{DT}{Dt} = \kappa \nabla^2 T. \tag{3.12}$$

In summary, under the assumptions of constant density (incompressible), constant viscosity, and constant thermal conductivity, the governing equations of fluid motion are

$$\nabla \cdot \boldsymbol{U} = 0, \tag{3.13}$$

$$\rho \frac{D\boldsymbol{U}}{Dt} = \rho \boldsymbol{g} - \nabla p + \mu \nabla^2 \boldsymbol{U}, \text{ and} \tag{3.14}$$

$$\rho c_p \frac{DT}{Dt} = \kappa \nabla^2 T. \tag{3.15}$$

Of course, the conditions of a particular flow need to be considered to determine whether these assumptions are reasonable or if a more general form of the governing equations is necessary.

3.2. Reynolds-Averaging

Because of the random fluctuations inherent to turbulent flows, statistical methods are often used to solve the governing equations derived in the previous section. One such approach uses a technique known as Reynolds averaging in which all fluctuating flow properties are split into two components—a mean component and a fluctuating component (Hoffmann & Chiang, 2000). By this, any flow property, f, can be defined at an instant as the sum of the two components,

$$f = \bar{f} + f'. \tag{3.16}$$

This can be done for both steady and unsteady flows as shown in Figure 3.1. However, there is a slight difference in the traditional steady state Reynolds-averaged Navier-Stokes (RANS) and unsteady RANS (URANS) procedures. This difference lies within the concept of time averaging.

Time averaging is one of three averaging procedures used in RANS along with spatial averaging and ensemble averaging (Wilcox, 2006). Consider first a steady flow in which turbulence can be considered stationary—its mean not varying with time (for example the left illustration of Figure 3.1). For stationary turbulence, classical time averaging is an appropriate technique. For

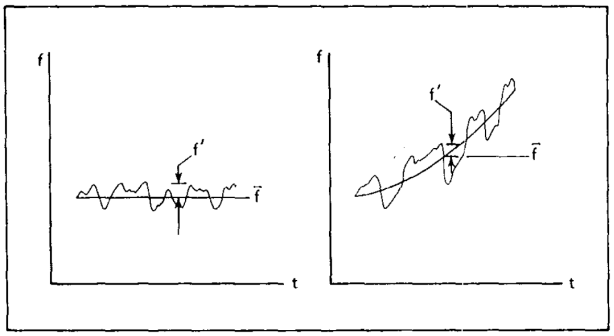

Figure 3.1. Illustration of the average and fluctuating quantities for steady (left) and unsteady (right) flows (Hoffmann & Chiang, 2000)

an instantaneous flow variable, $f(\boldsymbol{x}, t)$, its time average, $F_T(\boldsymbol{x})$ can be defined by

$$F_T(\boldsymbol{x}) = \lim_{T\to\infty} \frac{1}{T} \int_t^{t+T} f(\boldsymbol{x}, t) dt. \tag{3.17}$$

Spatial averaging is also commonly used when appropriate. If turbulence is homogeneous—its mean is uniform in all directions—the spatial average, $F_V(t)$ can be defined by integrating over the volume by

$$F_V(t) = \lim_{V\to\infty} \frac{1}{V} \int\int\int_V f(\boldsymbol{x}, t) dV. \tag{3.18}$$

Finally, ensemble averaging is commonly used for flows that decay with time, and is an average over a number of identical experiments, N, with tiny variations of initial conditions. The ensemble average, $F_E(\boldsymbol{x}, t)$ can be defined by

$$F_E(\boldsymbol{x}, t) = \lim_{N\to\infty} \frac{1}{N} \sum_{n=1}^{N} f_n(\boldsymbol{x}, t). \tag{3.19}$$

As previously mentioned, the classical approach to time averaging is only valid for steady flows with stationary turbulence. However, other approaches to the notion of time averaging for unsteady flows do exist. For example, consider a flow with a periodic nature such as the von Kármán effect behind a cylinder. Such a flow can be described with two, distinct 'timesteps', or time scales—a small time step, T_1 describing the fluctuations of the turbulence and a large time step, T_2 describing the periodicity of the vortex shedding. So long as T_2 is much larger than T_1 (by

several orders of magnitude), time averaging for such a flow can be defined by

$$F_i(\boldsymbol{x},t) = \frac{1}{T}\int_t^{t+T} f_i(\boldsymbol{x},t)dt, \text{ for } T_1 \ll T \ll T_2. \tag{3.20}$$

Again, this time averaging relies heavily on orders of magnitude in difference between T_1 and T_2, something that cannot be said for many unsteady flows. A third type of time averaging called phase averaging can be used on unsteady periodic flows such as the one described above, without the necessity that $T_2 \gg T_1$. Phase averaging is essentially an extension of ensemble averaging over each period defined by

$$< f(\boldsymbol{x},t) > \equiv \lim_{N\to\infty} \frac{1}{N}\sum_{n=1}^{N-1} f(\boldsymbol{x},t+n\tau) \tag{3.21}$$

where τ is the necessary known value of period for the flow and $f(\boldsymbol{x},t)$ is a typical Reynolds-averaged flow property with the addition of a term representing the imposed phasal unsteadiness, $\hat{f}(\boldsymbol{x},t)$, so that

$$f(\boldsymbol{x},t) = \overline{f}(\boldsymbol{x}) + \hat{f}(\boldsymbol{x},t) + f'(\boldsymbol{x},t). \tag{3.22}$$

Clearly there are several options to use RANS on unsteady flows. However, the inherent challenges from averaging unsteadiness, especially if it is non-periodic, make accurate URANS simulations difficult if not impossible for many flows (F. Menter & Egorov, 2005). This is one of the leading reasons for the recent interest in turbulence models that provide better resolution of flow structure such as LES or the scale-resolving models investigated in detail in this thesis.

3.3. Reynolds-averaged Navier-Stokes Equations

To derive the RANS equations, time averaging will be used as expressed in (3.17). However, for a proper choice of T and a flow where $T_2 \gg T_1$ the process is identical for using the time averaging described in (3.20). Consider the previously derived equations of motion for an incompressible, 3-D

flow with constant viscosity,

$$\nabla \cdot \boldsymbol{U} = 0, \tag{3.23}$$

$$\rho \frac{D\boldsymbol{U}}{Dt} = \rho \boldsymbol{g} - \nabla p + \mu \nabla^2 \boldsymbol{U}. \tag{3.24}$$

Using the viscous stress tensor,

$$\tau_{ij} = 2\mu s_{ij}, \tag{3.25}$$

where the strain-rate tensor, s_{ij} is given as

$$s_{ij} = \frac{1}{2}\left(\frac{\partial u_i}{\partial x_j} + \frac{\partial u_j}{\partial x_i}\right), \tag{3.26}$$

and expanding the divergence and gradient functions, (3.23) and (3.24) can be expressed in the form

$$\frac{\partial u_i}{\partial x_i} = 0, \tag{3.27}$$

$$\rho \frac{\partial u_i}{\partial t} + \rho u_j \frac{\partial u_i}{\partial x_j} = -\frac{\partial p}{\partial x_i} + \frac{\partial \tau_{ij}}{\partial x_j}, \tag{3.28}$$

where u_i is velocity, x_i is position, p is pressure, ρ is density, and μ is viscosity. Assuming a simple isotropic viscous fluid, $s_{ji} = s_{ij}$ and $\tau_{ji} = \tau_{ij}$. The convective term of the momentum equation can be rewritten using the conservation of mass (3.27) by

$$\begin{aligned} u_j \frac{\partial u_i}{\partial x_j} &= \frac{\partial}{\partial x_j}(u_j u_i) - u_i \frac{\partial u_j}{\partial x_j} \\ &= \frac{\partial}{\partial x_j}(u_j u_i) \end{aligned} \tag{3.29}$$

to simplify the process of time averaging. Using (3.25), (3.26), (3.28), and (3.29), the Navier-Stokes equation is found in conservation form to be

$$\rho \frac{\partial u_i}{\partial t} + \rho \frac{\partial}{\partial x_j}(u_j u_i) = -\frac{\partial p}{\partial x_i} + \frac{\partial}{\partial x_j}(2\mu s_{ji}) \tag{3.30}$$

The process of time averaging begins by replacing flow properties with their mean and fluctuating components as in (3.16). By doing so with (3.27) and (3.30) results in

$$\frac{\partial \bar{u}_i}{\partial x_i} = 0 \tag{3.31}$$

$$\rho \frac{\partial \bar{u}_i}{\partial t} + \rho \frac{\partial}{\partial x_j}\left(\overline{u_j u_i} + \overline{u'_j u'_i}\right) = -\frac{\partial \bar{p}}{\partial x_i} + \frac{\partial}{\partial x_j}(2\mu \bar{s}_{ji}). \tag{3.32}$$

Finally, (3.32) can be rewritten in its most recognizable form, often referred to as the Reynolds-averaged Navier-Stokes equation,

$$\rho \frac{\partial \bar{u}_i}{\partial x_j} = -\frac{\partial \bar{p}}{\partial x_i} + \frac{\partial}{\partial x_j}\left(2\mu \bar{s}_{ji} - \rho \overline{u'_j u'_i}\right). \tag{3.33}$$

Within (3.33) is a term containing the specific Reynolds-stress tensor,

$$\tau_{ij} = -\overline{u'_i u'_j}, \tag{3.34}$$

which as a symmetric tensor contains six unknown quantities. Prior to Reynolds-averaging, only four unknowns existed (pressure and three velocity components). However, the act of Reynolds-averaging the equations creates six additional unknowns without gaining any equations. Herein lies the turbulence closure problem—a lack of equations to solve for all unknowns. In the following chapter, several RANS turbulence models will be explored that address this issue to solve the governing equations.

3.4. Filtering and the Large Eddy Simulation Decomposition

While RANS modeling is characterized by the Reynolds time-averaging technique, Large Eddy Simulation (LES) is characterized by a filtering, or spatial-averaging technique. This filtering allows for a separation between the large scales to be resolved and the small scales to be modeled. The filtering operation for an arbitrary variable, ϕ, can be expressed in one dimension as follows,

$$\widetilde{\phi}(x,t) = \frac{1}{\Delta x}\int_{x+0.5\Delta x}^{x-0.5\Delta x} \phi(\xi,t)d\xi \tag{3.35}$$

$$\phi = \widetilde{\phi} + \phi'' \tag{3.36}$$

Because this filtering does not include any time-averaging, $\widetilde{\phi}$ is a function of both space and time (L. Davidson, 2020). Again, similar to Reynolds-averaging, filtering reduces flow quantities into two components as seen in (3.36); the LES decomposition. The first component, $\widetilde{\phi}$ represents the larger scales that will be resolved. The second component, ϕ'' represents the smaller scales that will be modeled instead of resolved. Taking the velocity vector as an example, the LES decomposition is as follows. (3.36) becomes

$$\boldsymbol{U}(\boldsymbol{x},t) = \widetilde{\boldsymbol{u}}(\boldsymbol{x},t) + \boldsymbol{u'}(\boldsymbol{x},t) \tag{3.37}$$

The spatial filter component, $\widetilde{\boldsymbol{u}}$ is essentially a low-pass filter that allows resolution of the large scales and can be expressed in the form

$$\widetilde{\boldsymbol{U}}(\boldsymbol{x},t) = \int_{\Omega_i} G(\boldsymbol{x}|\boldsymbol{\xi})\boldsymbol{U}(\boldsymbol{\xi},t)d\boldsymbol{\xi} \equiv \widetilde{\boldsymbol{u}}(\boldsymbol{x},t) \tag{3.38}$$

where G is the filter function, and Ω_i is an appropriately sized subdomain of the domain Ω (McDonough, 2007). Several filters are used in LES, including Gaussian, box, and Fourier cut-off filters. The second component, $\boldsymbol{u'}$ contains the high frequency filtered scales that should be smaller than the grid size. These will be modeled in a fashion unique to the particular LES model being used.

3.5. Large Eddy Simulation Equations

In a fashion similar to that of developing the RANS equations, the filtering process can be applied to the conservation of mass and momentum to develop the LES equations, separating what is resolved explicitly from that which must be modeled. To begin, consider again the continuity equation,

$$\nabla \cdot \boldsymbol{U} = 0. \tag{3.39}$$

Applying the filtering operation, the conservation of mass simply becomes

$$\nabla \cdot \widetilde{\boldsymbol{u}} = 0 \tag{3.40}$$

which can be implemented with little difficulty. Filtering of the momentum equation is a less trivial pursuit however, and will ultimately result in the nonlinear terms that will be modeled. Applying filtering, the momentum equation assumes the form of

$$\frac{\partial \widetilde{\boldsymbol{u}}}{\partial t} + \nabla \cdot \left(\widetilde{\boldsymbol{U}\boldsymbol{U}}\right) = -\nabla \widetilde{p} + \nu \Delta \widetilde{\boldsymbol{u}}. \tag{3.41}$$

For the nonlinear terms, the LES decomposition can be applied as follows.

$$\nabla \cdot \left(\widetilde{\boldsymbol{U}\boldsymbol{U}}\right) = \nabla \cdot \left(\widetilde{(\widetilde{\boldsymbol{u}} + \boldsymbol{u'})(\widetilde{\boldsymbol{u}} + \boldsymbol{u'})}\right) \tag{3.42}$$

The terms can be then written in matrix form,

$$\widetilde{(\widetilde{\boldsymbol{u}} + \boldsymbol{u'})(\widetilde{\boldsymbol{u}} + \boldsymbol{u'})} = \begin{bmatrix} \widetilde{(\widetilde{u} + u')(\widetilde{u} + u')} & \widetilde{(\widetilde{u} + u')(\widetilde{v} + v')} & \widetilde{(\widetilde{u} + u')(\widetilde{w} + w')} \\ \widetilde{(\widetilde{u} + u')(\widetilde{v} + v')} & \widetilde{(\widetilde{v} + v')(\widetilde{v} + v')} & \widetilde{(\widetilde{v} + v')(\widetilde{w} + w')} \\ \widetilde{(\widetilde{u} + u')(\widetilde{w} + w')} & \widetilde{(\widetilde{v} + v')(\widetilde{w} + w')} & \widetilde{(\widetilde{w} + w')(\widetilde{w} + w')} \end{bmatrix}. \tag{3.43}$$

For purpose of demonstration, consider the following expansion of one of the matrix terms,

$$\widetilde{(\widetilde{u} + u')(\widetilde{v} + v')} = \widetilde{\widetilde{u}\widetilde{v}} + \widetilde{\widetilde{u}v'} + \widetilde{u'\widetilde{v}} + \widetilde{u'v'}. \tag{3.44}$$

This can be further generalized to apply to the rest of the terms,

$$\widetilde{(\widetilde{u_i} + u_i')(\widetilde{u_j} + u_j')} = \widetilde{\widetilde{u_i}\widetilde{u_j}} + \widetilde{\widetilde{u_i}u_j'} + \widetilde{u_i'\widetilde{u_j}} + \widetilde{u_i'u_j'}. \tag{3.45}$$

Within (3.45) exists three unique forms of terms—the first term, the middle pair of terms, and the final term. The first term, $\widetilde{\widetilde{u_i}\widetilde{u_j}}$, is a portion of the Leonard stress. This is the only term that can be computed without the necessity of modeling as we have equations for $\widetilde{u_i}$ and $\widetilde{u_j}$. The next two terms, $\widetilde{\widetilde{u_i}u_j'} + \widetilde{u_i'\widetilde{u_j}}$, are known as the cross stress. Because these contain small scales, they require the use of modeling. Finally, the last term, $\widetilde{u_i'u_j'}$, is called the Reynolds stress due to its similar form to its Reynolds-Averaging counterpart. Aside from their common name and appearance, it is important to consider that the "Reynolds Stresses" of RANS and LES are fundamentally different due to the nature of the Reynolds-Averaging and filtering processes.

In summary, the Leonard, cross, and Reynolds stress terms are given below respectively,

$$L_{ij} = \widetilde{\widetilde{u_i}\widetilde{u_j}} - \widetilde{u_i}\widetilde{u_j}, \tag{3.46}$$

$$C_{ij} = \widetilde{\widetilde{u_i}u'_j} + \widetilde{u'_i\widetilde{u_j}}, \tag{3.47}$$

$$R_{ij} = \widetilde{u'_iu'_j}. \tag{3.48}$$

Finally, the momentum equation can be rewritten. It is desired that the term $\nabla \cdot (\widetilde{\boldsymbol{u}}\widetilde{\boldsymbol{u}})$ is within the equation, so the nonlinear terms become

$$\widetilde{\boldsymbol{u}}\widetilde{\boldsymbol{u}} + \left[\widetilde{(\widetilde{\boldsymbol{u}} + u')(\widetilde{\boldsymbol{u}} + u')} - \widetilde{\boldsymbol{u}}\widetilde{\boldsymbol{u}}\right] \equiv \widetilde{\boldsymbol{u}}\widetilde{\boldsymbol{u}} + \boldsymbol{\tau}_{SGS} \tag{3.49}$$

Substituting back into the momentum equation, we have

$$\widetilde{\boldsymbol{u}}_t + \nabla \cdot (\widetilde{\boldsymbol{u}}\widetilde{\boldsymbol{u}}) = -\nabla\widetilde{p} + \nu\Delta\widetilde{\boldsymbol{u}} - \nabla \cdot \boldsymbol{\tau}_{SGS} \tag{3.50}$$

where $\boldsymbol{\tau}_{SGS}$ is the LES subgrid-scale stress,

$$\boldsymbol{\tau}_{SGS} \equiv L_{ij} + C_{ij} + R_{ij}. \tag{3.51}$$

Now the only terms needing to be modeled (containing the smallest scales) are contained within $\boldsymbol{\tau}_{SGS}$. The way this is done will depend on the specific LES model chosen. In the following section, different turbulence modeling techniques will be presented, including several RANS models relevant to this research, the LES model most commonly used in hybrid approaches, as well as the hybrid models themselves.

4. TURBULENCE MODELS

As discussed in the previous section, Reynolds-averaging the Navier-Stokes equations is one approach to turbulence modeling, as well as the filtering process of Large Eddy Simulation (LES). Another method of solving the Navier-Stokes equations is Direct Numerical Simulation (DNS), which fully resolves all scales down to the Kolmogorov scale. Finally, the focus of this thesis lies within the recent development of hybrid turbulence models which typically combine RANS and LES models in an effort to reap the benefits of each while minimizing their drawbacks. In this chapter, an overview of several RANS and LES models, DNS, and several hybrid models will be given. An illustration of the hierarchy of these model approaches with respect to their computational cost and scale resolution is shown in Figure 4.1.

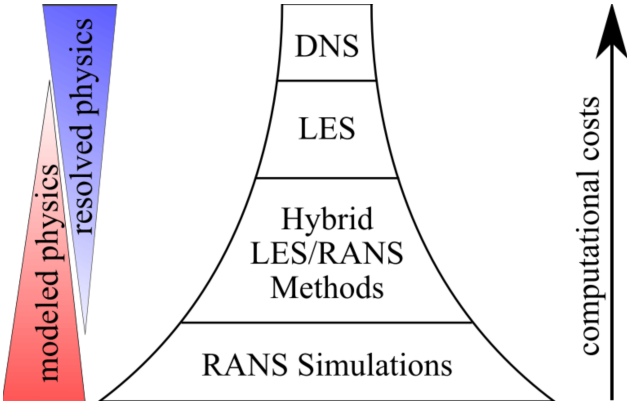

Figure 4.1. Hierarchy of CFD turbulence models considering resolved vs. modeled structure and computational cost (Xiao & Cinnella, 2019)

4.1. Direct Numerical Simulation

While not used in this research, a brief review of Direct Numerical Simulation (DNS) provides proper context for the necessity of the RANS, LES and hybrid modeling techniques utilized. As mentioned above, DNS uses numerical methods to resolve all scales of motion within a flow, from the largest to the smallest at the Kolmogorov length scale (2.1a). Because of this, a grid fine enough to properly carry out DNS needs to be of the same order of magnitude at any point as the scales that exist there. In addition, the time step used must be of the same order of magnitude

of the Kolmogorov time scale, (2.1b). As all space and time scales are resolved and none are left to be modeled, DNS is in a sense the inherent lack of turbulence modeling. The requirements to accommodate the minuscule grid size and time step necessary however quickly result in an extremely high computational cost that increases rapidly with the Reynolds number. In fact, estimates have put the computational cost of DNS solutions proportional to Re^3 as opposed to Re^2 for LES solutions and Re for RANS solutions (McDonough, 2007). To illustrate this point, rough estimations show that to perform DNS for an external flow over an airfoil at $Re = 1,000,000$ would require approximately 4 trillion mesh points and 600 TB of RAM, while the same problem could be done using LES with 52 million mesh points and 8 GB of RAM (Choi & Moin, 1995; DeLeon, 2016). In the future, it is possible that quantum computing and algorithms will make the use of DNS more common, but for the time being it remains a seldom-used technique for low-Reynolds number academic cases (Rodriguez, 2019).

4.2. Reynolds-averaged Navier-Stokes Models

Models that utilize the RANS equations can largely be categorized into one of three groups—zero-equation models, one-equation models, and two-equation models. Zero-equation models (aka algebraic models) use the concepts of the Boussinesq eddy-viscosity approximation and Prandtl's mixing-length hypothesis to compute the Reynolds stress tensor (Wilcox, 2006). The essence of the Boussinesq approximation is in the comparison of the shear stress in a turbulent flow (subscript t) to the relationship found in laminar flow (subscript l),

$$\tau_l = \mu \frac{\partial \bar{u}_i}{\partial x_j} = \rho \nu \frac{\partial \bar{u}_i}{\partial x_j} \tag{4.1}$$

$$\tau_t = \mu_t \frac{\partial \bar{u}_i}{\partial x_j} = \rho \nu_t \frac{\partial \bar{u}_i}{\partial x_j}. \tag{4.2}$$

This introduces the concept of an eddy viscosity, denoted μ_t or ν_t (Hoffmann & Chiang, 2000). The Prandtl hypothesis also likens a property of laminar flow to turbulence, considering that 'lumps' of fluid in a turbulent flow travel a finite distance before they collide and lose their identity, similarly to the concept of molecules in a laminar flow traveling a mean-free path distance before colliding (Hoffmann & Chiang, 2000). In relation to the Reynolds stress tensor, this is expressed

by

$$\begin{aligned}\tau_t &= -\rho\overline{u_i' u_j'} \\ &= \rho l_m^2 \left(\frac{\partial \bar{u}_i}{\partial x_j}\right)^2 \end{aligned} \tag{4.3}$$

where l_m is the Prandtl mixing length. Zero-equation models are simple, but incomplete in the sense that they require known values of the eddy viscosity and mixing length prior to simulation (Wilcox, 2006).

One-equation models also use the Boussinesq approximation along with either the turbulence kinetic equation or an eddy viscosity equation. Those using an eddy viscosity equation are complete due to automatically providing the turbulence length and are therefore more commonly used (Wilcox, 2006). One of the most popular eddy viscosity based one-equation models is the Spalart-Allmaras model. Although two-equation models have gained increasing popularity since their creation, one-equation models such as Spalart-Allmaras retain their place in CFD usage for certain flows, and have even been implemented with scale-resolving models such as Menter's Scale-Adaptive Simulation (F. Menter, Kuntz, & Bender, 2003).

Finally, two-equation models provide equations for the computation of the turbulence kinetic energy, k, as well as for a necessary length scale such as the turbulence length scale (Wilcox, 2006). Therefore, they are complete and require no prior knowledge of the flow field for computation. Several two-equation models are briefly discussed below.

4.2.1. k-ϵ Model

There are many variations of $k-\epsilon$ models available today, characterized as such by consisting of a PDE for both the turbulent kinetic energy, k, and dissipation, ϵ (hence, a two-equation model). The specific model presented here, developed by Tennekes and Lumley, uses dimensional analysis to link eddy viscosity to k and ϵ by

$$\nu_t = C_\nu \frac{k^2}{\epsilon}, \tag{4.4}$$

where C_ν is a constant. The equations for k and ϵ can be given as

$$\frac{\partial k}{\partial t} + \frac{\partial}{\partial x_j}(\bar{u}_j k) = \frac{\partial}{\partial x_j}\left[\left(\nu + \frac{\nu_t}{\sigma_k}\right)\frac{\partial k}{\partial x_j}\right] + P_k - \rho\epsilon \tag{4.5}$$

$$\frac{\partial \epsilon}{\partial t} + \frac{\partial}{\partial x_j}(\bar{u}_j \epsilon) = \frac{\partial}{\partial x_j}\left[\left(\nu + \frac{\nu_t}{\sigma_\epsilon}\right)\frac{\partial \epsilon}{\partial x_j}\right] + \frac{\epsilon}{k}\left(C_{\epsilon 1} P_k - C_{\epsilon 2}\epsilon\right) \tag{4.6}$$

where the turbulence production due to viscosity, P_k, is modeled for incompressible flows by

$$P_k = \nu_t \left(\frac{\partial \bar{u}_i}{\partial x_j} + \frac{\partial \bar{u}_j}{\partial x_i}\right)\frac{\partial \bar{u}_i}{\partial x_j} \tag{4.7}$$

The closure coefficients are given to be

$$C_\nu = 0.09, \quad C_{\epsilon 1} = 1.44, \quad C_{\epsilon 2} = 1.92, \quad \sigma_k = 1.0, \quad \sigma_\epsilon = 1.3 \tag{4.8}$$

for the standard model used in ANSYS CFX (ANSYS, 2017; McDonough, 2007).

4.2.2. k-ω Model

Similarly to the $k-\epsilon$ model, there are several variations of $k-\omega$ models available, all characterized by equations solving for the specific dissipation rate, ω. Here the Wilcox model, also used in ANSYS CFX is presented. $k-\omega$ models first assume that eddy viscosity is related to k and ω by

$$\nu_t = \frac{k}{\omega}. \tag{4.9}$$

The equations for k and ω are given as

$$\frac{\partial k}{\partial t} + \frac{\partial}{\partial x_j}(\bar{u}_j k) = \frac{\partial}{\partial x_j}\left[\left(\nu + \frac{\nu_t}{\sigma_k}\right)\frac{\partial k}{\partial x_j}\right] + P_k - \beta^* k\omega \tag{4.10}$$

$$\frac{\partial \epsilon}{\partial t} + \frac{\partial}{\partial x_j}(\bar{u}_j \epsilon) = \frac{\partial}{\partial x_j}\left[\left(\nu + \frac{\nu_t}{\sigma_\epsilon}\right)\frac{\partial \epsilon}{\partial x_j}\right] + \alpha\frac{P_k}{\nu_t} - \beta\omega^2 \tag{4.11}$$

where the production term is calculated as for the $k-\epsilon$ model using (4.7). The closure constants are given by

$$\beta^* = 0.09, \quad \alpha = 5/9, \quad \beta = 0.075, \quad \sigma_k = 2, \quad \sigma_\omega = 2 \tag{4.12}$$

for the Wilcox model (ANSYS, 2017; Wilcox, 2006).

4.2.3. Shear Stress Transport Model

Menter's $k-\omega$ SST Model was created in an effort to combine the best qualities of both the $k-\epsilon$ and $k-\omega$ models (F. R. Menter, 1994). It utilizes a blending function to use the $k-\omega$ model nearest to walls and the $k-\epsilon$ model farther away. In addition, a shear stress limiter is included in regions of adverse pressure gradients (L. Davidson, 2020).

To combine the $k-\omega$ and $k-\epsilon$ models, the $k-\epsilon$ model is first transformed into the form of a $k-\omega$ model by use of $\omega = \epsilon/(\beta^* k)$, where $\beta^* = c_\mu$ (L. Davidson, 2020). The transport equations for turbulent kinetic energy, k, and specific dissipation rate, ω, are given below in (4.13) and (4.14).

$$\frac{\partial k}{\partial t} + \frac{\partial}{\partial x_j}(\bar{v}_j k) = \frac{\partial}{\partial x_j}\left[\left(\nu + \frac{\nu_t}{\sigma_k}\right)\frac{\partial k}{\partial x_j}\right] + P^k - \beta^* k\omega \tag{4.13}$$

$$\frac{\partial \omega}{\partial t} + \frac{\partial}{\partial x_j}(\bar{v}_j \omega) = \frac{\partial}{\partial x_j}\left[\left(\nu + \frac{\nu_t}{\sigma_\omega}\right)\frac{\partial \omega}{\partial x_j}\right] + \alpha\frac{P^k}{\nu_t} - \beta\omega^2 + 2(1-F_1)\sigma_{\omega 2}\frac{1}{\omega}\frac{\partial k}{\partial x_i}\frac{\partial \omega}{\partial x_i} \tag{4.14}$$

The key difference in the $k-\epsilon$ and $k-\omega$ models is the inclusion of the final term in (4.14). The degree of this term's influence is controlled using the blending function F_1 given in (4.15), where d is the distance to the nearest wall node. A value of $F_1 = 0$ reverts to the $k-\epsilon$ formulation (far from walls), and a value of $F_1 = 1$ reverts to the $k-\omega$ formulation (near walls).

$$F_1 = \tanh\left(\xi^4\right), \quad \xi = \min\left[\max\left\{\frac{\sqrt{k}}{\beta^*\omega d}, \frac{500\nu}{d^2\omega}\right\}, \frac{4\sigma_{\omega_{k-\epsilon}} k}{CD_\omega d^2}\right],$$
$$CD_\omega = \max\left\{2\sigma_{\omega_{k-\epsilon}}\frac{1}{\omega}\frac{\partial k}{\partial x_i}\frac{\partial \omega}{\partial x_i}, 10^{-10}\right\} \tag{4.15}$$

Constants in the transport equations (α, β, σ_k, and σ_ω) are blended linearly between their $k-\epsilon$ and $k-\omega$ values according to F_1,

$$x = F_1 x_{k-\omega} + (1 - F_1) x_{k-\epsilon} \tag{4.16}$$

for an arbitrary constant x.

Similarly, a second blending function, F_2, is used in computation of the eddy viscosity, ν_t, as seen in (4.17). The inclusion of the max function in the denominator is the previously mentioned shear stress limiter, which reverts to the $k - \omega$ formulation for eddy viscosity if the production is too large (when $\bar{s}$ is large) (L. Davidson, 2020).

$$\nu_t = \frac{a_1 k}{\max(a_1 \omega, |\bar{s}| F_2)}, \quad F_2 = \tanh(\eta^2), \quad \eta = \max\left\{ \frac{2\sqrt{k}}{\beta^* \omega d}, \frac{500\nu}{d^2 \omega} \right\} \tag{4.17}$$

The constants for the SST model used in this study are given below (ANSYS, 2017; L. Davidson, 2020):

$$\begin{gathered} \beta^* = 0.09, \quad a_1 = 0.31 \\ \alpha_{k-\omega} = 5/9, \quad \beta_{k-\omega} = 3/40, \quad \sigma_{k,k-\omega} = 0.85, \quad \sigma_{\omega,k-\omega} = 0.5 \\ \alpha_{k-\epsilon} = 0.44, \quad \beta_{k-\epsilon} = 0.0828, \quad \sigma_{k,k-\epsilon} = 1, \quad \sigma_{\omega,k-\epsilon} = 0.856 \end{gathered} \tag{4.18}$$

While the SST model is a considerable improvement over a single $k - \epsilon$ or $k - \omega$ model for many flows, as a URANS model it still struggles to display the correct spectrum of turbulence scales, particularly the large scales (F. Menter & Egorov, 2005).

4.3. Large Eddy Simulation Models

Large Eddy Simulation (LES) is another approach to turbulence modeling that resolves all but the smallest turbulence scales, only modeling those smaller than the size of the computational cell itself. Ideally, this results in about 80% of the energy contained by the turbulence scales being resolved, and about 20% being modeled. Because of this, much unsteadiness remains within the flow and simulations with extremely high accuracy and detail are possible. However, this is only possible with extremely fine meshing, particularly near wall boundaries where the smallest scales exist, and therefore LES comes at a high computational cost. As with RANS, there are a number

of LES models that have been developed over the years, ranging in complexity and in modeling techniques. The Wall-Adapted Local Eddy Viscosity model (WALE) is commonly used with hybrid models such as Stress-Blended Eddy Simulation, and is therefore described below.

4.3.1. Wall-Adapted Local Eddy Viscosity Model

The Wall-Adapted Local Eddy Viscosity (WALE) model is a LES model commonly used by itself as well as with RANS models in hybrid approaches. It is similar to the classic zero-equation Smagorinsky model, but offers improvements in several areas (ANSYS, 2017; Nicoud & Ducros, 1999). The eddy-viscosity is calculated as follows,

$$\nu_{SGS} = (C_w \Delta)^2 \frac{\left(S_{ij}^d S_{ij}^d\right)^{3/2}}{\left(\overline{S}_{ij}\overline{S}_{ij}\right)^{5/2} + \left(S_{ij}^d S_{ij}^d\right)^{5/4}}. \tag{4.19}$$

S_{ij}^d is the traceless symmetric part of the velocity gradient tensor squared, given by

$$S_{ij}^d = \frac{1}{2}\left(\bar{g}_{ij}^2 + \bar{g}_{ji}^2\right) - \frac{1}{3}\delta_{ij}\bar{g}_{kk}^2, \tag{4.20}$$

where

$$\bar{g}_{ij}^2 = \bar{g}_{ik}\bar{g}_{kj}, \quad \bar{g}_{ij} = \frac{\partial \bar{u}_i}{\partial x_j}, \tag{4.21}$$

and δ_{ij} is the Kronecker delta. Using these relations, and $\overline{\Omega}$ as the anti-symmetric part of $\bar{g}$,

$$\overline{\Omega}_{ij} = \frac{1}{2}\left(\frac{\partial \overline{U}_i}{\partial x_j} - \frac{\partial \overline{U}_j}{\partial x_i}\right), \tag{4.22}$$

(4.20) can be rewritten as follows:

$$S_{ij}^d = \overline{S}_{ik}\overline{S}_{kj} + \overline{\Omega}_{ik}\overline{\Omega}_{kj} - \frac{1}{3}\delta_{ij}\left(\overline{S}_{mn}\overline{S}_{mn} - \overline{\Omega}_{mn}\overline{\Omega}_{mn}\right). \tag{4.23}$$

Note that in the ANSYS CFX implementation of the WALE model, the constant C_w is set to $C_w = 0.5$.

As mentioned above, the WALE model offers several advantages over the traditional Smagorinsky model. One such advantage is its ability to accurately model the laminar to turbulent transition

of wall-bounded flows due to the design of its invariant, $S_{ij}^d S_{ij}^d$ (Nicoud & Ducros, 1999). It also does not include secondary filtering as models such as the Dynamic Smagorinsky-Lilly model do.

4.4. Hybrid Models

Over the past ~25 years, new turbulence modeling techniques have been developed that aim to combine RANS and LES models in a strategic fashion. The general goal of these models is to implement RANS at and near wall boundaries (especially within the boundary layer) while using LES (or similar scale-resolving techniques) away from wall boundaries. By doing so, the extreme computational costs associated with using LES to resolve near-wall turbulence scales are avoided while the benefits of resolving the larger scales away from the walls are kept.

4.4.1. Scale-Adaptive Simulation

Scale-Adaptive Simulation (SAS) is characterized by the introduction of the von Kármán length scale, L_{vK}, shown in (4.24) (F. Menter & Egorov, 2005). This scale contains the second velocity gradient and is therefore suitable for detecting unsteadiness within a flow (L. Davidson, 2020).

$$L_{vK} = \kappa \left| \frac{U'}{U''} \right|, \quad U' = \sqrt{2 S_{ij} S_{ij}}, \quad U'' = \sqrt{\frac{\partial^2 U_i}{\partial x_k^2} \frac{\partial^2 U_i}{\partial x_j^2}} \tag{4.24}$$

The "Scale-Adaptive" nature of this method comes from the ratio of turbulence length scale, $L_t = k^{1/2}/(\omega c_\mu^{1/4})$, to von Kármán length scale, L_{vK}, which is key to the transition from SST to SAS "modes". To implement SAS with SST, the source term P_{SAS} shown below is added into (4.14).

$$P_{SAS} = F_{SAS} \max(T_1 - T_2, 0), \quad T_1 = \widetilde{\zeta}_2 \kappa S^2 \frac{L_t}{L_{vK}}, \quad T_2 = \frac{2k}{\sigma_\phi} \max\left(\frac{1}{\omega^2} \frac{\partial \omega}{\partial x_j} \frac{\partial \omega}{\partial x_j}, \frac{1}{k^2} \frac{\partial k}{\partial x_j} \frac{\partial k}{\partial x_j} \right) \tag{4.25}$$

The essence of SAS is captured in T_1, while T_2 exists to ensure that in steady flow, SST mode will be used. The addition of this source term (which will always be >= 0 due to the max function) will increase ω, decreasing the eddy viscosity ν_t. This allows unsteadiness in the flow to remain without being over-dissipated, one of the reasons this is preferable for unsteady flows.

It should be noted that while this model introduces an increased degree of scale-resolving capability to URANS models such as SST, it is still essentially a URANS model with an additional

production term. The next several models presented fit the classical definition of a hybrid model—blending RANS and LES models together in some fashion.

4.4.2. Detached Eddy Simulation

Detached Eddy Simulation (DES) was the first attempt at a hybrid model that blends a RANS model close to wall boundaries into a LES model farther from wall boundaries. Several versions of this model exist, including those implementing the Spalart-Allmaras one-equation RANS model as well as Menter's SST RANS model. Here the formulation of Strelets using the SST model is presented (Strelets, 2001).

The essence of of DES is a grid-dependent switch between RANS and LES modes based on the local turbulent length scale represented by

$$\begin{aligned} C_{DES}\Delta_{\max} > L_t \rightarrow RANS \\ C_{DES}\Delta_{\max} \leq L_t \rightarrow LES \end{aligned} \tag{4.26}$$

where $\Delta_{\max}$ is the maximum edge length of each cell and C_{DES} is typically chosen as $C_{DES} = 0.61$. Intuitively, this means that when the grid size is sufficiently small (to a degree modifiable by the constant C_{DES}) in comparison to the local turbulent length scale, the LES formulation will be used to resolve turbulence. Otherwise, the RANS formulation will be used to model the turbulence (F. Menter, 2015). The turbulent length scale, L_t, for a $k-\omega$ model such as the SST model is defined as

$$L_t = \frac{k^{3/2}}{\epsilon} = \frac{\sqrt{k}}{\beta^*\omega}. \tag{4.27}$$

To implement this into the SST model, take the k equation previously described for the $k-\omega$ model,

$$\frac{\partial k}{\partial t} + \frac{\partial}{\partial x_j}(\bar{u}_j k) = \frac{\partial}{\partial x_j}\left[\left(\nu + \frac{\nu_t}{\sigma_k}\right)\frac{\partial k}{\partial x_j}\right] + P_k - \beta^* k\omega, \tag{4.28}$$

and substitute the relevant relationship for the turbulent length scale, implementing the DES limiter in (4.26), resulting in

$$\frac{\partial k}{\partial t} + \frac{\partial}{\partial x_j}(\bar{u}_j k) = \frac{\partial}{\partial x_j}\left[\left(\nu + \frac{\nu_t}{\sigma_k}\right)\frac{\partial k}{\partial x_j}\right] + P_k - \frac{k^{3/2}}{\min(L_t, C_{DES}\Delta_{\max})}. \tag{4.29}$$

Ideally, DES uses the RANS model within the boundary layer and attached flow regions. Because of the grid-dependent switch described above however, this can easily go awry without proper care of grid size and selection of C_{DES}. For example, grid refinement within the boundary layer can cause a premature transition to the LES formulation, in turn reducing eddy viscosity and causing separation arbitrarily. This is commonly known as Grid-Induced Separation, and is the primary downfall of the traditional DES model (F. Menter, 2015). The following section describes two approaches to dealing with this issue.

4.4.3. Delayed and Shielded Detached Eddy Simulation

Delayed Detached Eddy Simulation (DDES) addresses the issue of Grid-Induced Separation in DES by 'protecting' the boundary layer from the DES limiter. Similar to DES, DDES has been applied to both the Spalart-Allmaras and SST models; once again the SST formulation is presented here (F. Menter, 2015; F. Menter, Kuntz, & Langtry, 2003).

Considering the dissipation term of the k equation modified by the DES limiter, the DDES version is derived as follows

$$E_{DES} = \frac{k^{3/2}}{\min(L_t, C_{DES}\Delta)} \tag{4.30}$$

$$= \frac{k^{3/2}}{L_t \min(1, C_{DES}\Delta/L_t)} \tag{4.31}$$

$$= \frac{k^{3/2}}{L_t} \max\left(1, \frac{L_t}{C_{DES}\Delta}\right) \tag{4.32}$$

$$E_{DDES} = \frac{k^{3/2}}{L_t} \max\left(1, \frac{L_t}{C_{DES}\Delta}(1 - F_{DDES})\right), \tag{4.33}$$

where F_{DDES} is a function that attempts to shield the boundary layer while still allowing turbulence to be resolved after separation. Despite its improvements upon DES, Grid-Induced Separation is still possible when using DDES.

Shielded Detached Eddy Simulation (SDES) is yet another approach to shielding the boundary layer, implementing a new shielding function and grid scale. Implementing into the k equation, the dissipation term becomes

$$E_{SDES} = \frac{k^{3/2}}{L_t}\left[\max\left(1, \frac{L_t}{C_{SDES}\Delta_{SDES}}(1 - F_{SDES})\right) - 1\right], \tag{4.34}$$

(F. Menter, 2015). Because the new shielding function F_{SBES} provides stronger shielding, the grid scale, Δ is reduced as follows.

$$\Delta_{SDES} = \max\left(\sqrt[3]{Vol}, 0.2\Delta_{\max}\right) \tag{4.35}$$

4.4.4. Stress-Blended Eddy Simulation

Stress-Blended Eddy Simulation (SBES) is a further improvement upon the SDES model. It utilizes the same proprietary blending function ($F_{SBES} = F_{SDES}$) but includes an explicit model switch. Using the shielding function, the stresses can be linearly blended accordingly, by

$$\tau_{ij}^{SBES} = F_{SBES}\tau_{ij}^{RANS} + (1 - F_{SBES})\,\tau_{ij}^{LES} \tag{4.36}$$

where τ_{ij}^{RANS} and τ_{ij}^{LES} are the RANS and LES modeled portions of the stress tensor, respectively (F. Menter, 2016). If both the RANS and LES models are eddy-viscosity based models, such as the SST RANS model and WALE LES model, this further simplifies to a blending of the eddy viscosities,

$$\nu_t^{SBES} = F_{SBES}\nu_t^{RANS} + (1 - F_{SBES})\,\nu_t^{LES} \tag{4.37}$$

SBES features many improvements over other scale-resolving hybrid models, including an explicit switch between desired RANS and LES models, asymptotic shielding of the boundary layer, and a rapid transition between RANS and LES models.

5. FLOW EXPERIMENTS

In this research, computations were done in conjunction with wind tunnel experiments done by Ullah, Fabijanic and Estevadeordal at North Dakota State University (Thomas et al., 2021; Ullah et al., 2020; Ullah, 2020). These experiments shared a similar purpose to the computations in researching the nature of the flow around the cylinders. In addition they provide verification to the accuracy of the CFD results. The nature of these experiments, including the wind tunnel, PIV setup, and other equipment are presented in this section.

5.1. Wind Tunnel Characteristics

A FloTek 1440 subsonic, open return wind tunnel was used for all experimentation. The wind tunnel features a 12" by 12" square test section with transparent side panels to allow PIV measurements and visual inspection. At the test section, the wind tunnel is able to deliver a freestream velocity of $U_\infty = 36$ m/s. The wind tunnel is shown in Figure 5.1.

Figure 5.1. FloTek 1440 wind tunnel

5.2. Three-Cylinder Experiments

At the core of these experiments is the setup of three cylinders spaced equilaterally and rotating about a common axis. The diameter of each cylinder is 3.1 mm, and the spacing between each cylinders' surfaces is 5.3 mm. Nondimensionalizing by the cylinder diameter results in a spacing ratio of $S = 1.70$. Rotation is counterclockwise from the point of view of the PIV results. The cylinder geometry and setup within the wind tunnel is shown in Figure 5.2 with each cylinder labeled as it is referred to in this study.

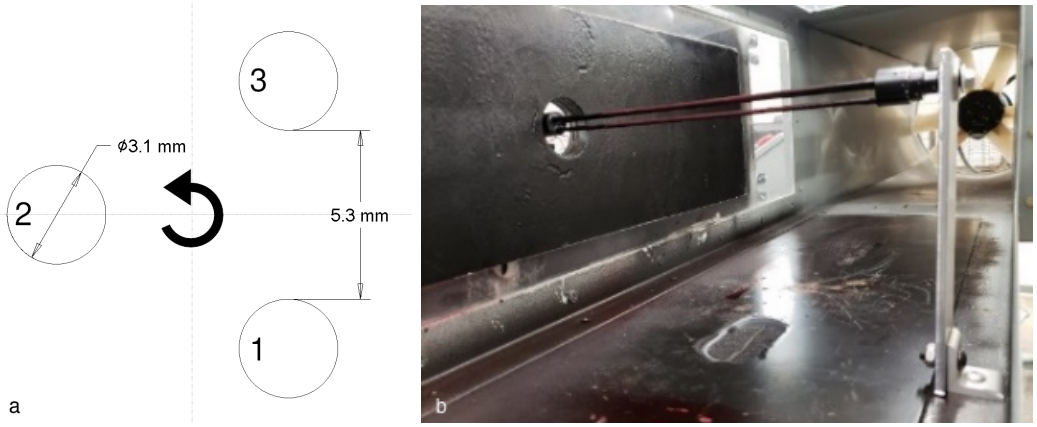

Figure 5.2. Three-cylinder setup (a) geometry and (b) wind tunnel setup (Ullah et al., 2020)

Three measurement techniques were used in these experiments—hotwire anemometry, 2D PIV, and 3D tomography. Velocity measurements were taken from three distinct locations using a hotwire. Two locations were chosen immediately behind the rotating cylinders—one centered vertically and the second near the top of the setup. The third location was centered vertically but much further downstream. The locations of these points relative to the common axis of rotation are shown in Figure 5.3. Nondimensionalizing once again by a single cylinder diameter, these locations are given in Table 5.1. The time series velocity data collected via hotwire was used to create

Table 5.1. Hotwire measurement point locations

Point	x	y
A	2.39	0
B	2.39	2.21
C	33.03	0

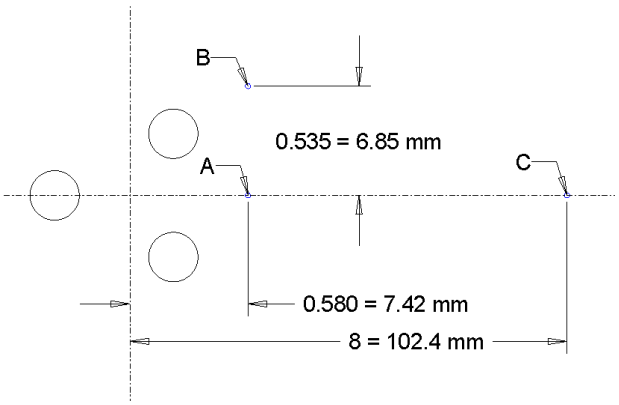

Figure 5.3. Hotwire measurement locations

frequency spectra using Fast Fourier Transformations (FFTs). From this, the Strouhal number for each experiment was calculated using the dominant frequencies and single cylinder diameter as characteristic length. A series of these experiments were performed with no rotation of the cylinders. The Reynolds number ranged from 57 to 7470, and three different cylinder orientations were used.

2D PIV was used to obtain instantaneous velocity fields for rotating and static cases. Imaging was done at two separate field-of-views (FOVs), in both cases with two separate cameras combining for the entire domain. In the first, "far" view, each camera produced a 80 mm FOV for a combined FOV of 160 mm. In the second, "close" view, each camera produced a 40 mm FOV for a combined FOV of 80 mm, showing greater detail in the flow near the cylinders. These experiments ranged in Reynolds number from 57 to 7150, and in rotation speed from 120 RPM to 3000 RPM (2 Hz to 50 Hz), as well as static cases. From the velocity fields, instantaneous contours of Z vorticity were produced as well as time-averaged velocity, vorticity, and standard deviation contours.

3D tomography was performed over a calibrated volume approximately 6 mm in depth using four cameras. As with the 2D PIV results, several filters were passed over the raw data to make remove unphysical characteristics. From these results, iso-surfaces of Z vorticity were produced as well as contour slices of Z vorticity at three locations spanning the depth ($Z = 2.5$ mm, $Z = 0$ mm, and $Z = -2.5$ mm).

Full details of these experiments and the results found are available in Al Habib Ullah's thesis (Ullah, 2020).

6. CFD COMPUTATION METHODS

6.1. Software

All computations in this research were run with the commercial CFD software ANSYS CFX 18.2. CFX is a Navier-Stokes solver using Finite Volume Method based on Elements (EbFVM) with a Cell Vertex Formulation with a wide availability of turbulence models ranging from algebraic models to hybrid and LES models (ANSYS, 2017). In addition it offers a large amount of control to the user in tuning model constants and implementing model extensions where desired. It scales extremely well in parallel, bringing computational times down significantly. It also interfaces well with ANSYS ICEM, a robust and powerful meshing software used for all mesh generation in the research. Geometry was created using Creo Parametric 4.0 and further modified within ANSYS ICEM. Tecplot 360 EX 2018 R2 was used for most of the post-processing, including all contours, iso-surfaces, and many of the plots generated. In addition, Tecplot's Python API (PyTecplot) was used to automate much of this post-processing of transient .trn and .cgns files. Other plots and results processing was done with Python using packages such as Numpy, Matplotlib, and Pandas for array operations, plotting, and file processing.

6.2. Hardware

This work made use of computing resources at the Center for Computationally Assisted Science and Technology (CCAST) at North Dakota State University. CCAST's Thunder Cluster contains several condos of computing nodes for running the CFX jobs. For the cases run, 7–10 20–core nodes were used in parallel, each with 42 GB of available RAM and 2x Intel Ivy Bridge E5–2670 v2 10C 2.5GHz processors (for Computationally Assisted Science & Technology, 2017). Computational cost for each run ranged in the order of 2×10^4 to 2×10^5 CPU hours, largely dependent on variables such as Reynolds number and setup rotational velocity, model selection, and number of nodes requested.

6.3. Fluid Domain Geometry

Several iterations of the fluid domain were created before settling upon the final version. All geometries created consisted of a rectangular, stationary domain and a cylindrical, rotating domain containing the setup of cylinders to allow rotation in the simulations. Geometry modifications were

done primarily to reduce the size of the domain in preservation of computational cost without sacrificing accuracy. The original domain is shown in Figure 6.1.

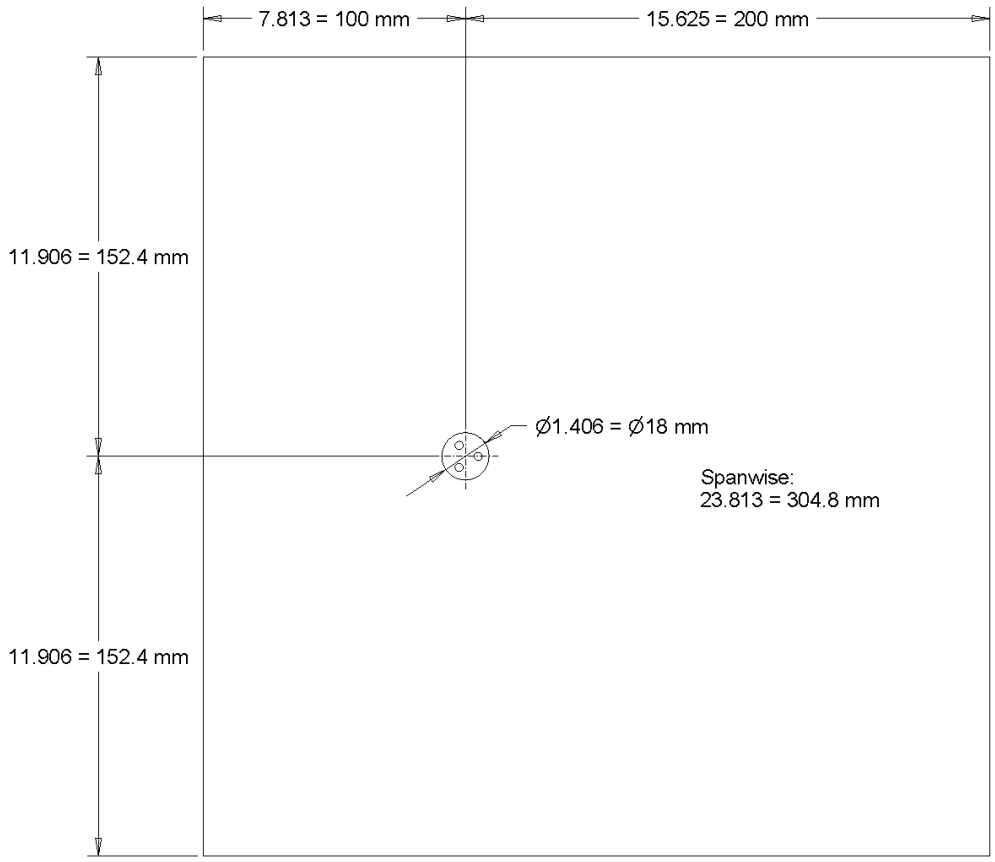

Figure 6.1. Original geometry

Nondimensionalizing by the setup diameter (of a circle circumscribing all three cylinders), this domain has a vertical dimension of 23.813, spanwise dimension of 23.813, and streamwise dimensions of 7.813 and 15.625 upstream and downstream of the setup central axis, respectively. The diameter of the rotating interface between stationary and rotating domains is 18. Dimensions of the cylinder setup itself match the specifications of the wind tunnel setup and remained the same throughout modifying other aspects of the geometry. More detailed dimensions of the rotating domain are shown in Figure 6.2.

The vertical dimension was originally chosen to match the height of the wind tunnel used in the experiments. However, after running several test simulations it was found that much of the domain in this direction is unnecessary as the flow is nearly uniform for much of its height.

The final geometry was reduced to a vertical dimension of 4. The spanwise dimension was also originally chosen to match the wind tunnel's size, but a first attempt at mesh generation found this to be far too computationally prohibitive. Instead, the spanwise dimension was reduced to use periodic boundary conditions instead of walls based on the suggestion of Menter to provide at least two characteristic lengths in the spanwise direction to properly allow scale resolution (F. Menter, Kuntz, & Bender, 2003). This begs the question of what to use as characteristic length for this estimate—the setup diameter or individual cylinder diameter. Research has shown that the behavior of the flow downstream of three-cylinder flows, including the size of the flow structures, is largely dependent on the spacing ratio, s, between cylinders (spacing non-dimensionalized by single cylinder diameter). In a study of the flow over equilateral three-cylinder arrangements by Bao et al., intermediate gap spacings of $0.5 < S < 4$ were characterized by wakes that while immediately individual to each cylinder, interacted in different ways further downstream, even combining to form new flow structures (Bao et al., 2010). It is worth noting that in this study all cylinder arrangements remained static as opposed to the rotating setup of the present research. Taking these considerations, the entire arrangement diameter was chosen conservatively as characteristic length in determining spanwise dimension to ensure flow structures are not stifled. The upstream streamwise dimension was reduced to 3 as tests showed the inlet flow any farther upstream. The downstream streamwise dimension was modified to 8.359 to be just large enough to match PIV imagery of the close-up shots (with two cameras). The final geometry is shown in Figure 6.2.

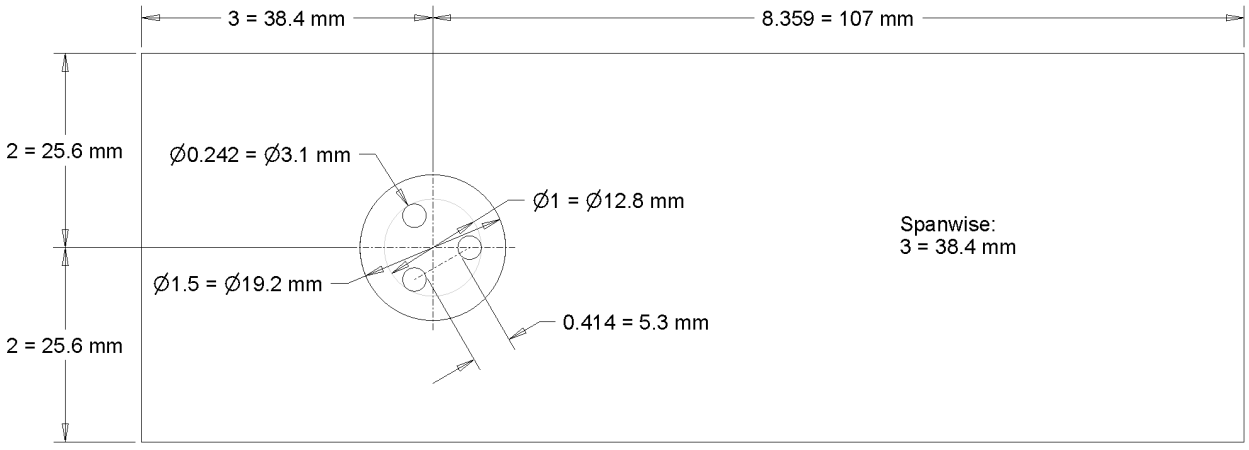

Figure 6.2. Final geometry

6.4. Mesh Generation and Refinement

Mesh refinement took place throughout the geometry iteration process as well as after the final geometry was selected. The final mesh is shown in Figure 6.3 with its node and element counts tabulated in Table 6.1. In the spanwise dimension are 161 evenly spaced nodes, which was found to be adequate to resolve instabilities in the flow. Mesh sizing around the cylinders is no larger than ~0.155 mm, per recommendation of 20 cells per characteristic length of the flow (for this estimation characteristic length was conservatively chosen as single cylinder diameter) (F. Menter, 2015). A first-layer height of 0.002 mm was inflated 36 cells from the cylinder walls, transitioning into the rest of the mesh. The $y+$ value was checked on solutions at the highest Reynolds number and was found to have a maximum value of 1.01 (and even lower for lower Re runs), confirming this choice. At the rotor-stator interface, sizing was matched between domains at ~0.155 mm, inflating slightly into the stationary domain O-grid. 160 nodes were distributed evenly surrounding each cylinder in the circumferential direction as recommended (Bao et al., 2010).

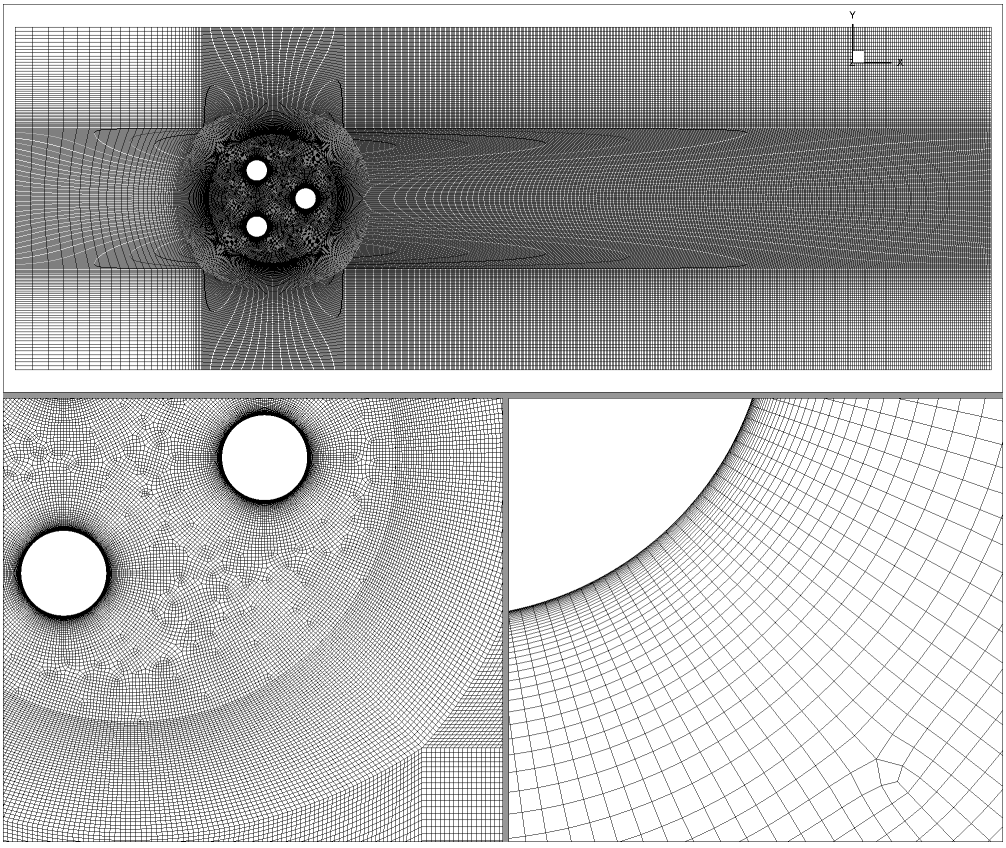

Figure 6.3. Final mesh

Table 6.1. Mesh parameters

Domain	Nodes	Elements
Stationary	21,404,160	21,106,456
Rotating	8,413,000	8,253,354
Total	29,817,160	29,359,810

6.5. Boundary Conditions and Setup

6.5.1. Boundary Conditions

A uniform normal velocity inlet boundary condition is specified according to the Reynolds number desired for each run, with medium (5%) turbulence intensity. Downstream of the flow, an outlet with zero average static pressure is specified. Entrainment opening boundary conditions are specified at the top and bottom of domain. Translational periodicity is applied on each side in the spanwise directions. A transient rotor stator interface is created linking the stationary and rotating domains. No-slip walls are specified at each cylinder's surface. An illustration of the boundary conditions defined is shown in Figure 6.4.

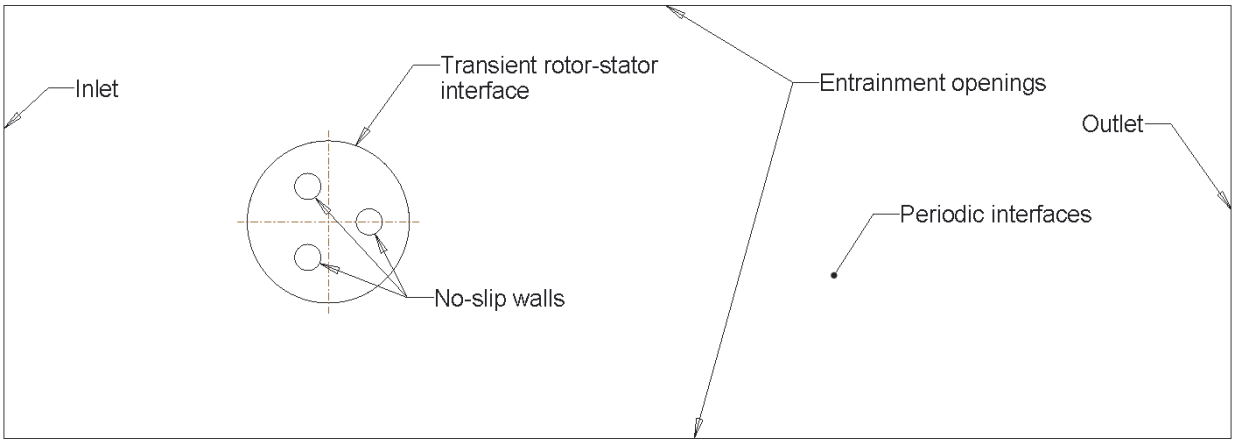

Figure 6.4. Boundary conditions

6.5.2. Solver and Timestep Options

Timesteps are estimated for each Reynolds number by

$$\Delta t = \frac{T_{tf}}{N \cdot CFL}, \quad T_{tf} = \frac{L}{U_\infty}, \tag{6.1}$$

where L is the domain length, U_∞ is the freestream velocity, and N is the number of cells passed in the domain length trajectory (F. Menter, 2015). A CFL of 1 was specified and monitored so that the timesteps could be adjusted. The final timesteps used are given in Table 6.2. A bounded central difference scheme is used for convection terms to reduce wiggles in the solution (F. Menter, 2015). A second order backward Euler transient scheme is used for time differencing.

Table 6.2. Timesteps used

Re	Δt (s)
57	1.2×10^{-4}
858	1.7×10^{-5}
7150	1.5×10^{-6}

7. RESULTS AND DISCUSSION

Here, the results of the study are presented and discussed. Essential to the discussion is the effect of differing Reynolds number and cylinder rotational speed on the flow, as well as the effect of the different CFD models used, SAS and SBES. The first several sections present the results of the primary three-cylinder simulations, including time-averaged quantities such as the statistical Reynolds stresses and velocity profiles, and instantaneous/time-dependent results such as the lift and drag coefficients on each cylinder and vortex visualization using quantities such as vorticity and Q-Criterion. Much experimental data from Ullah et al. is presented in conjunction with these results for comparison and validation (Ullah et al., 2020). The several sections following serve to bring together a discussion on the effect of the key variables—Reynolds number, rotation rate, and turbulence model selection. Finally, an analysis of the computational cost is given for the different cases run.

Unless otherwise denoted, results are shown in non-dimensional form for clarity as well as ease of comparison between different cases. Characteristic length is chosen as the entire cylinder arrangement's size as defined by a circle circumscribing all three cylinders; $D = 12.8$ mm. Velocities are non-dimensionalized by the freestream velocity based on the Reynolds number of the run, shown in Table 7.1. Note that in the experimental results freestream velocities were found to be slightly higher than expected, so these slightly higher values found from examining the results were used in non-dimensionalization. Statistical Reynolds stresses are non-dimensionalized by the freestream velocity squared.

Table 7.1. Freestream velocity values for CFD and PIV

Re	$(U_\infty)_{CFD}$ (m/s)	$(U_\infty)_{Exp}$ (m/s)
57	0.29	0.39
858	4.365	4.75
7150	36.376	41.5

7.1. Statistical Reynolds Stresses

The statistical Reynolds stresses are calculated for both the PIV and CFD results. These results do not necessarily represent the Reynolds stresses modeled with RANS methods as the CFD models are hybrid and use LES-like techniques for much of the flow domain. By pure statistical definition however, these quantities do give a useful representation of the fluctuations within the flow, which gives an idea of the size of scales within the flow. The statistical Reynolds stresses can be calculated as follows,

$$R_{ij} = \overline{u_i' u_j'} \tag{7.1}$$

$$= \overline{u_i u_j} - \overline{u_i}\,\overline{u_j}. \tag{7.2}$$

For the PIV results, these averages were calculated over a total of 100 frames taken at a frequency of 15 Hz. While this would theoretically result in PIV stills taken only at specific cylinder locations throughout the rotation at 25 Hz and 50 Hz rotation rates, visual inspection of the raw PIV stills confirmed that slight discrepancies in the rotational speeds resulted in the 100 frames representing the entire cycle. For the CFD results, averages were calculated over all timesteps (several thousand) across an integer number of full rotations. Calculation was also delayed for the CFD computations until the flow and turbulent structures were able to initialize.

Note that the CFD results do not show the Reynolds stresses within the rotating domain for the rotating cases. This is a considerable challenge as the averaged quantities within ANSYS CFX stay "with the node" throughout the rotation, resulting in meaningless results. It is possible that this could be fixed by averaging quantities using velocities in the stationary frame instead; however there are still several challenges with this. First, during every timestep of rotation, the nodes do not directly replace each other. This creates a challenge in what location to use for averaging. Also, the ring shaped region that is at some points covered by one of the three cylinders will result in some areas being averaged over a different amount of timesteps than others. In any case—the PIV results do not show this region due to the area nearest the cylinders being blocked from the PIV images, so comparison would be impossible anyway.

7.1.1. Re=57

7.1.1.1. f=0 Hz

First the statistical Reynolds stresses for the case of $Re = 57$ and $f = 0$ are considered. Shown in Figures 7.1, 7.2, and 7.3 are Reynolds stress components R_{xx}, R_{yy}, and R_{xy} as calculated for the PIV and both models, SAS and SBES. The stresses from the CFD results were averaged over a total of 2.25 seconds for each model.

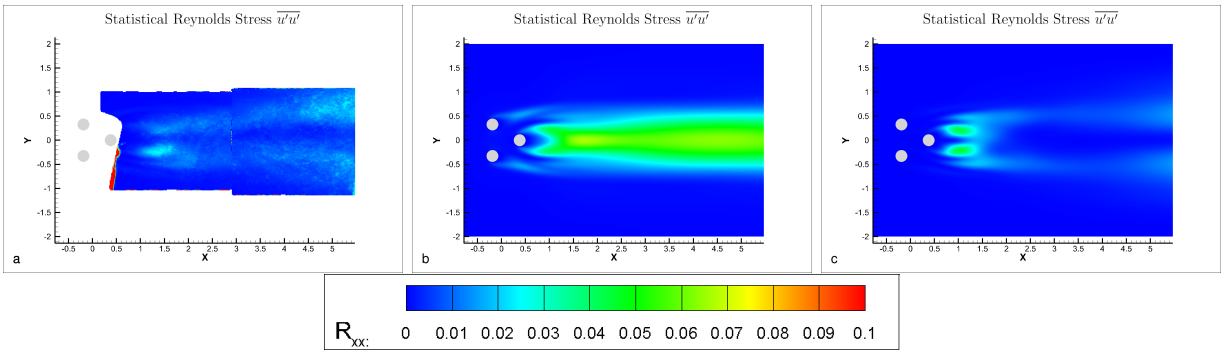

Figure 7.1. Statistical Reynolds stresses R_{xx} for Re=57, f=0 Hz using a. PIV, b. SAS, and c. SBES

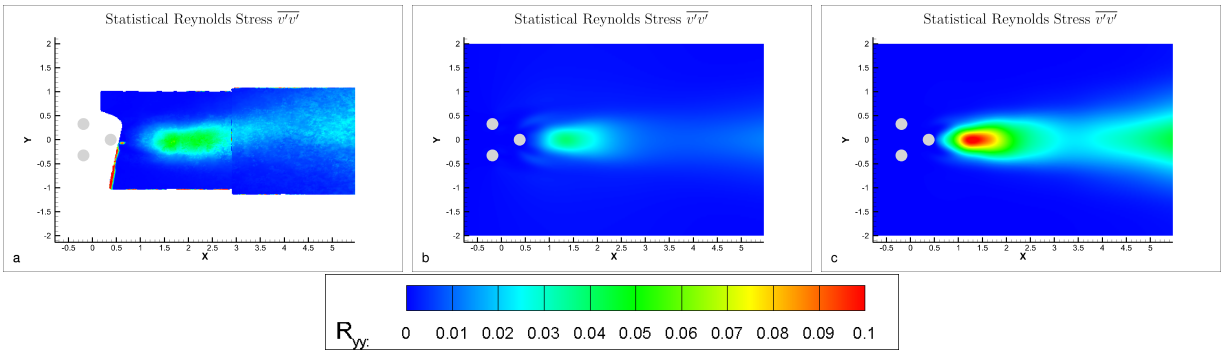

Figure 7.2. Statistical Reynolds stresses R_{yy} for Re=57, f=0 Hz using a. PIV, b. SAS, and c. SBES

Figure 7.1 shows that R_{xx} is quite accurately predicted in magnitude by the SBES model while the SAS model over-predicts R_{xx}. Figure 7.2 shows an opposite trend; the SBES model slightly over-predicts R_{yy}'s magnitude while SAS under-predicts. This suggests that while the SAS model contains larger fluctuations in the streamwise (x) direction, the SBES model contains larger

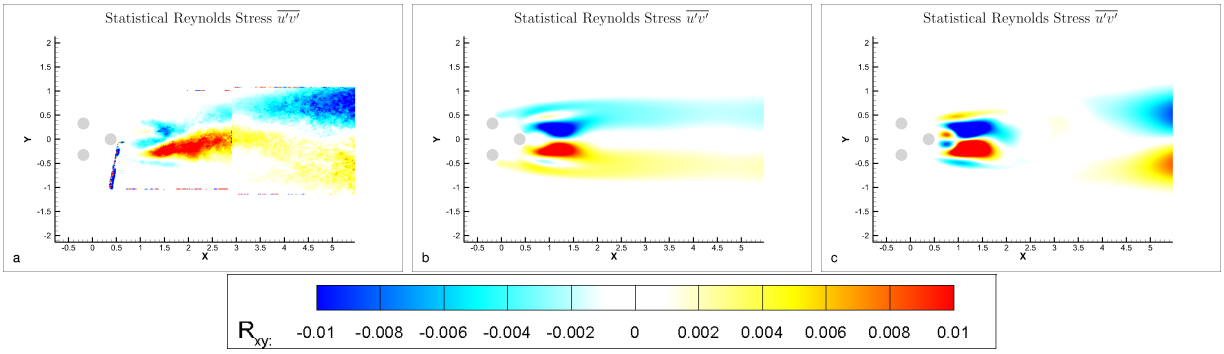

Figure 7.3. Statistical Reynolds stresses R_{xy} for Re=57, f=0 Hz using a. PIV, b. SAS, and c. SBES

fluctuations in the vertical (y) direction. Figure 7.3 shows similar results for prediction of R_{xy} between the models, although the SBES model seems to better predict R_{xy} further downstream.

The computational results are extremely symmetrical while the PIV results, with the exception of that for R_{yy} in Figure 7.2 are not. This could be for several reasons. First, if the 100 frames averaged disproportionally represented certain phases of the vortex shedding cycle, this would result in the averages being skewed. For example, in Figure 7.3a R_{xy} shows a larger magnitude of the stress below the x-axis, which could result from a large number of frames containing vortices in that region. Additionally, because of the extremely low Reynolds number, both SAS and SBES failed to resolve most of the smaller scale fluctuations within the flow while the PIV did capture some of these. This could also result in some asymmetry, although the primary reason is likely disproportions in the frame sampling.

With this being said, the magnitudes of the stresses, and their basic patterns in the flow are remarkably close between the PIV and CFD. This gives confidence that even in regions of flows where SAS and SBES are not utilizing their scale resolving capabilities, accurate 2D solutions (at least in terms of time-averaged quantities) are found thanks to the underlying SST model being used.

Finally, R_{zz} is shown in Figure 7.4 for comparison between the two CFD models (not available for the PIV as the experimental data is 2D). The extremely small magnitude of these stresses (more than $10^7\times$ smaller than R_{xx} and R_{yy}) confirms the two-dimensionality of the flow simulated. Flow structures are essentially non-resolved in the third direction. This can be visualized using quantities such as the Q-Criterion as is further down.

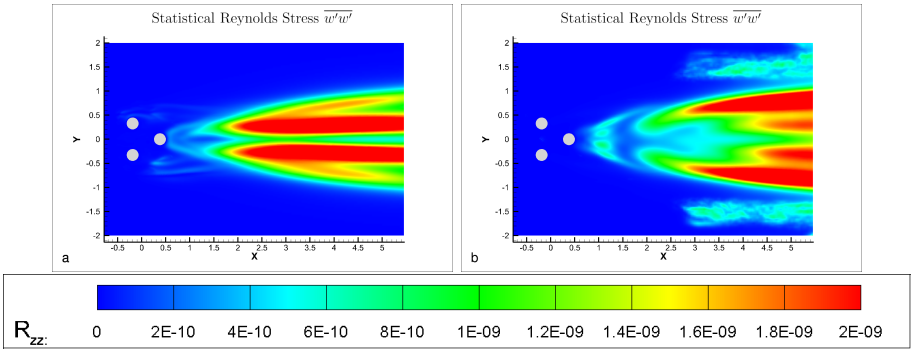

Figure 7.4. Statistical Reynolds stresses R_{zz} for Re=57, f=0 Hz using a. SAS, and b. SBES

7.1.2. Re=858

Next, consider cases for the mid Reynolds number flow at $Re = 858$. For the CFD solutions, averages were taken over a period of one full rotation, with 3–4 full rotations given to initialize the flow (this was more than enough time to develop the flow; however the averages were not output in early simulations, and solutions were continued from backups so they could be found).

7.1.2.1. f=25 Hz

First, R_{xx}, R_{yy} and R_{xy} are shown at $f = 25$ Hz in Figures 7.5, 7.6, and 7.7. There is some discrepancy in the magnitude of the stresses between the PIV and CFD. In all three plots, the CFD seems to overpredict their magnitude as compared to the PIV. As seen in Figures 7.5 and 7.7, there are no significant differences between the SAS and SBES models for prediction of R_{xx} and R_{xy} besides slightly less smooth solutions for SBES as a result if it resolving smaller structures. However, Figure 7.6 does show SBES predicting R_{yy}'s magnitude more accurately than SAS. Both the PIV and CFD suggest an asymmetry of R_{yy} favoring the top side due to the rotation of the cylinders.

R_{zz} is shown in Figure 7.8 for comparison between the two CFD models. Unlike the $Re = 57$ solutions, the magnitude of R_{zz} is substantial here, similar to or even greater than R_{xy}. This is due to the models utilizing their scale resolving capabilities to resolve structures in three dimensions.

7.1.2.2. f=50 Hz

Next, R_{xx}, R_{yy} and R_{xy} are shown at $f = 50$ Hz in Figures 7.9, 7.10, and 7.11. Again, the CFD over-predicts each component of the stress to a degree, and the SBES model outperforms SAS in matching the magnitude of R_{yy} as seen in Figure 7.10. While SAS and SBES show similar

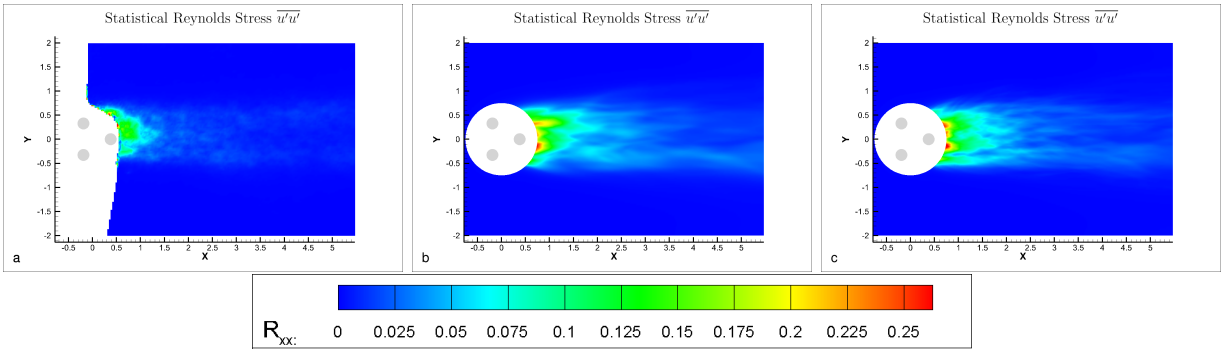

Figure 7.5. Statistical Reynolds stresses R_{xx} for Re=858, f=25 Hz using a. PIV, b. SAS, and c. SBES

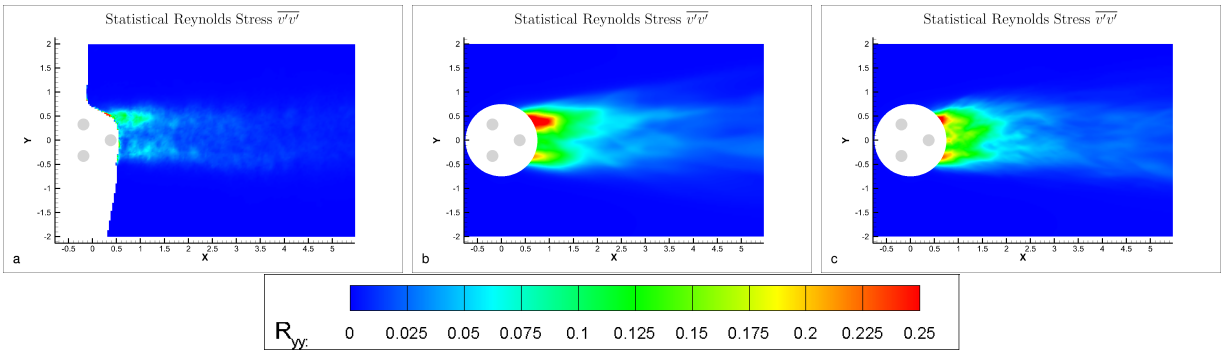

Figure 7.6. Statistical Reynolds stresses R_{yy} for Re=858, f=25 Hz using a. PIV, b. SAS, and c. SBES

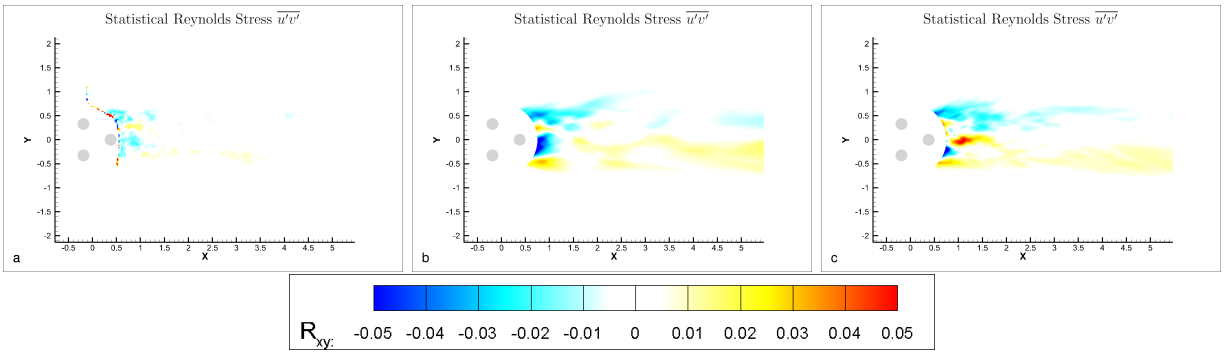

Figure 7.7. Statistical Reynolds stresses R_{xy} for Re=858, f=25 Hz using a. PIV, b. SAS, and c. SBES

predictions for R_{xy} when $f = 25$ Hz and $f = 50$ Hz (see Figures 7.7 and 7.11), the PIV shows a larger magnitude at $f = 50$ Hz, which results in a closer match to both the SAS and SBES models. SST matches the magnitude of R_{xx} closely, but performs less well at predicting R_{yy} and R_{xy}. The more "smoothed" contours of SST are due to the lack of small scales being resolved as are with SAS and SBES.

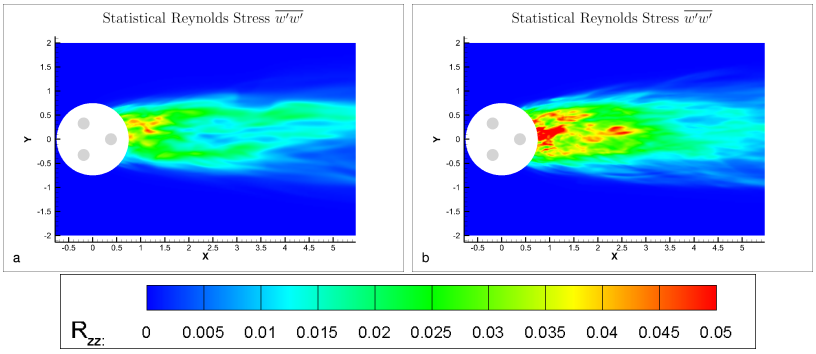

Figure 7.8. Statistical Reynolds stresses R_{zz} for Re=858, f=25 Hz using a. SAS, and b. SBES

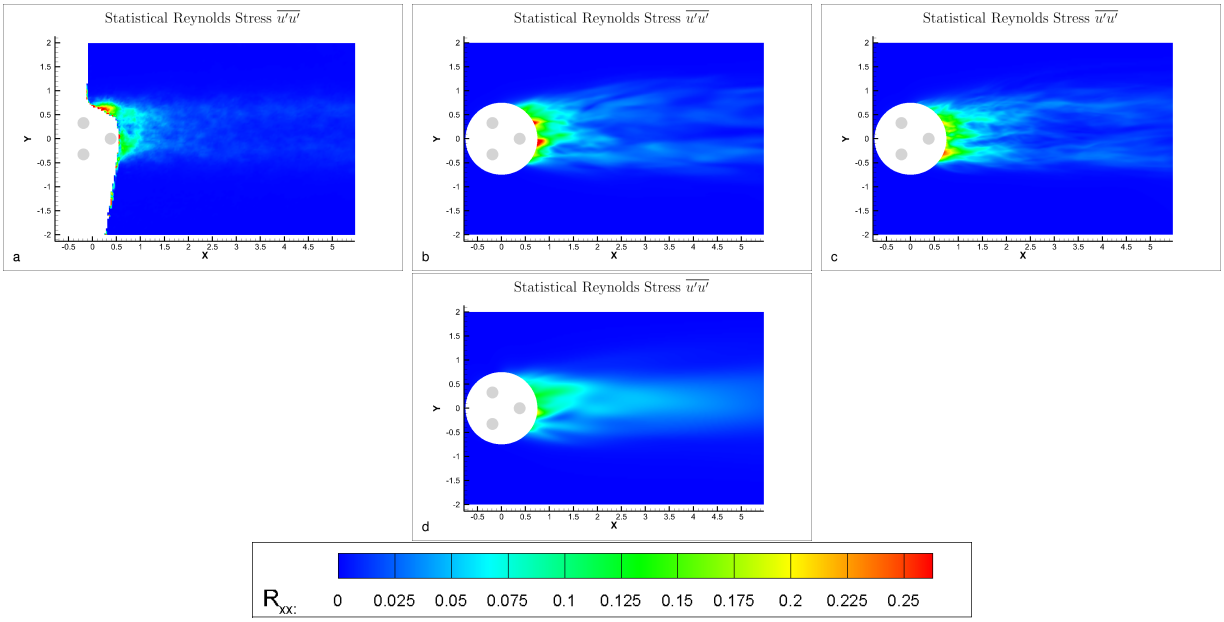

Figure 7.9. Statistical Reynolds stresses R_{xx} for Re=858, f=50 Hz using a. PIV, b. SAS, c. SBES, and d. SST

R_{zz} is shown in Figure 7.12 for comparison between the three CFD models. These are similar to those found for $f = 25$ Hz, with the SBES model predicting a slightly larger magnitude of the stress than the SAS model. Again, both SAS and SBES utilize their scale-resolving capabilities, resulting in their significant magnitudes. SST however, does not resolve any turbulence in the spanwise direction as expected, and fluctuations are not seen. Once again this highlights the benefits of using a hybrid model over a pure RANS model.

7.1.3. Re=7150

CFD computations were run for one rotational speed, $f = 50$ Hz, at the high Reynolds number, $Re = 7150$. Averaging was started after 120 degrees of rotation for flow development

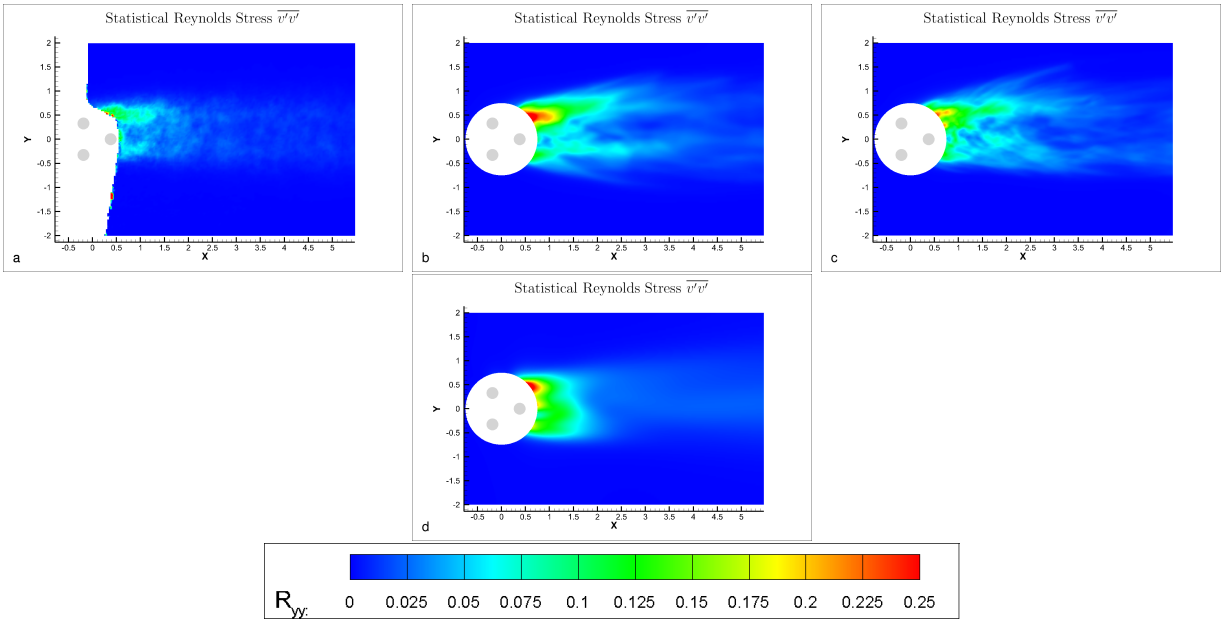

Figure 7.10. Statistical Reynolds stresses R_{yy} for Re=858, f=50 Hz using a. PIV, b. SAS, c. SBES, and d. SST

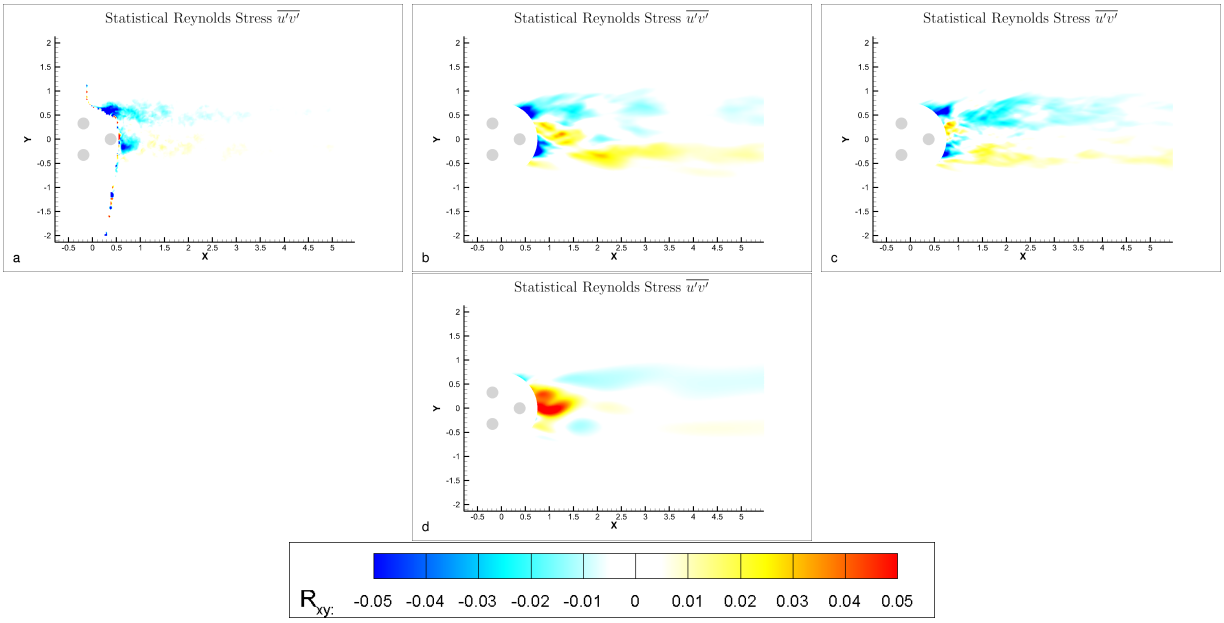

Figure 7.11. Statistical Reynolds stresses R_{xy} for Re=858, f=50 Hz using a. PIV, b. SAS, c. SBES, and d. SST

which was found to be adequate while monitoring the Q-Criterion and various flow quantities. Averaging continued for a total of one rotation.

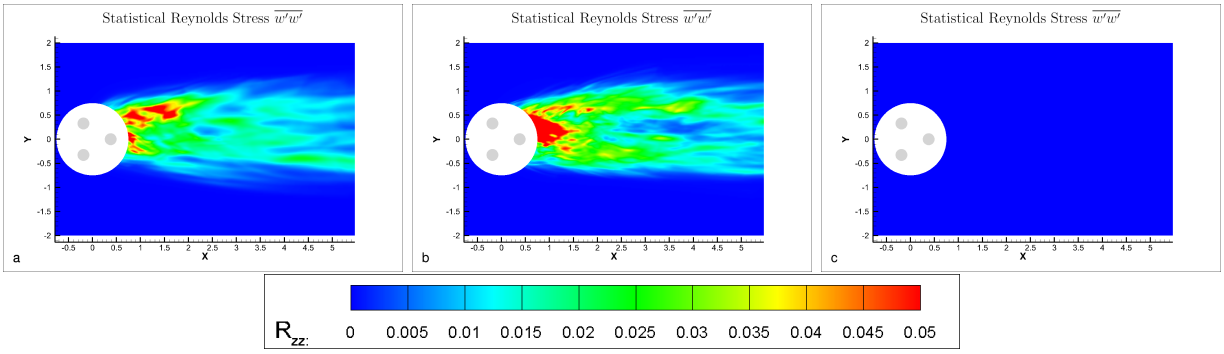

Figure 7.12. Statistical Reynolds stresses R_{zz} for Re=858, f=50 Hz using a. SAS, b. SBES, and c. SST

7.1.3.1. f=50 Hz

R_{xx}, R_{yy}, and R_{xy} are shown at $f = 50$ Hz in Figures 7.13, 7.14, and 7.15. It is immediately noticeable that the CFD solutions are much more symmetrical and smooth than those at $Re = 858$. At a higher Reynolds number, there are far more turbulent structures and scales passing through the domain over the course of one rotation which is likely the cause of this in addition to the fact that more timesteps are averaged over one rotation. Over-prediction of the stresses is still present in the CFD solutions, but not significant. R_{yy} shows a slight asymmetry similar to that at $Re = 858$ in the PIV results (see Figures 7.6, 7.10, and 7.14), which is this time not present in the CFD solution. If more than 100 frames were averaged over a uniform distribution of cylinder positions this would likely be diminished.

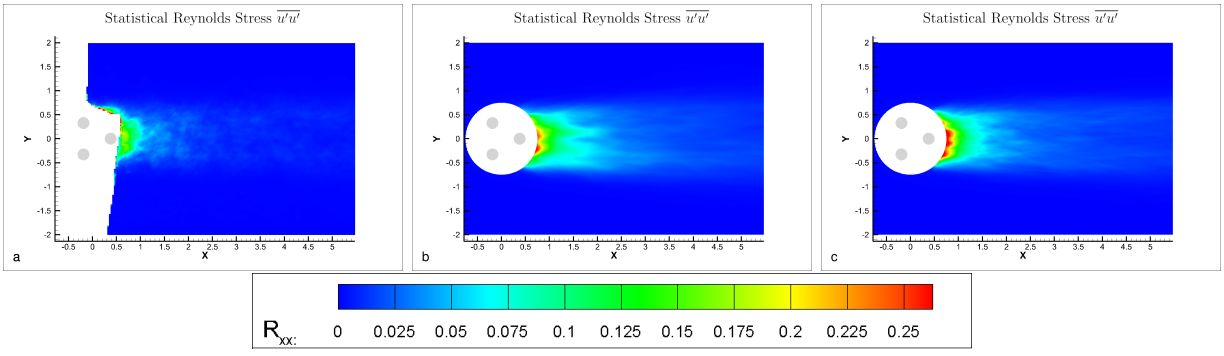

Figure 7.13. Statistical Reynolds stresses R_{xx} for Re=7150, f=50 Hz using a. PIV, b. SAS, and c. SBES

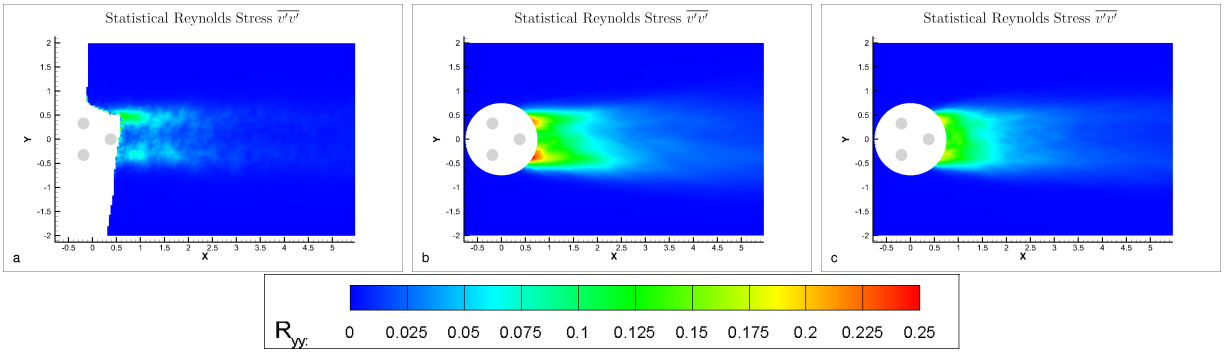

Figure 7.14. Statistical Reynolds stresses R_{yy} for Re=7150, f=50 Hz using a. PIV, b. SAS, and c. SBES

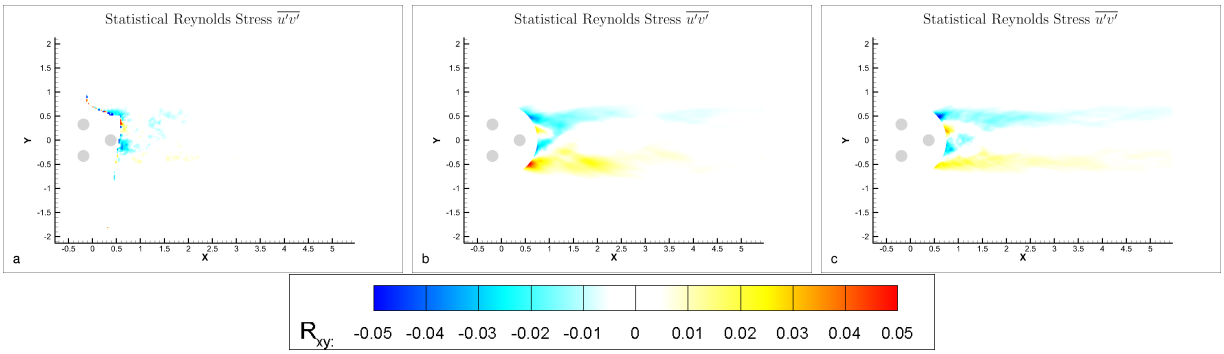

Figure 7.15. Statistical Reynolds stresses R_{xy} for Re=7150, f=50 Hz using a. PIV, b. SAS, and c. SBES

R_{zz} is shown in Figure 7.16 for comparison between the two CFD models. Here SBES shows a clearly larger magnitude of the stress than SBES. This is once again expected as it is able to resolve more scales in three dimensions than SAS does.

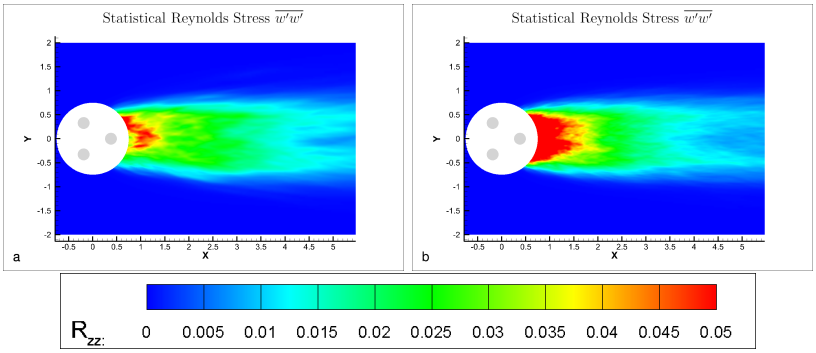

Figure 7.16. Statistical Reynolds stresses R_{zz} for Re=7150, f=50 Hz using a. SAS, and b. SBES

7.2. Time Averaged Velocity

In addition to the statistical Reynolds stresses, contours of average velocity are presented. These averages were taken over the same time as the statistical Reynolds stresses.

7.2.1. Re=57

Figure 7.17 shows the average u velocity for the static $Re = 57$ case. Note that in much of the dark blue regions, the average u velocity is actually negative—moving to the left. Both CFD models match closely with the PIV data. Slight differences can be seen in profiles extracted at distances of $X = 1$ and $X = 4$ downstream from the cylinder arrangement's central axis, shown in Figure 7.18. At $X = 1$, both models match the experiments extremely well, including the two secondary peaks caused by the wake around the furthest downstream cylinder. At $X = 4$, SBES shows a closer match to the experiments, both in the shape of the profile and its peak. This suggests that the SAS model allows the flow to dissipate more quickly in its return to a more uniform flow.

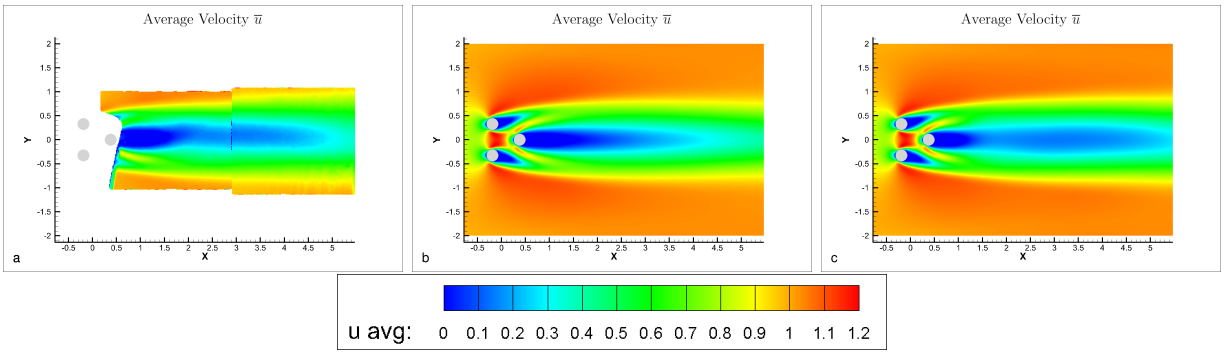

Figure 7.17. Average velocity $\overline{u}$ for Re=57, f=0 Hz using a. PIV, b. SAS, and c. SBES

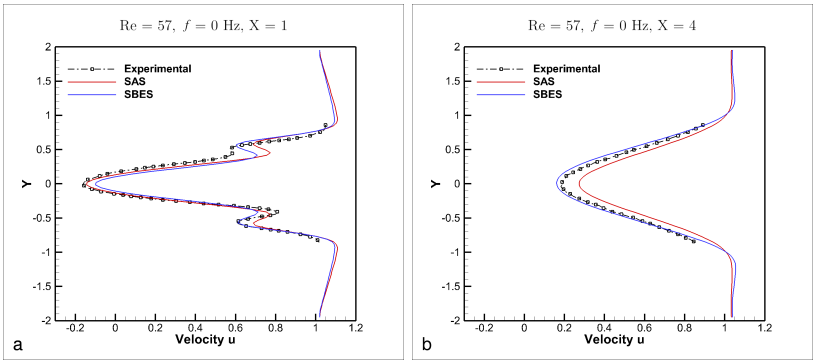

Figure 7.18. Velocity u profile for Re=57, f=0 Hz at downstream distances of a. X=1 and b. X=4

7.2.2. Re=858

7.2.2.1. f=25 Hz

Next, average u velocity contours are shown for $Re = 858$ and $f = 25$ Hz in Figure 7.19. Profiles are extracted at distances of $X = 1$, $X = 4$, and $X = 7$ downstream as shown in Figure 7.20. The contours show close agreement between the experimental results and both CFD models. Closer inspection of the profiles in Figure 7.20 shows better agreement for SAS at locations of $X = 4$ and $X = 7$ than SBES. Both predict similarly at $X = 1$, and while the double peak found in the experiments is seen in the CFD, it is less pronounced. It is important to remember that the experimental results are from a single center plane while the CFD results are averaged over 25 spanwise planes, which could explain the peaks being less pronounced. It is also worth noting that both CFD models show a slight "drift" in the average velocity profiles above the central axis at $X = 7$. This could be in part due to the opening boundary conditions set in the CFD simulations allowing flow to freely move towards the top and bottom of the domain, while the experiments may have a slight suppression imposed on the wake due to the wind tunnel walls

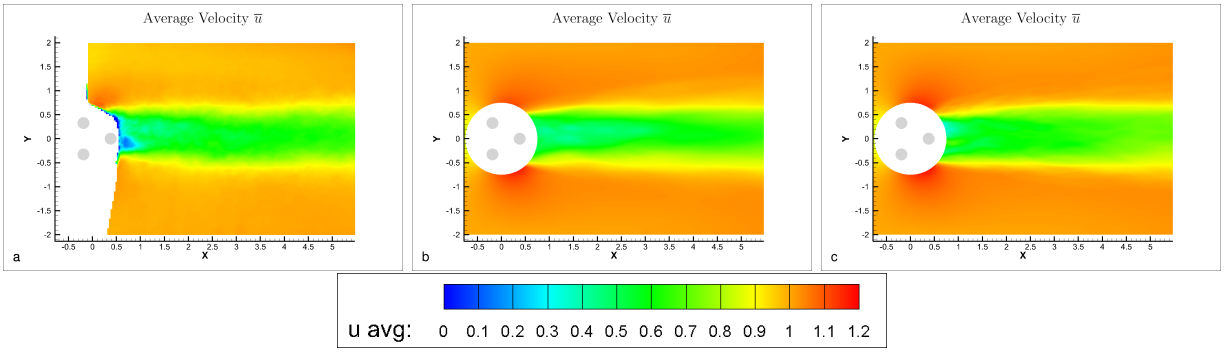

Figure 7.19. Average velocity $\overline{u}$ for Re=858, f=25 Hz using a. PIV, b. SAS, and c. SBES

7.2.2.2. f=50 Hz

Figure 7.21 shows the average velocity u contours for $Re = 858$ and $f = 50$ Hz. The contours seem to suggest the CFD, especially SAS, widening their wake where the experiments show a wake of relatively constant width. Looking at the extracted profiles in Figure 7.22 however, this does not seem to be the case, meaning it is likely just chance that the center frame shows this trend while other slices are averaging it out. Similar to the results at $f = 25$ Hz, the furthest

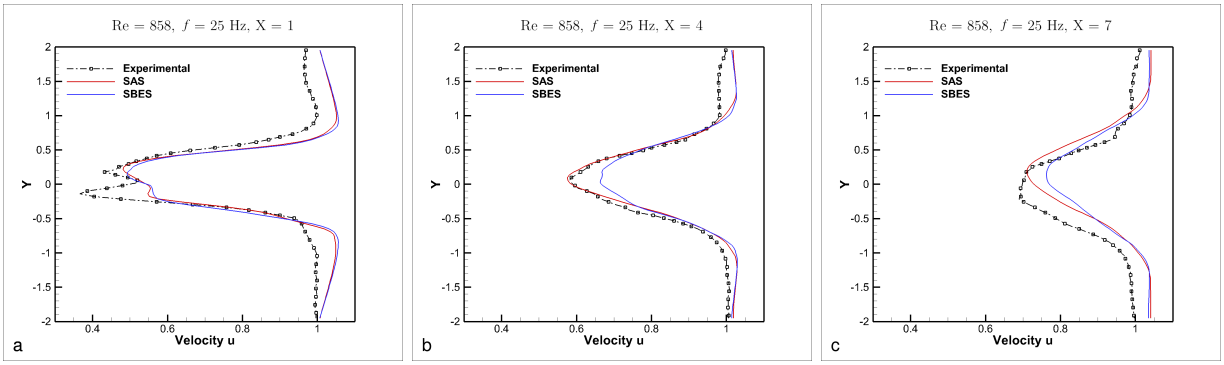

Figure 7.20. Velocity u profile for Re=858, f=25 Hz at downstream distances of a. X=1, b. X=4, and c. X=7

downstream profile at $X = 7$ shows a slight translation upwards of the CFD profiles not matched in the experiments. Again, this could be a result of the boundary conditions imposed on the CFD not perfectly matching with the reality of the wind tunnel's walls. SST shows a much more significant valley in the profile at $X = 1$, of approximately $u = 0$. It matches the experiments closely at $X = 4$, but then over-predicts velocity at $X = 7$. This shows that the SST model is more dissipative in nature and that even in prediction of average quantities, the hybrid models are superior.

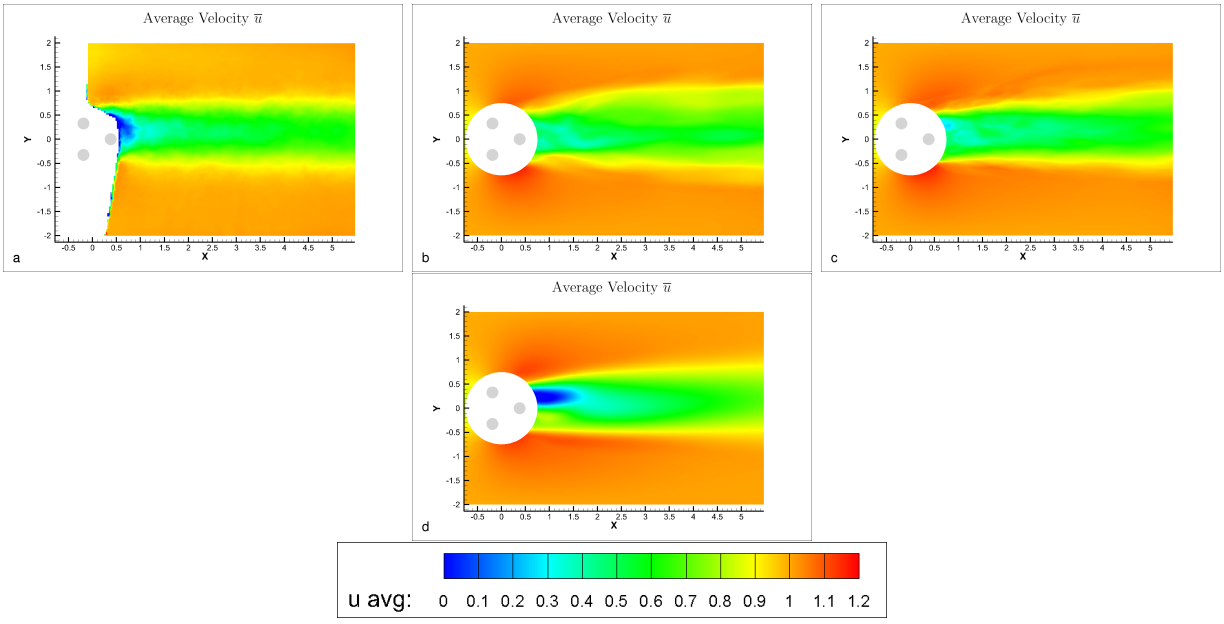

Figure 7.21. Average velocity $\overline{u}$ for Re=858, f=50 Hz using a. PIV, b. SAS, c. SBES, and d. SST

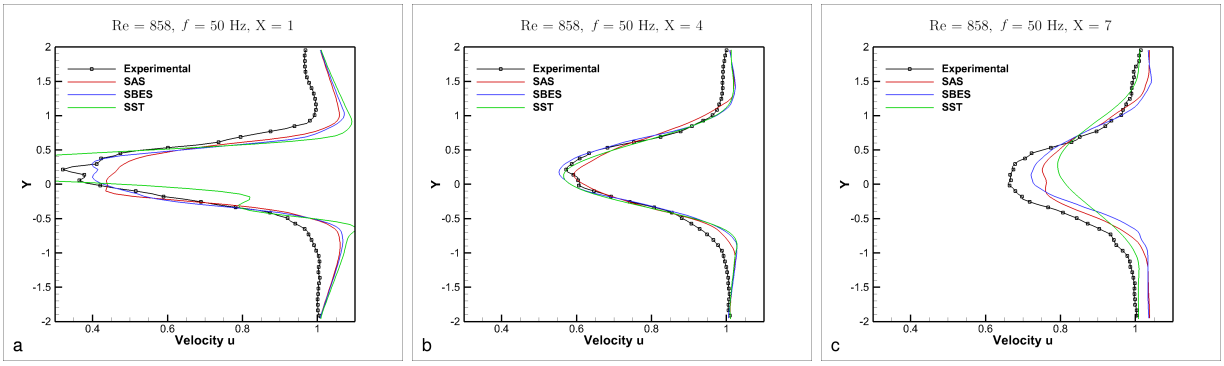

Figure 7.22. Velocity u profile for Re=858, f=50 Hz at downstream distances of a. X=1, b. X=4, and c. X=7

7.2.3. Re=7150

7.2.3.1. f=50 Hz

Finally, Figure 7.23 shows the contours for the case of $Re = 7150$ and $f = 50$ Hz. The widening of the CFD solutions is not seen here as it was at $Re = 858$, either in the contours or profiles of Figure 7.24. The solutions of SAS and SBES are almost indistinguishable here, again predicting the double peak at $X = 1$. One observation common to almost all profiles in this study (especially those closest to the cylinders) is of the CFD solutions "overshooting" the freestream velocity value near the edge of the wake, and returning to the freestream value at the opening boundary condition. This is due to the area of higher velocity surrounding the wakes that shed from cylinders near the top and bottom of the arrangement.

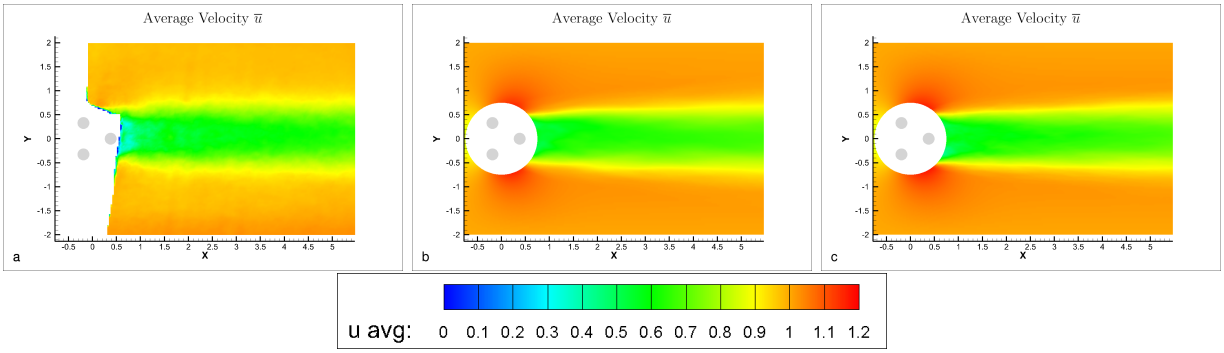

Figure 7.23. Average velocity $\overline{u}$ for Re=7150, f=50 Hz using a. PIV, b. SAS, and c. SBES

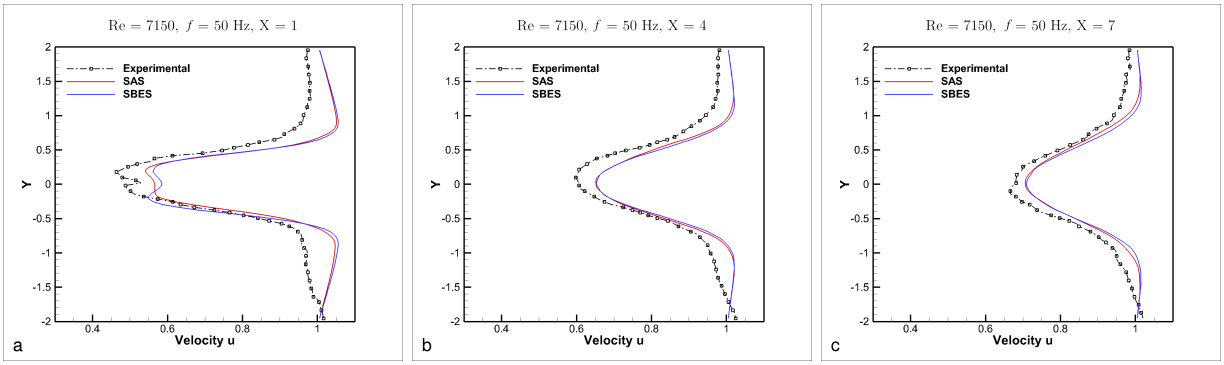

Figure 7.24. Velocity u profile for Re=7150, f=50 Hz at downstream distances of a. X=1, b. X=4, and c. X=7

7.3. Time Averaged Velocity and Statistical Reynolds Stress Error

To better quantify the performance of the models in terms of the average velocity and Reynolds stress, error is calculated on extracted lines along the x-axis ($Y = 0$) from $X = 0.75$ to $X = 5.75$ (at the mid-plane, $Z = 0$). Table 7.2 shows the errors. In general, $\overline{u}$ is slightly better predicted by SAS, although both SAS and SBES show very comparable results for average velocity. Error is significantly higher in predicting $\overline{u}$ at $Re = 57$ than the higher Re flows. This is primarily due to the fact that the region directly behind the cylinders contains nearly stagnant flow, numerically inflating the error to a degree because of division by near zero values. R_{xx} is better predicted using SBES for all cases, which speaks to its abilities to more accurately resolve fluctuations present in the flow. Finally, in comparison to both SAS and SBES, the pure RANS model (SST) shows significantly lower accuracy of $\overline{u}$ and R_{xx}.

The values of error for R_{xx} are seemingly large. This is to be expected to a degree as they are a second order turbulence quantity as opposed to the velocity components being first order. Additionally, with these values being close to zero, small differences in magnitude are more significant in percentage. To visualize these differences more clearly, the extracted profiles are shown in Figure 7.25. These plots are not entirely smooth as would be expected for averaged quantities. This is in some part due to the averaging techniques described for both the experimental and CFD results. For example, Figure 7.25b shows the experimental profile quickly decreasing to a value of approximately $R_{xx} = 0.02$, leveling off, and then decreasing suddenly from $X = 2.4$ to $X = 3$. It is likely that ensemble averaging over even more frames as well as assurance of equal sampling over the rotation would produce a much smoother profile. The CFD also shows fluctuating profiles.

Table 7.2. Percent error of average flow properties on an extracted line across the x-axis with lowest the lowest values of $\overline{u}$ and R_{xx} for each combination of Re and f underlined

Re	f	Model	$\overline{u}$	R_{xx}
57	0	SAS	<u>31.20</u>	1382.84
57	0	SBES	34.17	<u>94.62</u>
858	25	SAS	<u>8.09</u>	152.86
858	25	SBES	12.67	<u>127.55</u>
858	50	SAS	10.25	95.75
858	50	SBES	<u>9.88</u>	<u>65.78</u>
858	50	SST	15.57	284.97
7150	50	SAS	<u>9.21</u>	162.9
7150	50	SBES	9.31	<u>142.22</u>

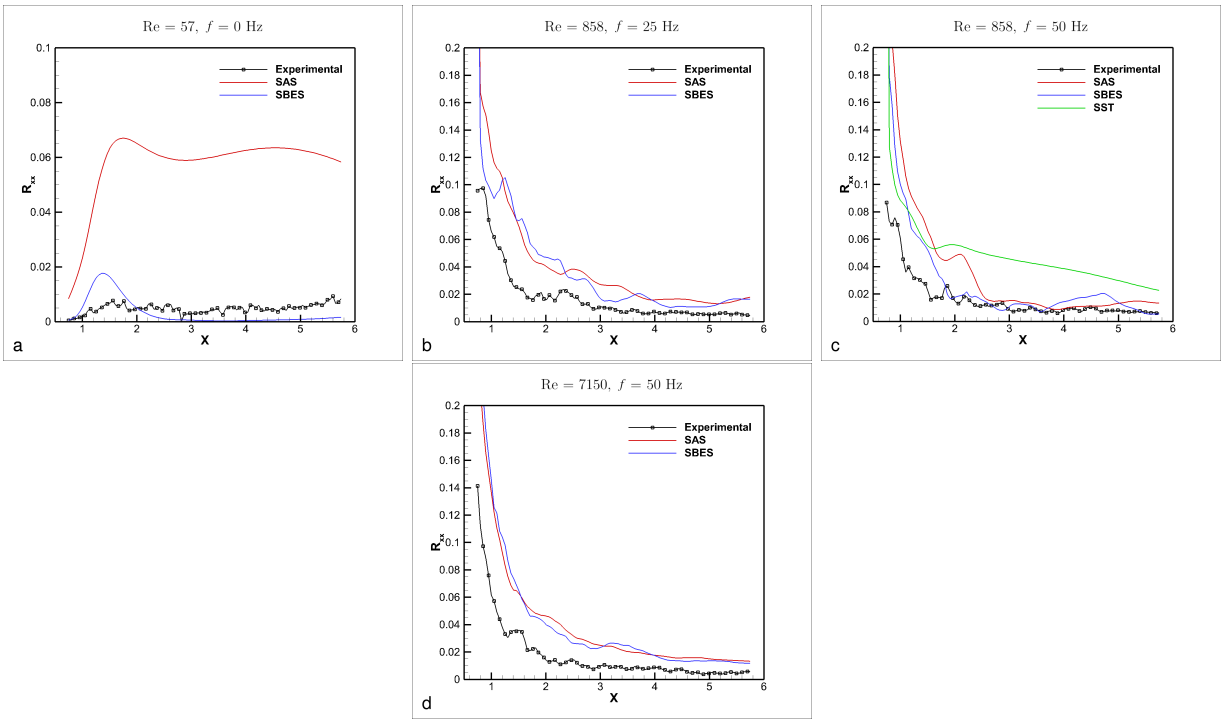

Figure 7.25. R_{xx} along x-axis downstream of the cylindrical arrangement for a. Re=57, f=0 Hz, b. Re=858, f=25 Hz, c. Re=858, f=50 Hz, and d. Re=7150, f=50 Hz

Allowing the simulation to run for a longer time and averaging over the course of a larger number of rotations would likely smooth their solutions much more.

7.4. Turbulence Intensity

If the time-averaged velocity components and Reynolds stresses are known, the turbulence intensity can be calculated. Turbulence intensity is defined by

$$TI \equiv \frac{\overline{u'}}{\overline{U}}, \tag{7.3}$$

where TI is the turbulence intensity, $\overline{u'}$ is the RMS of turbulent velocity fluctuations and $\overline{U}$ is the mean velocity,

$$\overline{u'} \equiv \sqrt{\frac{1}{3}\left(\overline{u'^2} + \overline{v'^2} + \overline{w'^2}\right)}, \tag{7.4}$$

$$\overline{U} \equiv \sqrt{\overline{u}^2 + \overline{v}^2 + \overline{w}^2}. \tag{7.5}$$

To determine mean turbulence intensity for a flow, this is simply done using the normal statistical Reynolds stresses to calculate $\overline{u'}$; for example, $\overline{u'^2} = \overline{u'u'}$.

The turbulence intensity gives a quantitative value to the strength of turbulence at a given point. Knowledge of this could be useful in an application such as generating turbulence for testing an airfoil, where the location at which the cylinders are placed could be chosen based on the desired turbulence intensity over the airfoil. This section shows the turbulence intensity from both experimental and computational results.

7.4.1. Re=57

7.4.1.1. f=0 Hz

First the case of $Re = 57$ and $f = 0$ Hz is shown in Figure 7.26. Figure 7.27 shows an extracted profile from the x-axis downstream of the cylindrical arrangement. As would be expected from the over-predicted Reynolds stresses, the turbulence intensity is somewhat over-predicted for both SAS and SBES. SBES shows a much closer match nearest the cylinders, but SAS seems to allow the turbulence to dissipate slightly more according to the experiments further downstream as is evidenced by Figure 7.27. The experiments show a peak turbulence intensity along the x-axis of about 42% while the SAS and SBES show peaks of 1432% and 185%, respectively. These high turbulence intensities are explained by looking at the average velocities in this region. As shown in Figure 7.18, the region of peak turbulence intensity coincides with a stagnant region of near zero

average u velocity. The average v and w velocity components in this region are also near zero, resulting in a near zero mean velocity of which the fluctuations are large in comparison, resulting in a large predicted turbulence intensity.

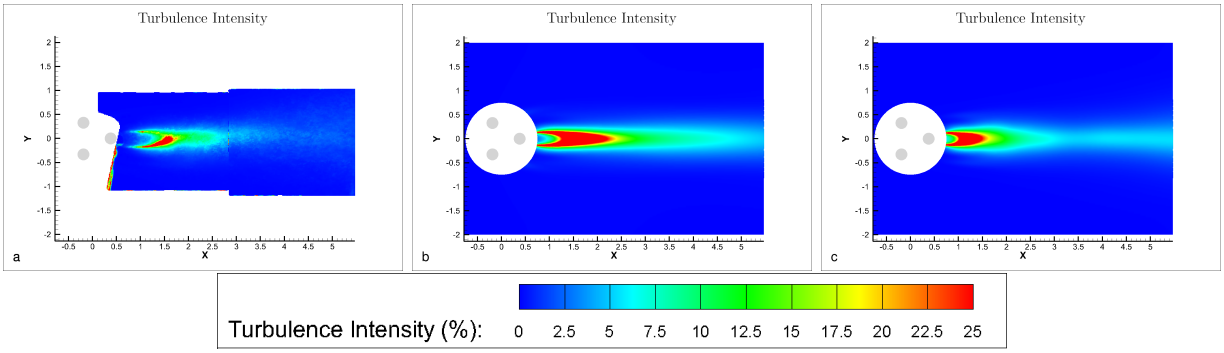

Figure 7.26. Turbulence intensity (in %) for Re=57, f=0 Hz using a. PIV, b. SAS, and c. SBES

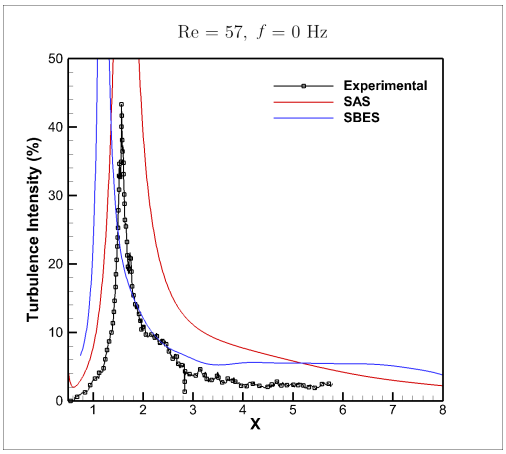

Figure 7.27. Turbulence intensity along x-axis downstream of the cylindrical arrangement for Re=57, f=0 Hz

7.4.2. Re=858

7.4.2.1. f=25 Hz

Next, consider the case of Re = 858 and f = 25 Hz. Figure 7.28 shows a slight over-prediction of the turbulence intensity just above the x-axis, similar to the over-predictions seen in the Reynolds stresses. Figure 7.29 shows close predictions of the peak turbulence intensity around $X = 0.75$, with the intensity increasing much more rapidly in the results than in the computations.

No significant difference is seen between the two models, both showing a slight over-prediction of turbulence intensity throughout the length of the domain. Some of this can be attributed to the fact that the turbulence intensity for the experiments was calculated using the 2D PIV results which do not include fluctuations in the third dimension.

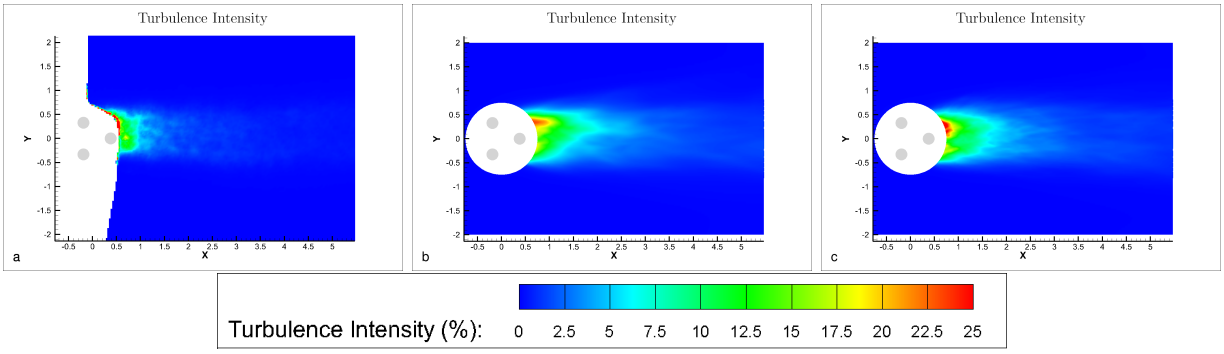

Figure 7.28. Turbulence intensity (in %) for Re=858, f=25 Hz using a. PIV, b. SAS, and c. SBES

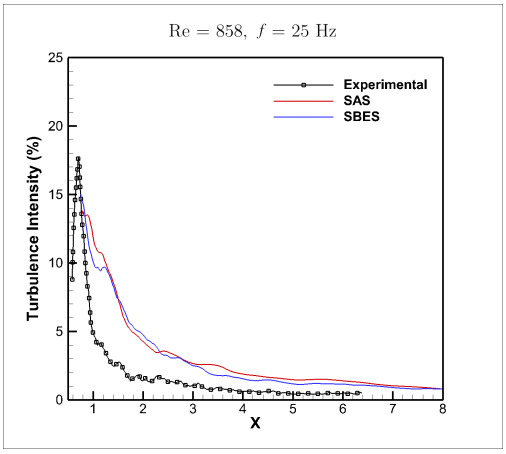

Figure 7.29. Turbulence intensity along x-axis downstream of the cylindrical arrangement for Re=858, f=25 Hz

7.4.2.2. f=50 Hz

The case of $Re = 858$ and $f = 50$ Hz contains results for the CFD models SAS and SBES, as well as the RANS model SST for comparison. Figure 7.30 shows the contours while Figure 7.31 shows the profiles along the x-axis. A slight over-prediction is seen by SAS and SBES similar to that for the $Re = 858$ and $f = 25$ Hz results, but the over-prediction by the SST model is much

more significant slightly above the x-axis. The profiles along the x-axis in Figure 7.31 do not reflect this massive over-prediction, but show similar results for the three models. SST shows a more gradual reduction in turbulence intensity throughout the domain while SST and SBES decrease more rapidly between $X = 1$ and $X = 3$ before leveling out around 1–2%. This more drastic reduction in this region reflects that seen in the experiments more closely than SST shows.

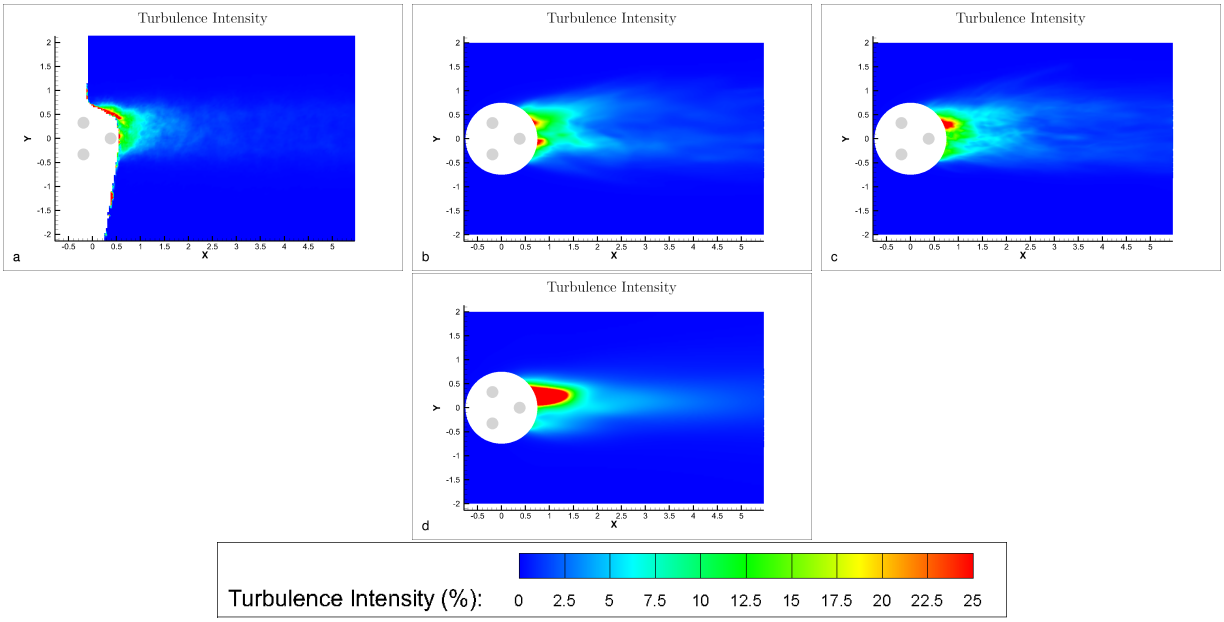

Figure 7.30. Turbulence intensity (in %) for Re=858, f=50 Hz using a. PIV, b. SAS, c. SBES, and d. SST

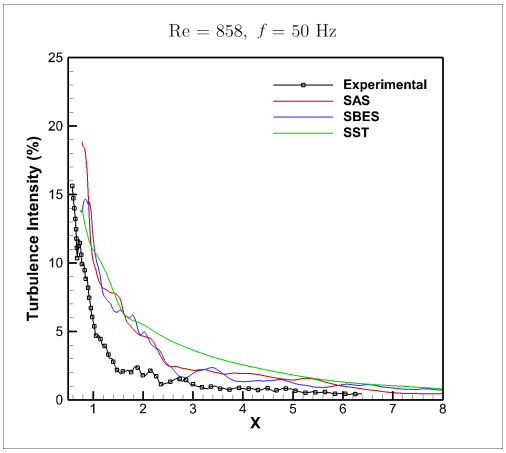

Figure 7.31. Turbulence intensity along x-axis downstream of the cylindrical arrangement for Re=858, f=50 Hz

7.4.3. Re=7150

7.4.3.1. f=50 Hz

Finally, consider the results shown for $Re = 7150$ and $f = 50$ Hz in Figures 7.32 and 7.33. The turbulence intensity is similarly predicted for both models. Again, this is slightly larger than the experimental results show throughout the length of the domain, which is in part due to the lack of spanwise fluctuations reflected in the PIV data. Both models predict a peak turbulence intensity of 16–18%, while the experiments show a peak of 17%.

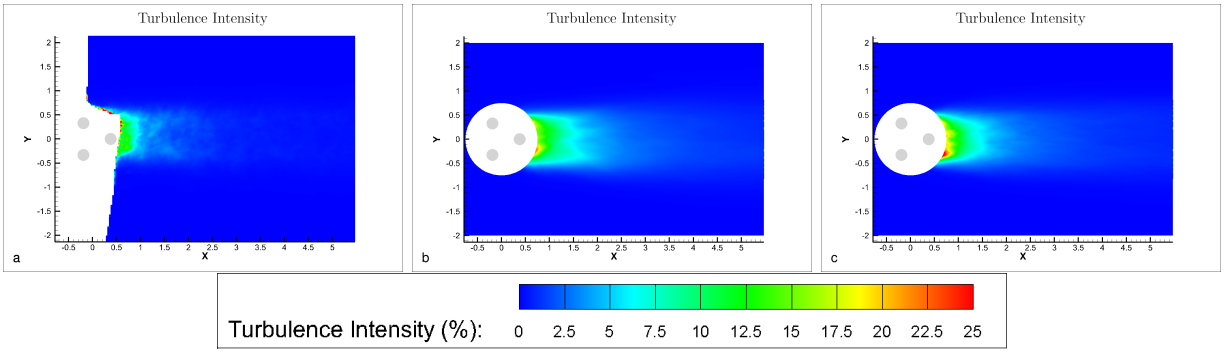

Figure 7.32. Turbulence intensity (in %) for Re=7150, f=50 Hz using a. PIV, b. SAS, and c. SBES

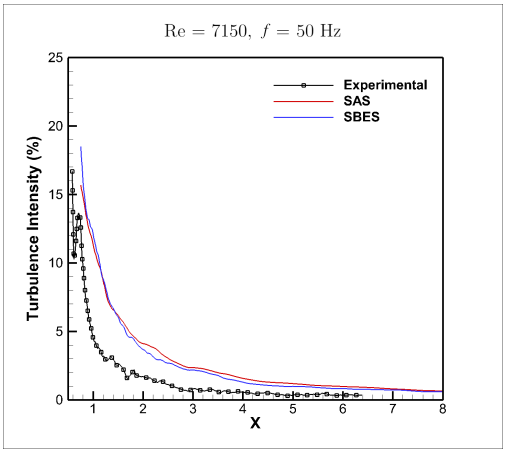

Figure 7.33. Turbulence intensity along x-axis downstream of the cylindrical arrangement for Re=7150, f=50 Hz

7.5. Lift and Drag

Although the forces on the cylinders are not available from any of the experiments, the lift and drag as calculated from the two CFD models is discussed below. Lift and drag coefficients can be found from the forces on the cylinder walls,

$$C_D = \frac{F_D}{\rho U_\infty^2 r b} \tag{7.6}$$

$$C_L = \frac{F_L}{\rho U_\infty^2 r b}, \tag{7.7}$$

where F_D and F_L are the drag and lift forces, respectively, ρ and U_∞ are freestream density and velocity, r is the cylinder radius and b is the span of the cylinder. The coefficient of drag on a cylinder at varying Re is a commonly researched quantity with an abundance of experimental data available. Figure 7.34 compiles an abundance of this data. Based on this data, C_D is expected to be just under 2 at $Re = 57$, around 1 at $Re = 858$, and just over 1 at $Re = 7150$. Sucker and Brauer provide a curve-fit equation for the data with accuracy up to $Re = 200,000$,

$$C_D \approx 1.18 + \frac{6.8}{Re^{0.89}} + \frac{1.96}{\sqrt{Re}} - \frac{0.0004Re}{1 + 3.64E - 7Re^2}, \tag{7.8}$$

which estimates values of $C_D = 1.60$, $C_D = 0.993$, and $C_D = 1.06$ for $Re = 57$, $Re = 858$, and $Re = 7150$, respectively (Sucker & Brauer, 1975). These values, while useful, should be taken with a grain of salt as the rotation within the flow will likely have an effect causing differences between this and a simple single cylinder experiment.

From the lift oscillations, a Fast Fourier Transform (FFT) is applied to find the dominant frequency and estimate the Strouhal number,

$$St = \frac{fL}{U_\infty}, \tag{7.9}$$

where f is frequency, L is characteristic length (single cylinder diameter in this case), and U_∞ is freestream velocity. Many experiments have been performed on the flow over a single cylinder in the study of their vortex shedding frequency as measured by the Strouhal number. A number of these

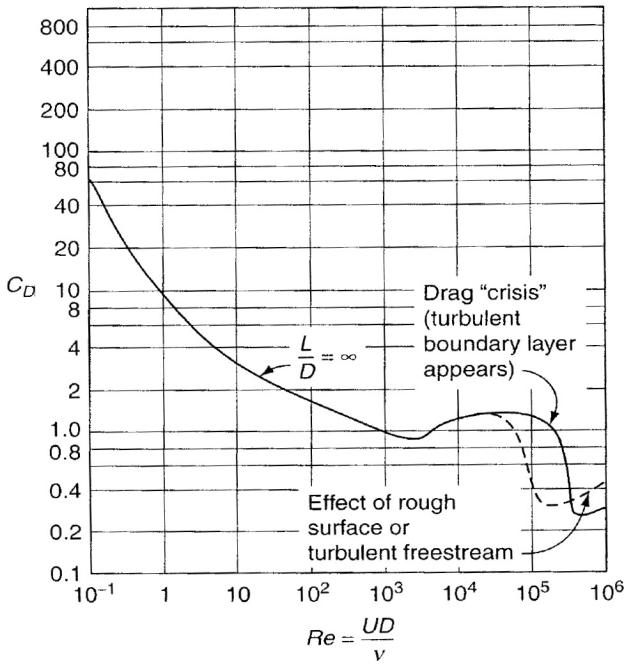

Figure 7.34. Drag coefficient over a circular cylinder as compiled from various experiments at different Re (White, 2006)

results are compiled in Figure 7.35. From this plot, we expect a Strouhal number of approximately 0.1 at $Re = 57$, and just over 0.2 at $Re = 858$ and $Re = 7150$.

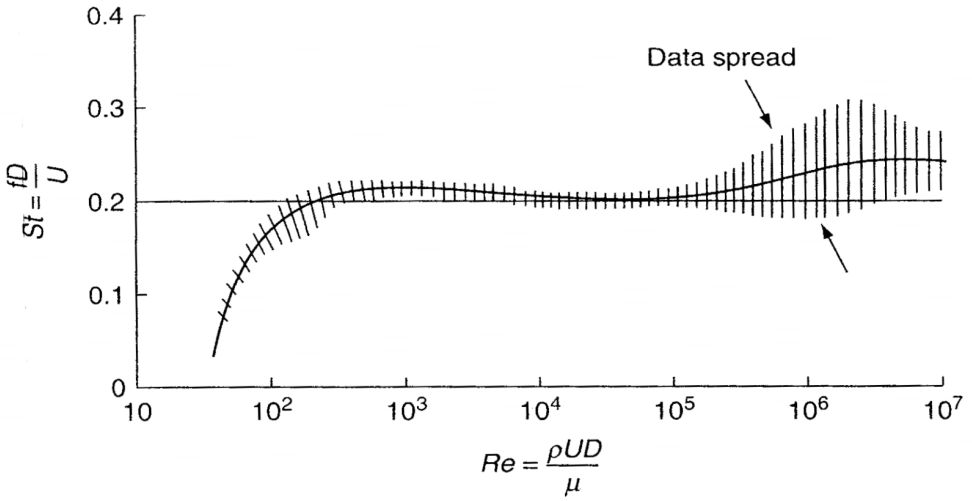

Figure 7.35. Strouhal numbers as compiled from various experiments at different Re (White, 2006)

7.5.1. Re=57

First, consider the lift and drag at $Re = 57$. Figures 7.36 and 7.37 both show a very periodic pattern to the lift and drag. Cylinders 1 and 3 (the two upstream cylinders) show shallow oscillations in comparison to Cylinder 2 in Figure 7.36. This is because the downstream cylinder's presence and wake suppresses the shedding off these cylinders from fully developing. Figure 7.37 shows that the upstream cylinders have higher drag than Cylinder 2. Interestingly, the drag on Cylinder 2 fluctuates at twice the frequency of the lift, while Cylinders 1 and 3 show the lift and drag oscillating at the same frequency. The Strouhal numbers as calculated from the dominant frequencies of the lift curves and time-averaged C_D are shown in Table 7.3. The Strouhal numbers are reasonably close to the value expected for a single cylinder, although some difference is not unexpected due to the influence of the additional wake interactions in the flow. The drag coefficients of Cylinders 1 and 3 are close to the expected value of 1.60, with that of Cylinder 2 being lower as previously discussed. There is very little difference between the two models, a result of them both essentially solving the entire flow in RANS mode.

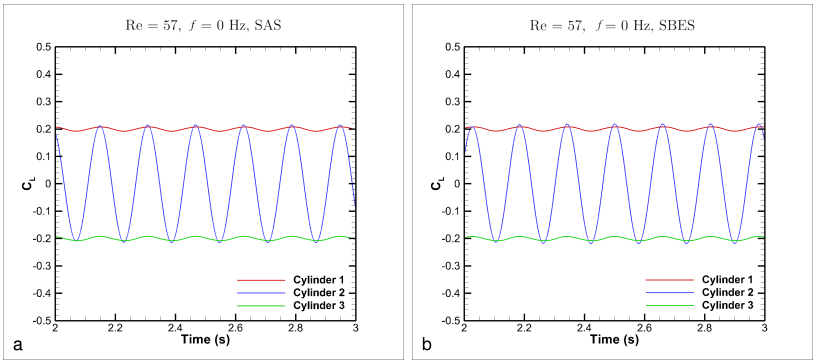

Figure 7.36. Coefficient of lift for Re=57, f=0 Hz using a. SAS and b. SBES

7.5.2. Re=858

7.5.2.1. f=25 Hz

Figures 7.38 and 7.39 show the lift and drag plots for a full, single rotation cycle for $Re = 858$ and $f = 25$ Hz. The drag plots in Figure 7.39 show prevalent patterns for both the SAS and SBES models over the rotation. For reference, consider the cylinders' positions for various phases of a rotation cycle shown in Figure 7.40. For an example, consider the drag on Cylinder 1 throughout

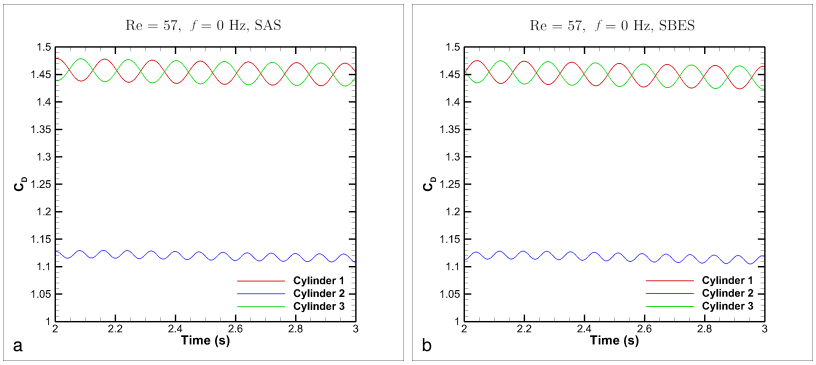

Figure 7.37. Coefficient of drag for Re=57, f=0 Hz using a. SAS and b. SBES

Table 7.3. Strouhal number and time-averaged C_D for each cylinder at Re=57, f=0 Hz

Cylinder	SAS		SBES	
	St	$\overline{C_D}$	St	$\overline{C_D}$
1	0.0684	1.453	0.0677	1.454
2	0.0684	1.119	0.0677	1.121
3	0.0684	1.453	0.0677	1.454
Net		1.342		1.343

a cycle. At $\theta = 30°$, Cylinder 1 is fully blocked from the direct freestream by Cylinder 2. This coincides with a low point of nearly zero drag in Figure 7.39. From approximately $\theta = 100°$ to $\theta = 200°$, Cylinder 1 shows higher drag than Cylinders 2 and 3. Figure 7.40 makes clear the reason for this—it is moving forward from the back of the arrangement, effectively adding to the relative freestream over that cylinder and therefore increasing drag. For the remainder of the cycle, the drag returns to a relatively constant, more moderate value mostly between Cylinders 2 and 3. This region of the cycle, from approximately $\theta = 240°$ to $\theta = 360°$ is its return to the back, or downstream position, free from any obstructions of the other cylinders that could cause large fluctuations in its drag. Following the cycle for either Cylinder 2 or 3 will show very similar trends, suggesting that the periodicity of a cycle is essentially broken into thirds (120° semi-cycles) of repetition between relative cylinders as would be expected due to the equilateral symmetry of the geometric arrangement.

One additional observation on the drag plots is a difference in the intensity of the fluctuations between the SAS and SBES models. The SAS model shows larger oscillations while the SBES model shows a slightly smoother graph, especially in the regions of peak drag for a cylinder. This may be

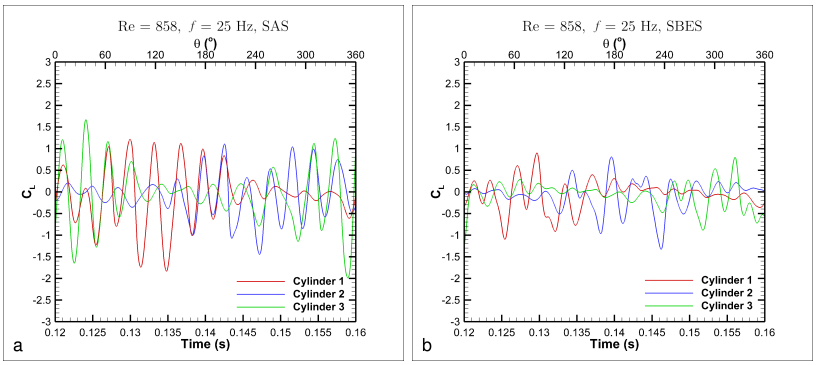

Figure 7.38. Coefficient of lift for Re=858, f=25 Hz using a. SAS and b. SBES

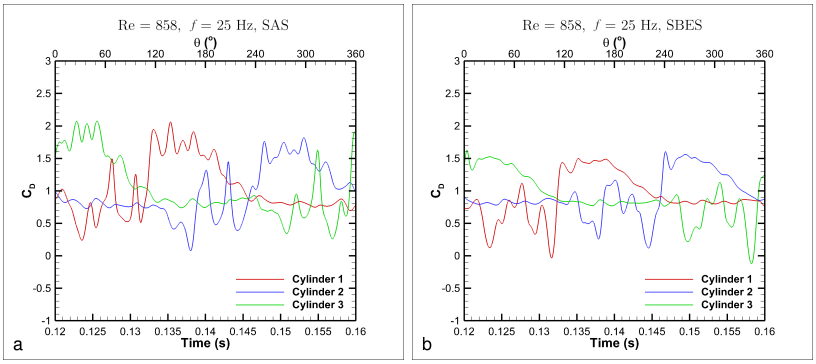

Figure 7.39. Coefficient of drag for Re=858, f=25 Hz using a. SAS and b. SBES

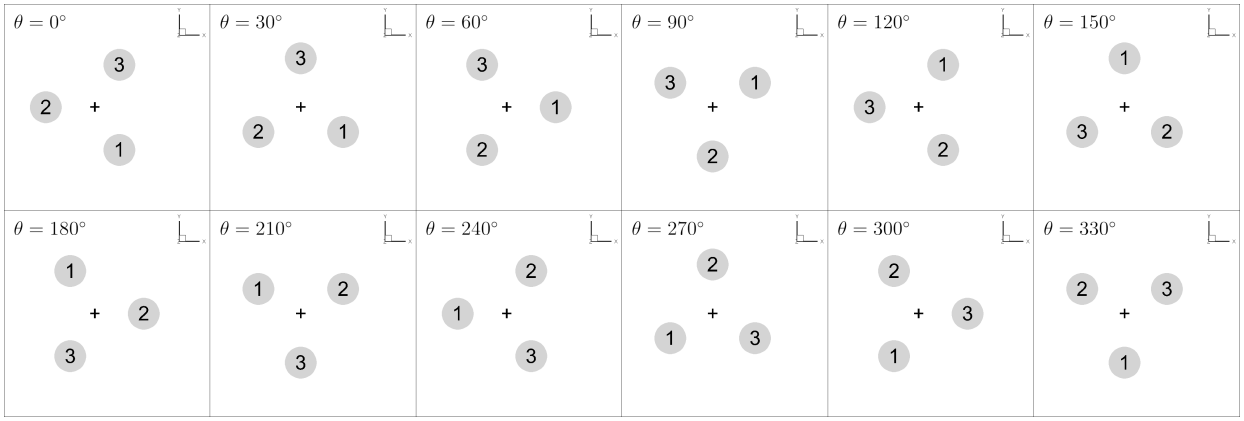

Figure 7.40. Cylinder locations throughout rotation cycle

in part due to the scales being resolved in the regions directly behind a cylinder. For example, SAS only allows somewhat large scales to be resolved directly behind a cylinder, which can play a large effect on the drag. SBES allows much smaller scales to be resolved directly behind a cylinder, which could play a role in damping the effects of a single large oscillation. For example, see Figure 7.41. The cylinder moving forward from the back of the arrangement's drag is likely considerably affected

by the large scales behind the cylinder using SAS, while the additional small scales resolved behind the cylinder in the SBES solution negate any large effects.

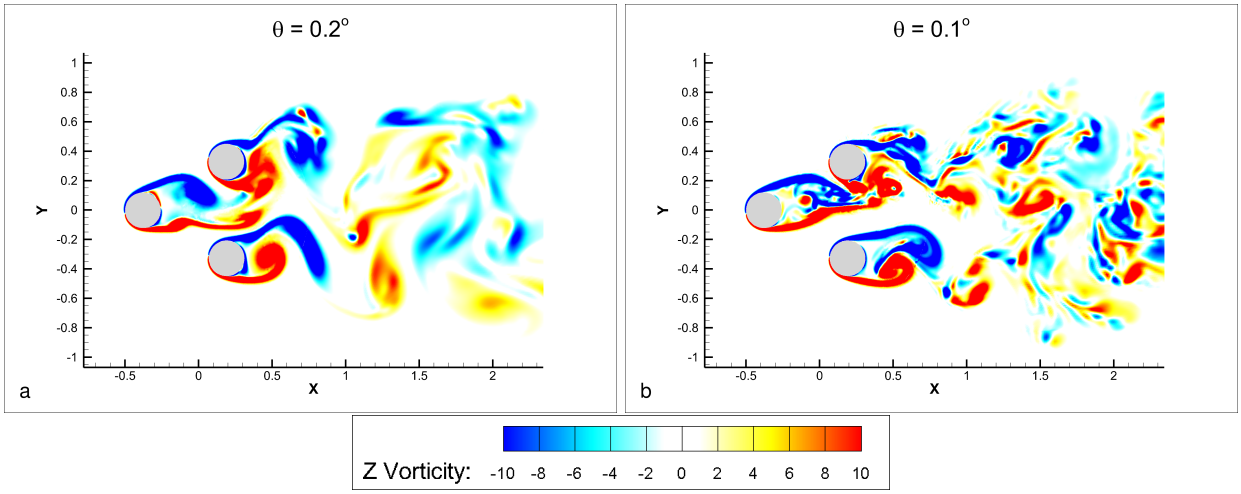

Figure 7.41. Vorticity Z contours for Re=858, f=25 Hz using a. SAS and b. SBES

As mentioned above, while the drag coefficient is calculated in the above plots under the assumption of a constant freestream velocity, the actual relative velocity over each cylinder is constantly changing throughout the rotation. To investigate this further, an adjusted value of C_D can be calculated by accommodating for the relative freestream over each cylinder,

$$(C_D)_{adj} = C_D \left(\frac{U_\infty^2}{(U_x + U_\infty)^2} \right), \tag{7.10}$$

where C_D is the drag coefficient calculated using the constant freestream velocity value of U_∞, and U_x is the x component of the velocity for an individual cylinder purely due to rotation,

$$U_x = 2\pi f r_c \sin\theta, \tag{7.11}$$

where f is the rotational frequency in Hz, r_c is the radius of a circle coincident with the three cylinders' centers, and θ is the cylinder's phase. Figure 7.42 shows the adjusted drag coefficients. While similar patterns as those seen in the non-adjusted C_D plots are seen, each cylinder shows a different region throughout the cycle of peak drag. For example, consider Cylinder 1, whose region of peak drag is now from roughly $\theta = 270°$ to $\theta = 15°$. Referencing its position again

in Figure 7.40, this is the region where it is moving towards the back of the arrangement, in the streamwise direction. This reduces the local freestream and local Reynolds number over the cylinder. Figure 7.34 shows that a reduction in Reynolds number is met with an increase in C_D (for $Re < 2000$ as is the case here). Relative minimums in C_D still correlate with regions where a cylinder is being blocked by a further upstream cylinder—for example at $\theta \approx 30°$ and $\theta \approx 90°$ for Cylinder 1.

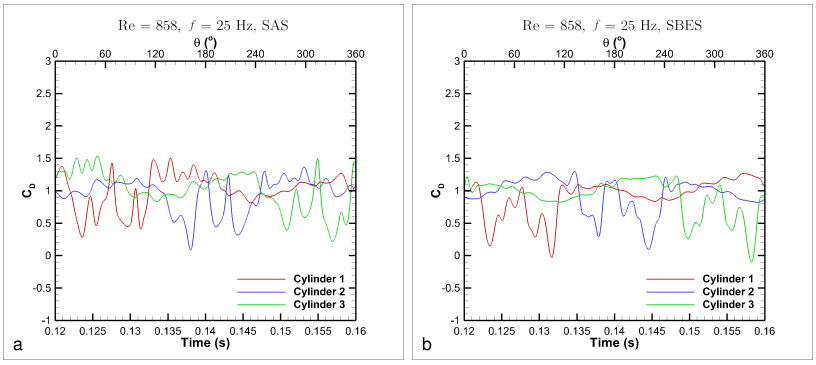

Figure 7.42. Relative freestream adjusted coefficient of drag for Re=858, f=25 Hz using a. SAS and b. SBES

Finally, the Strouhal numbers as computed from a FFT applied to the lift oscillations are shown in Table 7.4. As expected, values are in the range of slightly larger than 0.2. However, there is not complete agreement between the Strouhal number calculated between each cylinder. It is likely that running computations for a longer time would result in the dominant frequencies becoming more defined, and each cylinder would have the same calculated Strouhal number.

Table 7.4. Strouhal number and time-averaged C_D for each cylinder at Re=858, f=25 Hz

Cylinder	SAS		SBES	
	St	$\overline{C_D}$	St	$\overline{C_D}$
1	0.247	1.027	0.230	0.907
2	0.247	0.963	0.244	0.939
3	0.195	1.036	0.244	0.909
Net		1.001		0.918

7.5.2.2. f=50 Hz

Next, consider the lift and drag plots for $Re = 858$ and $f = 50$ Hz as shown in Figures 7.43 and 7.44. The drag plots in Figure 7.44 show similar trends to those described for $f = 25$ Hz, with peak drag occurring while the cylinders approach the front of the arrangement and least drag occurring when cylinders are obstructed from the freestream by another cylinder. Peak drag is also predicted slightly higher than at $f = 25$ Hz. This is due to the impact of increasing the local Reynolds number on a cylinder during its peak drag phase of the cycle being increased by a higher rotation rate. Unlike the lower f run however, no significant difference is seen in there being large fluctuations within the high drag phases.

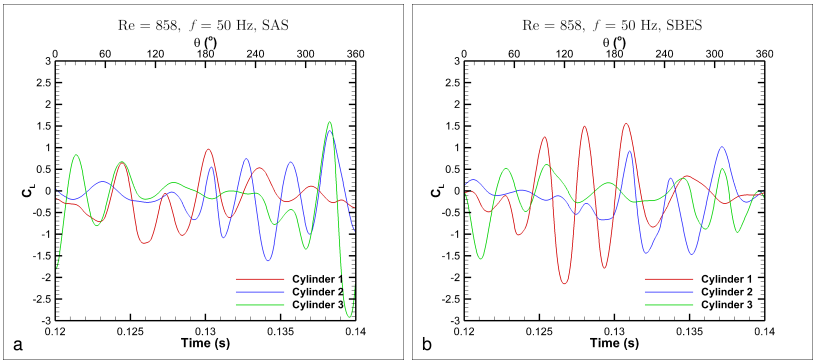

Figure 7.43. Coefficient of lift for Re=858, f=50 Hz using a. SAS and b. SBES

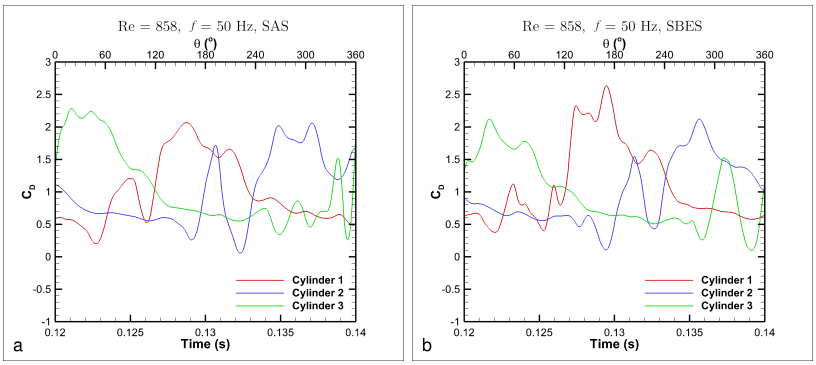

Figure 7.44. Coefficient of drag for Re=858, f=50 Hz using a. SAS and b. SBES

Relative freestream adjusted drag plots are shown in Figure 7.45. Similar trends are seen to those of f=25 Hz, but the increase in C_D is more significant during a cylinder's return to the

back of the arrangement. This is expected because the increase in f results in a much more drastic reduction in the local freestream and Re over the cylinder, resulting in a larger increase of C_D. For example, given the constant freestream of $U_\infty = 4.365$ m/s for $Re = 858$, $f = 50Hz$ can reduce this to as low as $U_{relative} = 2.85$ m/s, a reduction of 34.8% compared to a maximum reduction of 17.4% for $f = 25$ Hz.

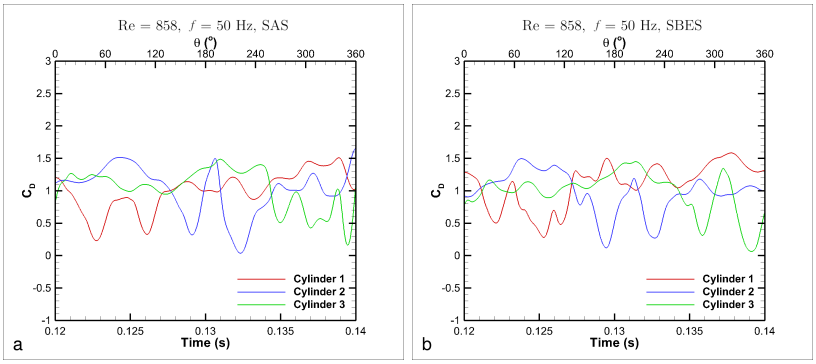

Figure 7.45. Relative freestream adjusted coefficient of drag for Re=858, f=50 Hz using a. SAS and b. SBES

The Strouhal numbers and time-averaged C_D are compiled in Table 7.5. Again, as expected values of St are slightly above 0.2, but perfect agreement is not found between all three cylinders. This is once again expected to be a product of the limited time for which the simulations were run. $\overline{C_D}$ is quite close to the calculated value of 0.993 for both models.

Table 7.5. Strouhal number and time-averaged C_D for each cylinder at Re=858, f=50 Hz

Cylinder	SAS		SBES	
	St	$\overline{C_D}$	St	$\overline{C_D}$
1	0.213	1.035	0.228	1.100
2	0.213	1.011	0.264	1.016
3	0.259	1.077	0.228	0.995
Net		1.041		1.037

7.5.3. Re=7150

7.5.3.1. f=50 Hz

Finally, consider the lift and drag plots for Re = 7150 and f = 50 Hz as shown in Figures 7.46 and 7.47. The drag plots show similar trends as those described for the Re = 858 cases, although the region of peak drag for each cylinder is less pronounced. This is because at a higher Reynolds number, the impact of the rotation in increasing the local Reynolds number on a cylinder is less significant.

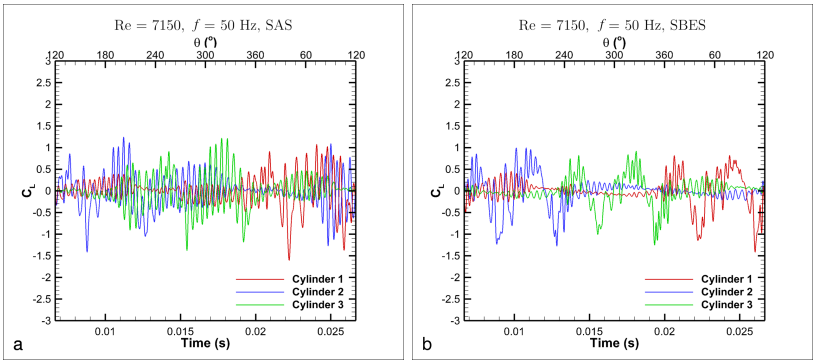

Figure 7.46. Coefficient of lift for Re=7150, f=50 Hz using a. SAS and b. SBES

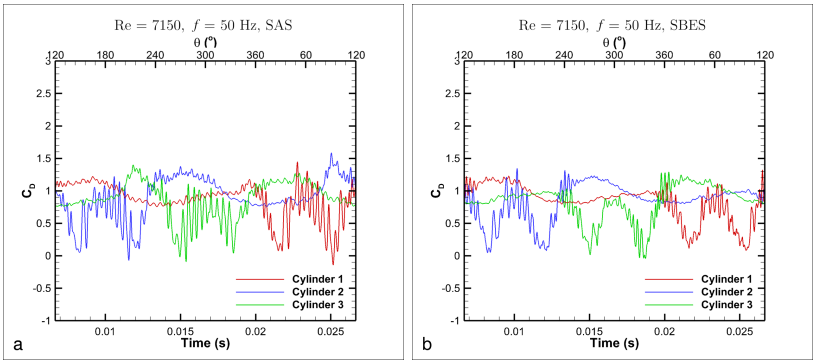

Figure 7.47. Coefficient of drag for Re=7150, f=50 Hz using a. SAS and b. SBES

Figure 7.48 shows the relative freestream adjusted drag plots. These look incredibly similar to the non-adjusted plots of Figure 7.47. This is due to the reduced impact of the velocity due to rotation on the local freestream—a maximum of only 4.2% change in the Reynolds number is possible. Only a slight compression of the C_D profiles towards their average values is visible.

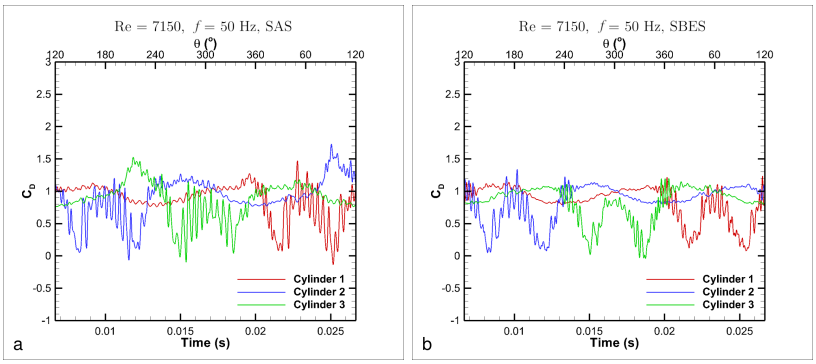

Figure 7.48. Relative freestream adjusted coefficient of drag for Re=7150, f=50 Hz using a. SAS and b. SBES

The Strouhal numbers and time-averaged C_D are compiled in Table 7.6. SAS predicts the Strouhal number in the expected area of slightly greater than 0.2. However, SBES predicts St at roughly 10× lower. The reason for this can be seen in the lift plots in Figure 7.46. As with the case of Re = 858 and f = 25 Hz, SAS shows oscillations of much greater magnitude than those of the same frequency for SBES. In addition, a lower frequency can visibly be seen in the plot for SBES. These two frequencies can be seen in the frequency spectrum, shown for Cylinder 3 as an example in Figure 7.49. Two peaks can be clearly seen—one of roughly 200 Hz and the larger of roughly 2000 Hz. Because the lower frequency dominates in this case, the Strouhal number is under-predicted.

Table 7.6. Strouhal number and time-averaged C_D for each cylinder at Re=7150, f=50 Hz

Cylinder	SAS		SBES	
	St	$\overline{C_D}$	St	$\overline{C_D}$
1	0.211	0.866	0.0256	0.839
2	0.198	0.905	0.0256	0.846
3	0.230	0.873	0.0192	0.832
Net		0.881		0.839

Considering the time-averaged C_D in Table 7.6, it is less than the calculated estimate of 1.060 in the case of both models. Whereas experiments have shown the drag to increase slightly between Re = 858 and Re = 7150, the opposite is predicted in the results. It is possible that implementing a transition model for cases above Re = 858 could benefit in this drag prediction.

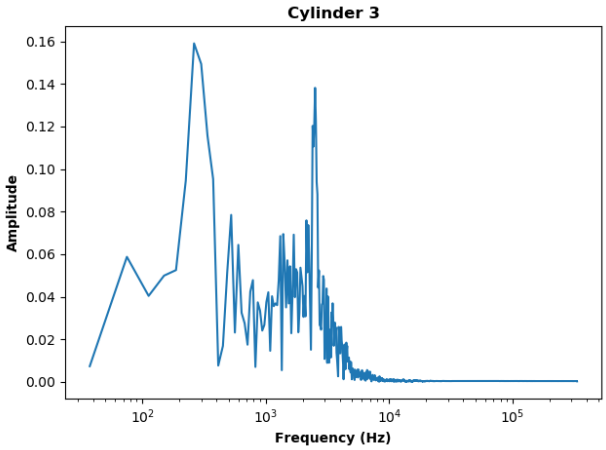

Figure 7.49. Frequency spectra for Cylinder 3 at Re=7150, f=50 Hz, SBES

7.6. Vorticity and Flow Structure Analysis

As mentioned in Section 2, the Kolmogorov length scale, $\eta_k \equiv \nu^{3/4}/\epsilon^{1/4}$, governs the smallest possible length scales within a flow. Without knowing the eddy dissipation rate, ϵ, an inviscid estimation can be made under the assumption of $\epsilon \approx U_\infty^3/\Lambda$ that

$$\eta_k \approx \Lambda Re^{-3/4}, \tag{7.12}$$

where Λ is the largest length scale present in the flow (assumed to be the characteristic length). Table 7.7 shows the minimum calculated Kolmogorov length scales within the flow for each of the cases run. η_k is both calculated from the ϵ found in the flow solutions as well as using the inviscid approximation for comparison. With the smallest grid spacing present in the flow being $2E-6$ m within the inflation layer, this suggests that a DNS solution for the highest Reynolds number flow would require much of that domain to be meshed at nearly that sizing. This emphasizes the importance of turbulence modeling techniques that do not require this strict of meshing requirements, leading to huge computational costs.

For analyzing the flow structures present in the rotating flow, the case of $Re = 858$ and $f = 50$ Hz is considered due to the fine time resolution of exported results. In addition, the SBES model is chosen due to the resolution of smaller scales giving more detail to the flow. 24 instantaneous frames of vorticity in the spanwise direction (Z vorticity) are shown in Figures 7.50–7.52 throughout the duration of a full rotation. Even in 2D, the vorticity contours offer many

Table 7.7. Kolmogorov length scales

Re	f	Model	η_k (m)	η_k (m) (approximation)
57	0	SAS	4.05E-04	1.49E-04
57	0	SBES	5.49E-04	1.49E-04
858	25	SAS	2.94E-05	1.96E-05
858	25	SBES	4.14E-05	1.96E-05
858	50	SAS	2.42E-05	1.96E-05
858	50	SBES	2.81E-05	1.96E-05
7150	50	SAS	4.02E-06	3.99E-06
7150	50	SBES	4.86E-06	3.99E-06

insights into the complex flow behaviors. For example, large scale vortex shedding can be seen, especially on the top side where the counterclockwise rotation pushes up the wake coming off the top-most cylinder. It would be expected then that the Strouhal number of the flow would be dictated by a frequency of three times of the rotational frequency,

$$St = \frac{3fD}{U_\infty}, \tag{7.13}$$

where f is the rotational frequency, D is arrangement diameter, and U_∞ is freestream velocity. The experiments of Ullah et al. contain data on the Strouhal number based on hotwire velocity measurements at three points in the cylinders' wake (Ullah et al., 2020). These points are shown in the description of the experiments in Figure 5.3.

Given the equation for Strouhal number developed, calculated St is compared to the experimental findings in Table 7.8. Error is calculated based off location A which was found to have the most consistent findings. This supports the premise that the largest flow structures within the flow which result from individual wakes of cylinders dictate the shedding frequency of the entire arrangement.

Table 7.8. Calculated vs. experimental Strouhal number

Re	f	St_{calc}	St_{ExpA}	St_{ExpB}	St_{ExpC}	% Error
858	25	0.220	0.225	0.225	0.225	2.23
858	50	0.440	0.450	0.450	0.450	2.23
7150	50	0.053	0.053	0.053	0.053	0

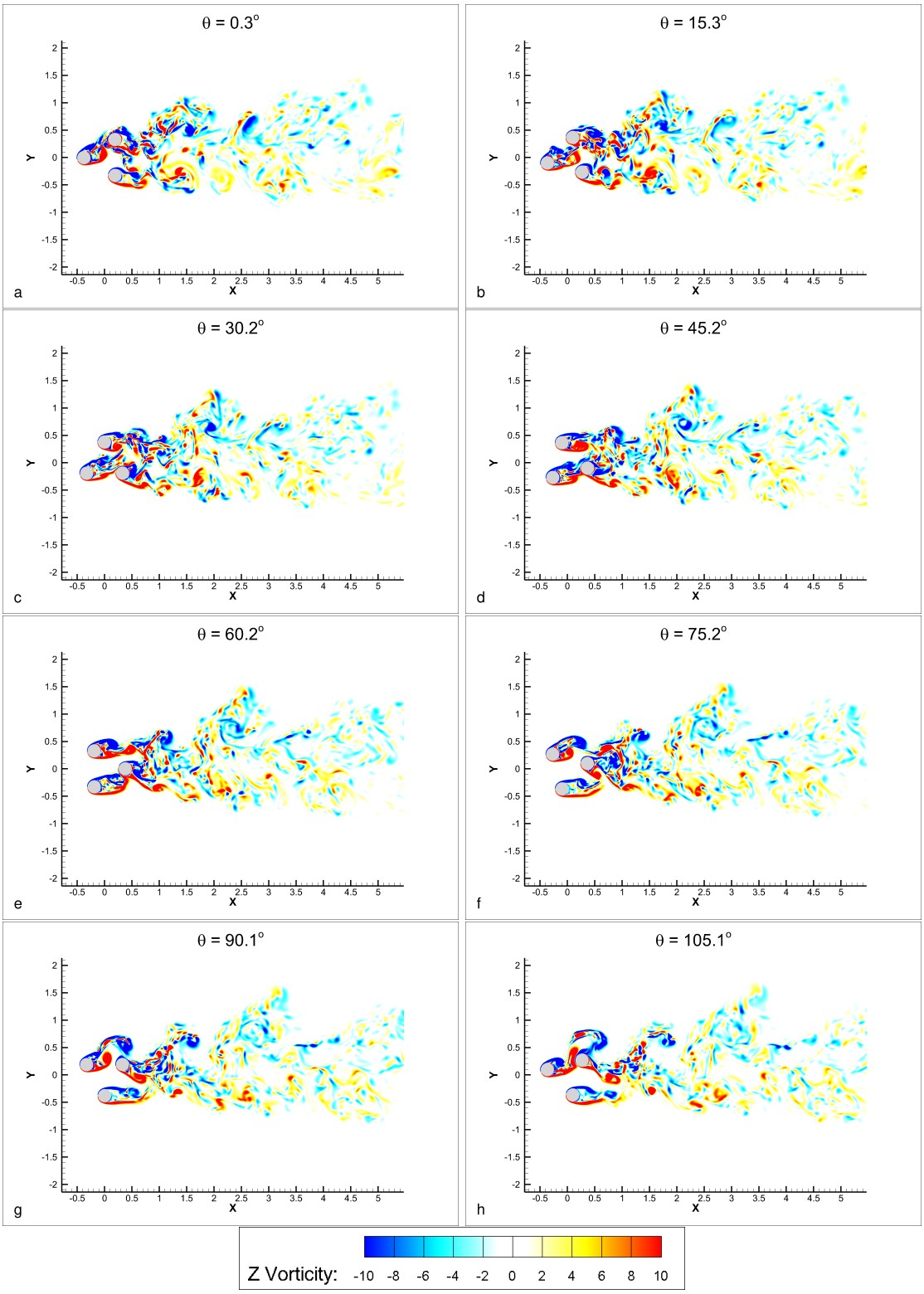

Figure 7.50. Instantaneous spanwise (Z) vorticity frames from $\theta = 0.3°$ to $\theta = 105.1°$ for Re=858, f=50 Hz, and SBES

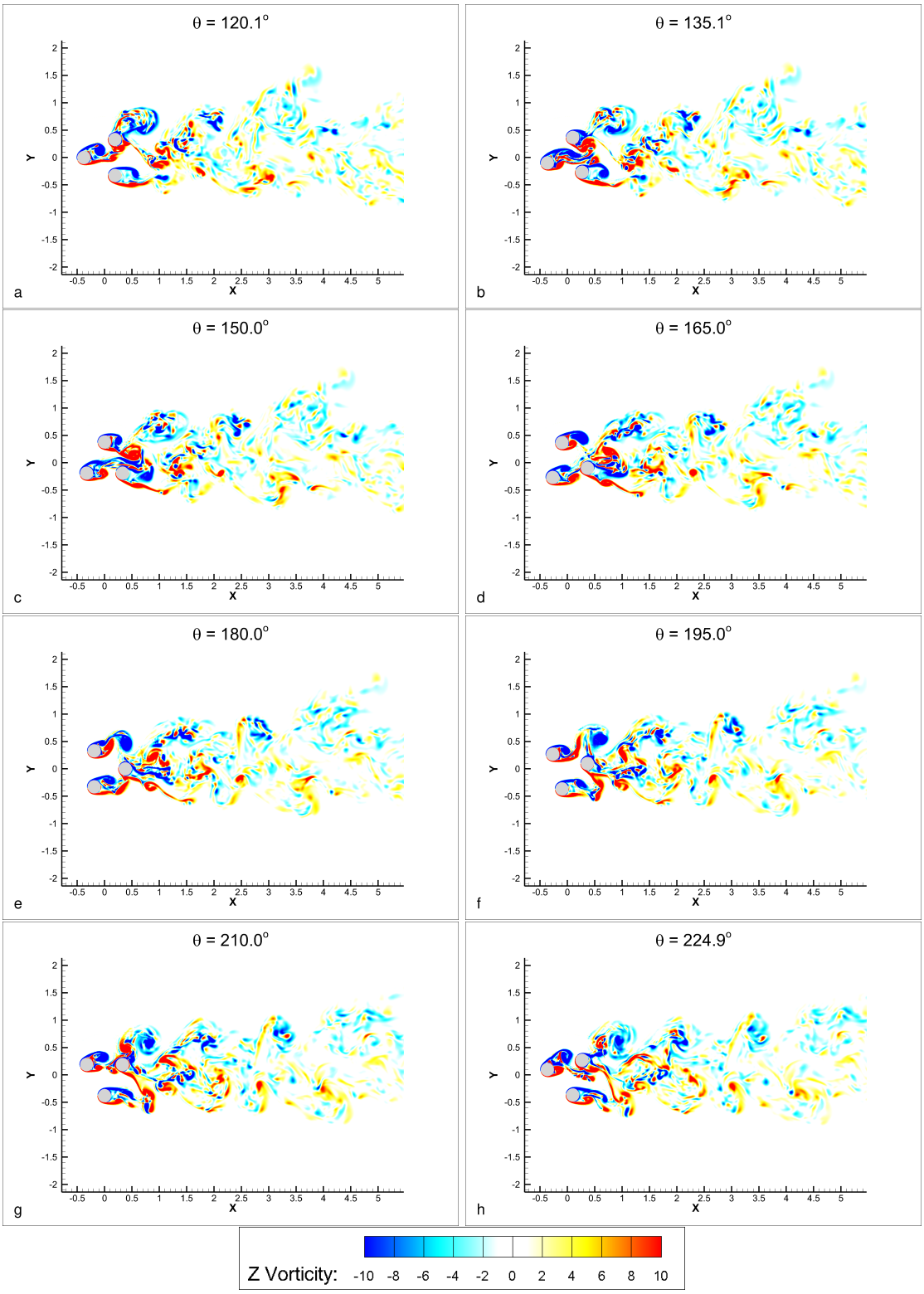

Figure 7.51. Instantaneous spanwise (Z) vorticity frames from $\theta = 120.1°$ to $\theta = 224.9°$ for Re=858, f=50 Hz, and SBES

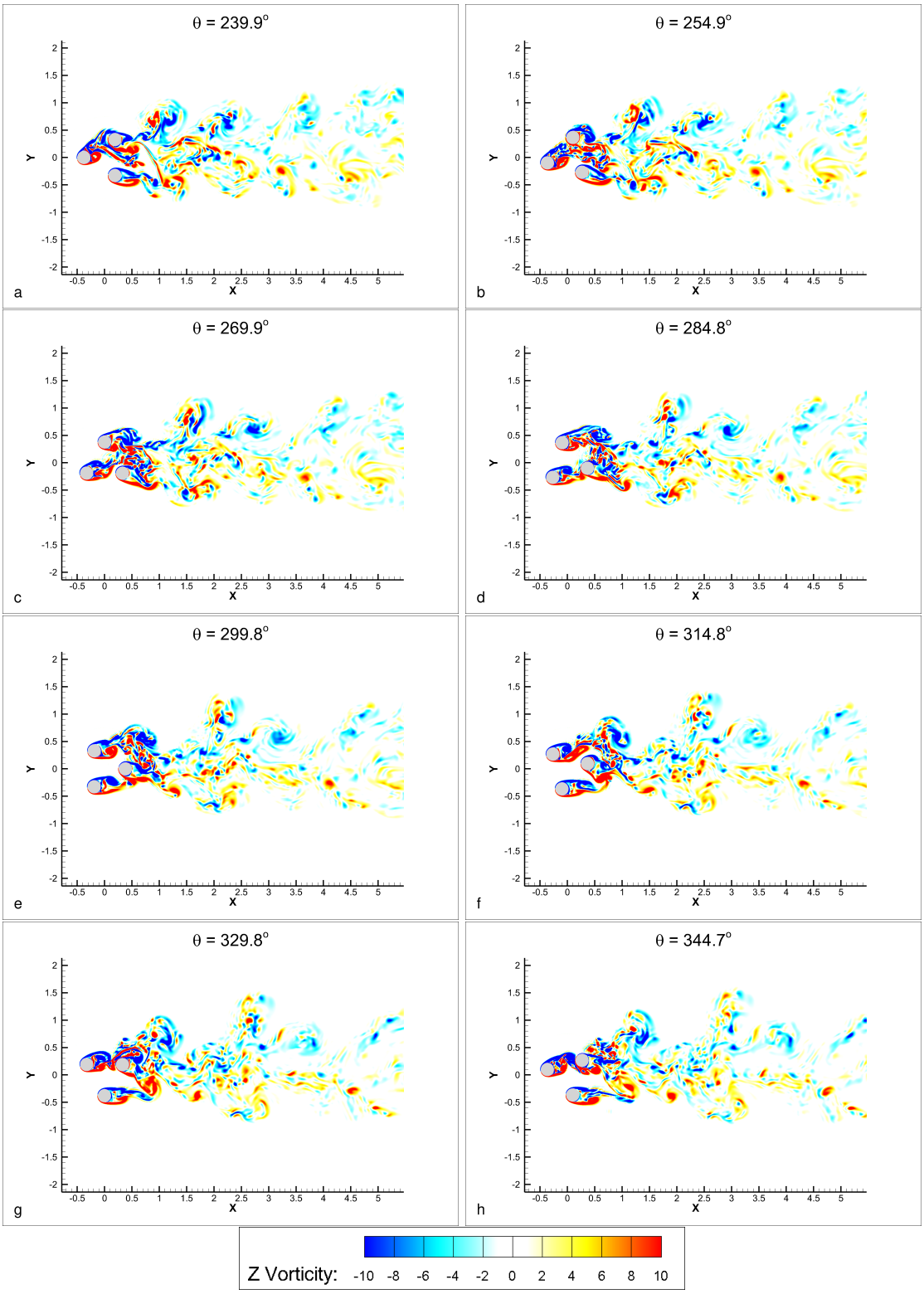

Figure 7.52. Instantaneous spanwise (Z) vorticity frames from $\theta = 239.9°$ to $\theta = 344.7°$ for Re=858, f=50 Hz, and SBES

In addition to this, Figures 7.50–7.52 show many of the 2D flow structures also found by Ullah et al. such as the spiraling arm vortices. Typically, at phases just after a cylinder was fully obstructed by another, the commonly rotating wakes align and begin to combine. For example, at $\theta = 45.2°$, the wakes of the two lower cylinders begin to mix and form a larger structure. Further downstream the mixing becomes much greater and harder to predict.

A commonly used parameter for identifying vortices is the Q-Criterion. Q-Criterion identifies vortices as regions of greater vorticity magnitude than strain-rate magnitude and is defined by

$$Q = C_Q(\Omega^2 - S^2), \tag{7.14}$$

where C_Q is a constant (C_Q=0.5 by default in Tecplot and is therefore used for this analysis), Ω is the vorticity magnitude, and S is the strain-rate magnitude (Tecplot, 2018). Q-Criterion easily shows the three-dimensionality of a flow or lack thereof. For example, Figure 7.53 shows Q-Criterion iso-surfaces for cases of $Re = 57$, $f = 0$ Hz. As expected and already determined from quantities such as $\overline{w'w'}$, 2D rollers are produced with negligible spanwise velocity.

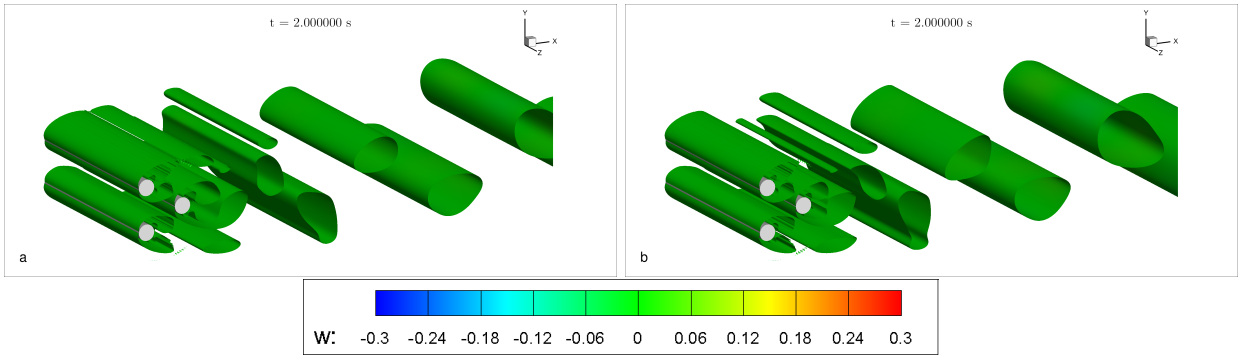

Figure 7.53. Q-Criterion iso-surfaces of $Q = 2$ colored by spanwise velocity for Re=57, f=0 Hz using a. SAS and b. SBES

It is far more interesting to view the Q-Criterion for three-dimensional turbulent flow. This can be useful in identifying broad flow patterns and Lagrangian coherent structures within a flow. The Q-Criterion is shown in Figure 7.54 for a $dZ = 0.5$ wide slice at the center of the domain. Circled are two of the large scale structures that shed from the top-most cylinder of the

arrangement. The rotation of the arrangement causes the wake of the "following" cylinder to push these structures vertically as the flow continues. This is magnified due to the fact that the wake shedding off the bottom of the topmost cylinder will be repelled by the anti-rotating wake off the top-most cylinder. For this instance, the wake shed from cylinder 3 will be repelled by cylinder 1 and pushed in the region of the circled structures. It is this behavior in repetition that likely contributes to the average velocity contours showing a wake slightly tilted upwards from the x-axis.

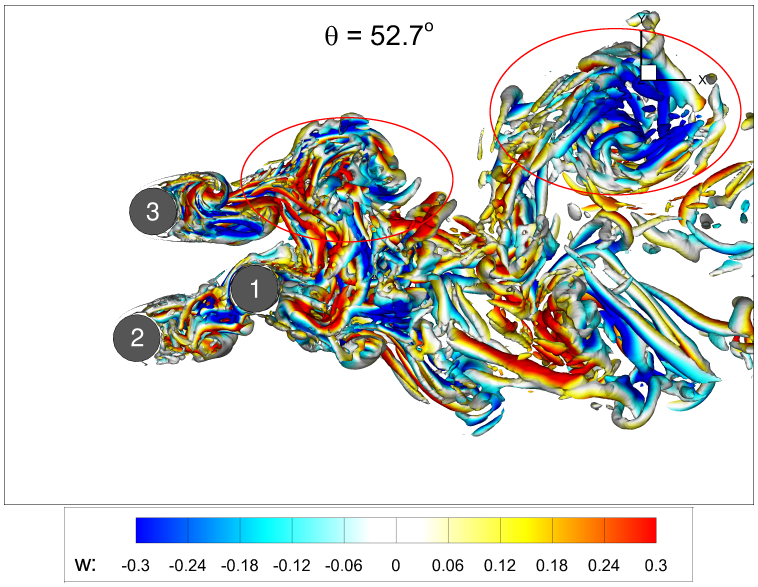

Figure 7.54. Q-Criterion iso-surfaces of $Q = 10$ colored by spanwise velocity for Re=858, f=50 Hz using SBES

Figure 7.55 shows Q-Criterion near the walls where the model transitions from RANS to SBES. Likewise, Figure 7.56 shows the SDES/SBES blending function at the center plane. In Figure 7.56, regions of red where $F_{SBES} = 1$ denote regions where RANS mode is in effect while blue areas where $F_{SBES} = 0$ show where LES is used to resolve scales. A short transition region exists in-between. This boundary is evident in Figure 7.55, which shows 2D sheets coming off the cylinders that transition into the formation of 3D scales. This is where the main differences of SBES and pure LES are clear; pure LES would resolve much smaller scales from the point of flow separation on the cylinder surfaces.

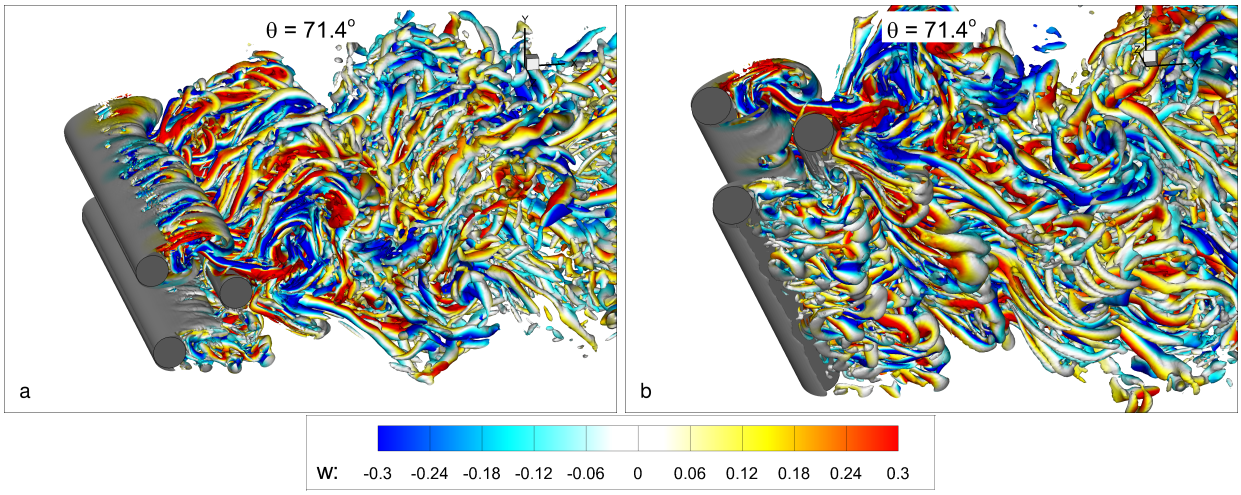

Figure 7.55. Q-Criterion iso-surfaces of $Q = 10$ colored by spanwise velocity near the cylinder walls for Re=858, f=50 Hz using SBES a. viewed from the top and b. viewed from the bottom

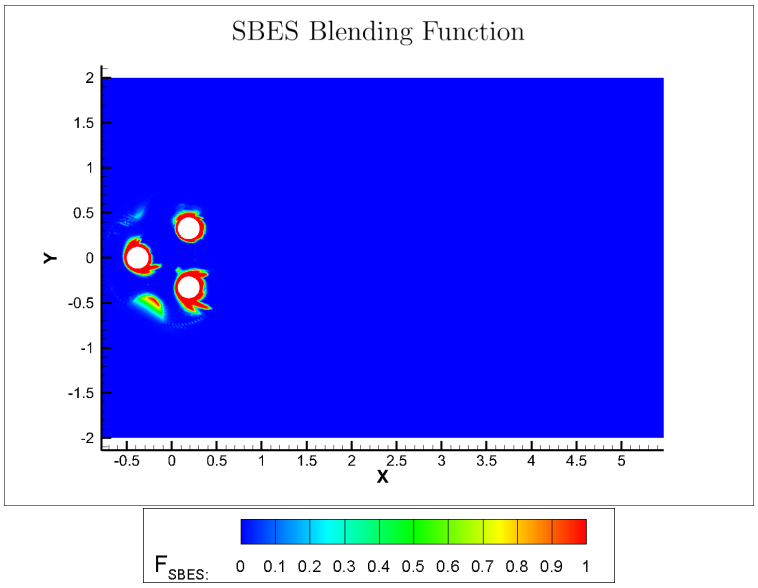

Figure 7.56. SDES/SBES blending function for Re=858, f=50 Hz

The Q-Criterion shows that the vortex structures in the flow are primarily streamwise tube-like structures. However, some additional structures can be identified. Figure 7.57 shows Q-Criterion looking up from the bottom of the arrangement. Large scale v-shape vortices can be seen in the circles shown (Ruiz et al., 2015). These are similar in structure to the streamwise vortex pairs observed by in experiments by Williamson et al. and in computations of Thompson et al. (Thompson et al., 1996; Williamson et al., 1995). These structures develop from instabilities in

the shear layer shed from the cylinders. Opposite signed spanwise velocity demonstrates the rotation of the structures' "legs". Figure 7.57b shows the vector field on a v-shape vortex structure.

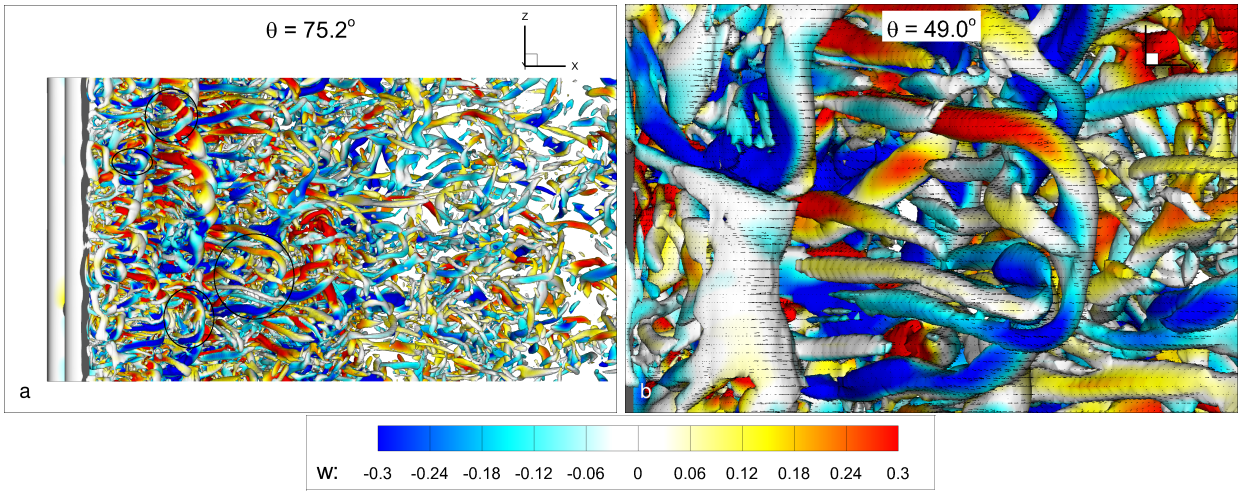

Figure 7.57. Q-Criterion iso-surfaces of $Q = 10$ colored by spanwise velocity near the cylinder walls for Re=858, f=50 Hz using SBES

Another structure found in the flow is a long spanwise structure such as that seen in Figure 7.58. This kind of structure is likely a remnant of a 2D roller that is shed from the cylinders that did not break into 3D structures such as the v-shape structures and the prevalent streamwise tubes. This could be due to a lack of shear or grid size not being fine enough, although it does show undulations within the structure suggesting that grid size is not the issue.

The high Reynolds number case, $Re = 7150$ and $f = 50$ Hz, is also shown in Figure 7.59. The higher Reynolds number results in much smaller scales being resolved and an even greater degree of mixing and complexity of the flow. That being said, large scale structures such as the von Kármán style vortices are still seen such as those circled in Figure 7.59. Shedding off the top-most cylinder is at a much higher frequency than that of three times the rotational frequency, yet the $3f$ frequency still dominates in the experiments' Strouhal number calculations. Looking back to the lift oscillations in Figure 7.46, these higher frequencies represent those from which the expected Strouhal number of ~0.2 are calculated, while the lower frequencies of $3f$ result in the lower Strouhal number calculated (keep in mind that the Strouhal numbers calculated from Figure 7.46 are based on single cylinder diameter).

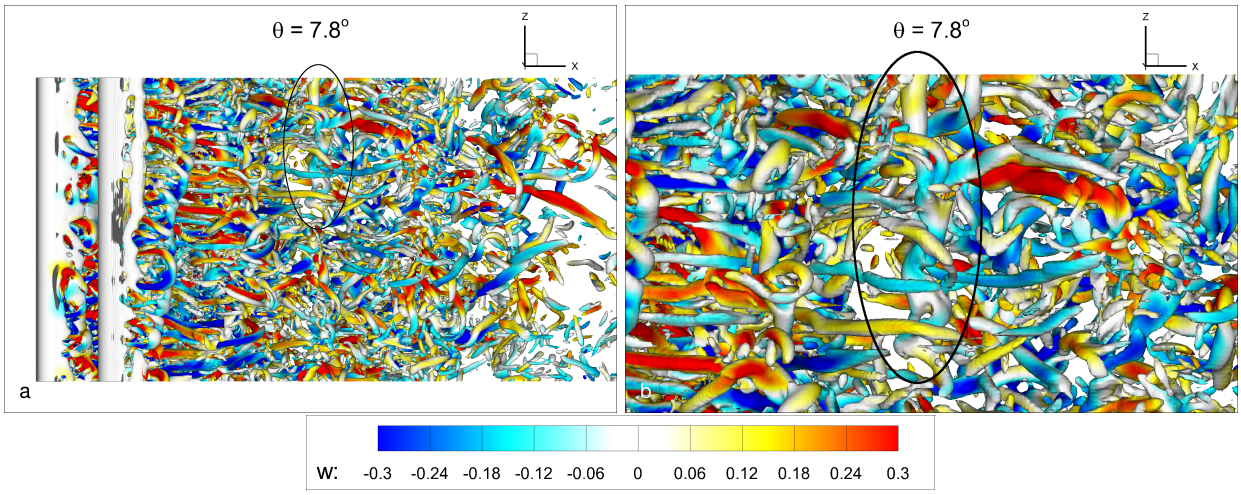

Figure 7.58. Q-Criterion iso-surfaces of $Q = 10$ colored by spanwise velocity for Re=858, f=50 Hz using SBES

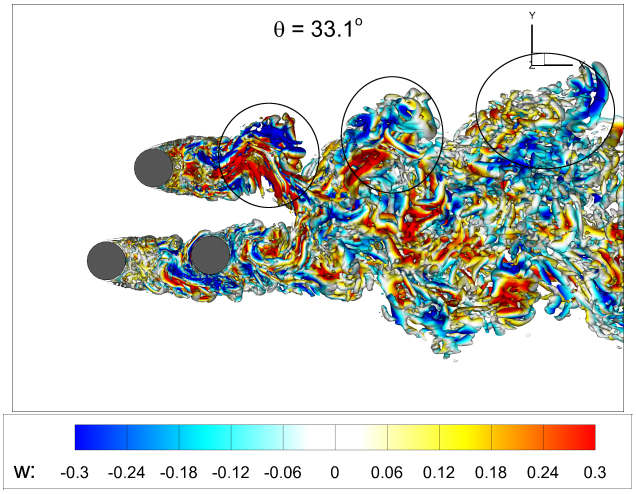

Figure 7.59. Q-Criterion iso-surfaces of $Q = 10$ colored by spanwise velocity for Re=7150, f=50 Hz using SBES

7.7. Computational Cost Analysis

As one of the primary reasons to use hybrid models is their efficiency, this study would not be complete without taking into consideration their computational cost. Table 7.9 outlines the cost of each run, both in total CPU hours and number of CPU hours per timestep. Note also the number of processors used for each run. The number of processors used varied slightly between runs, from 160 to 200. Parallel scaling is not linear and therefore the cost per timestep will be affected to some degree by this. In general, fewer processors are more efficient than more processors. In runs that were restarted from backups several times with a different amount of processors, a weighted

average of the processors is used, weighted using the amount of timesteps calculated with each number of processors.

Table 7.9. Computational cost analysis

Re	f	Model	Processors	Timesteps	$ (CPU Hours)	$/timestep
57	0	SAS	190	13,000	24,664	1.90
57	0	SBES	160	9,000	15,025	1.67
858	25	SAS	179	10,308	28,972	2.81
858	25	SBES	180	12,308	40,750	3.31
858	50	SST	200	19,702	27,888	1.42
858	50	SAS	180	10,770	26,972	2.50
858	50	SBES	180	10,770	43,750	4.06
7150	50	SAS	180	17,778	44,583	2.51
7150	50	SBES	179.5	17,778	161,944	9.11

First consider cases run with SAS. They have a relatively consistent computational cost as Reynolds number increases, ranging from 1.90 to to 2.81 over all cases. SBES sees a more significant increase in computational cost as Reynolds number increases, peaking at a cost of 9.11 at $Re = 7150$. At $Re = 57$, SBES is actually slightly more efficient—however this may be due to using less processors (160 vs. 190). It is expected that both models would be extremely comparable if not identical in cost when only their RANS modes are in use. Comparing SAS and SBES at $Re = 858$, there is not a significant difference in cost, with SBES being on average 40.1% costlier. Considering the benefits of resolving more turbulent scales with SBES, this is highly favorable at this Reynolds number. At $Re = 7150$, SBES is 3.63× more expensive than SAS. This demonstrates that at higher Reynolds numbers, the costs must be counted more carefully when selecting a model considering the desired outcomes and application of the study.

Considering that the same mesh is used for both models, it is interesting that such a difference in computational cost is seen between SAS and SBES. The reason for this is that SBES requires more iterations per timestep to converge, a factor that also increases with Reynolds number. While SAS requires 2–3 iterations per timestep to converge at both $Re = 858$ and $Re = 7150$, SBES increases from 3 iterations per timestep to 10 iterations per timestep from $Re = 858$ to $Re = 7150$.

Figure 7.60 plots the cost efficiency as a function of the Reynolds number (scaled logarithmically) for all the cases described. Note that the single SST case does show the lowest cost as

expected. As the only run using 200 processors, it is expected it would have been even more efficient at 180 processors. This can be considered as a baseline RANS model to compare the efficiencies of SAS and SBES.

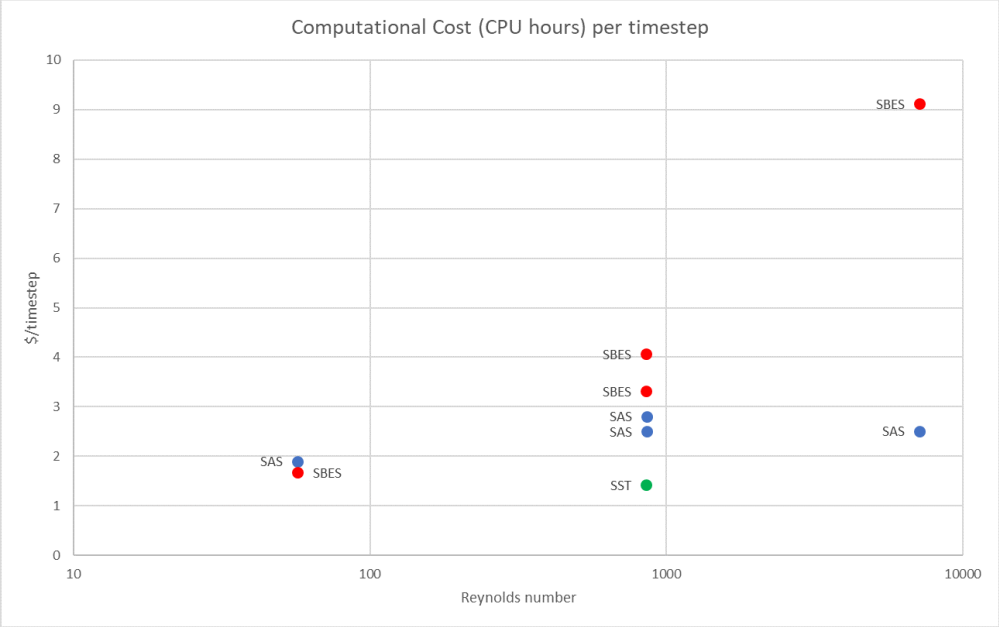

Figure 7.60. Computational cost vs. Reynolds number

8. CONCLUSIONS AND FUTURE WORK

8.1. Conclusions

Flow computations have been performed on the highly unsteady flow over an arrangement of three cylinders using SAS and SBES turbulence models. First and second order turbulence quantities of time-averaged velocity components and statistical Reynolds stress show good agreement with experimental results for both models. SBES shows better prediction of the Reynolds stresses which may be a result of it resolving more of the small scales present in reality. The Strouhal number of the individual cylinders throughout the rotation is very similar to the Strouhal number of a single cylinder in cross-flow. Comparison to a control case using the SST RANS model shows that SAS and SBES are superior both in average flow property predictions and instantaneous flow resolution.

The key difference in model performance is evident in comparing instantaneous quantities of vorticity, Q-Criterion, and so on. SBES is able to resolve more and smaller turbulence scales than SAS and results in a much more detailed solution. This makes it possible for detailed flow analysis almost on par with a LES solution which would not be possible with a RANS model or even SAS. From inspection of the major flow structures and comparison to the experimental results, the Strouhal number can be found as a function of the rotational frequency, $St \propto 3f$. Other structures identified include v-shape vortices as well as long spanwise vortices.

Finally, computational efficiency is comparable at low Reynolds numbers but SBES becomes significantly more expensive as the Reynolds number increases. SAS has a relatively constant computational cost for each Reynolds number while the cost of SBES increases somewhat linearly with the Reynolds number.

8.2. Future Work

While the WALE LES model used in SBES is capable of handling transition, it is typically shielded from performing within the boundary layer and therefore its transition capabilities are not utilized. One area to further improve upon the results in this study could be to implement the use of a transition model such as the $\gamma - Re_\theta$ model in conjunction with the SST model used in SBES.

Better prediction of the transition to turbulence could lead to more accurate results, albeit at the cost of an increase in computational time.

Running simulations for longer amounts of time would produce more reliable time-averaged quantities for comparison with the experiments. In addition, a longer time series would allow more reliable calculation of the Strouhal number, especially for the large scale fluctuations due to the von Kármán like shedding of the entire arrangement.

Finally, further analysis can be done into the turbulent flow structures found within the flow and describing them quantitatively. If found to be computationally feasible, a pure LES run could also be conducted to compare the structures produced, especially near the cylinders where the hybrid models start to resolve scales.

BIBLIOGRAPHY

ANSYS. (2017). *Ansys cfx-solver theory guide 18.2*. ANSYS, Inc.

Bao, Y., Zhou, D., & Huang, C. (2010). Numerical simulation of flow over three circular cylinders in equilateral arrangements at low reynolds number by a second-order characteristic-based split finite element method. *Computers & Fluids*, *39*(5), 882–899.

Choi, H., & Moin, P. (1995). Grid-point requirements for large eddy simulation: Chapman's estimates revisited. *Journal of Fluid Mechanics*, *299*, 35–71.

Davidson, L. (2020). *Fluid mechanics, turbulent flow and turbulence modeling*. Chalmers University of Technology.

Davidson, P. A. (2013). Elementary properties of turbulence. *Turbulence in rotating, stratified and electrically conducting fluids* (pp. 197–219). Cambridge University Press.

DeLeon, R. (2016). Turbulence modeling with large-eddy simulation.

for Computationally Assisted Science, C., & Technology. (2017). Introduction to thunder cluster.

Hinze, J. O. (1959). *Turbulence : An introduction to its mechanism and theory*. New York : McGraw-Hill.

Hoffmann, K. A., & Chiang, S. T. (2000). *Computational fluid dynamics* (4th ed., Vol. 3). Education Education System.

Lam, K., & Cheung, W. (1988). Phenomena of vortex shedding and flow intererence of three cylinders in different equilateral arrangements. *Journal of Fluid Mechanics*, *196*, 1–26.

Mayle, R. E. (1991). The role of laminar-turbulent transition in gas turbine engines. *Journal of Turbomachinery*, 509–537.

McDonough, J. M. (2007). *Introductory lectures on turbulence*. University of Kentucky.

Menter, F. R. (1994). Two-equation eddy-viscosity turbulence models for engineering applications. *AIAA Journal*, *32*(8), 1598–1605.

Menter, F. (2015). *Best practice: Scale-resolving simulations in ansys cfd* (Report No. 2.00). ANSYS Germany GmbH.

Menter, F. (2016). *Stress-blended eddy simulation (sbes) - a new paradigm in hybrid rans-les modeling* (Report). ANSYS Germany GmbH.

Menter, F., & Egorov, Y. (2005). A scale-adaptive simulation model using two-equation models. *AIAA*, *1095*.

Menter, F., Kuntz, M., & Bender, R. (2003). A scale-adaptive simulation model for turbulent flow predictions. *AIAA*, *0767*.

Menter, F., Kuntz, M., & Langtry, R. (2003). Ten years of industrial experience with the sst turbulence model. *Heat and Mass Transfer*, *4*.

Nicoud, F., & Ducros, F. (1999). Subgrid-scale stress modelling based on the square of the velocity gradient tensor. *Flow Turbulence and Combustion*.

Pope, S. B. (2000). *Turbulent flows*. Cambridge University Press.

Reynolds, O. (1883). An experimental investigation of the circumstances which determine whether the motion of water shall be direct or sinuous, and of the law of resistance in parallel channels. *Philosophical Transactions of the Royal Society of London*, *174*, 935–982.

Richardson, L. F. (1922). *Weather prediction by numerical process*. Cambridge, The University Press.

Rodriguez, S. (2019). *Applied computational fluid dynamics and turbulence modeling*. Springer.

Rostad, B. (2018). *Unsteady aerodynamics & turbulent near-wake characterization of static & rotating cylinder systems* (Master's thesis). North Dakota State University.

Ruiz, A. M., Lacaze, G., & Oefelein, J. C. (2015). Flow topologies and turbulence scales in a jet-in-cross-flow. *Physics of Fluids*, *27*.

Sinha, N. (2013). *Towards rans parameterization of vertical mixing by langmuir turbulence in shallow coastal shelves* (Doctoral dissertation). Argonne National Laboratory.

Strelets, M. (2001). Detached eddy simulation of massively separated flows. *39th AIAA Fluid Dynamics Conference and Exhibit*.

Sucker, D., & Brauer, H. (1975). Investigation of the flow around transverse cylinders. *Wärme- und Stoffubertragung*, *8*(3), 149–158.

Tatsuno, M., Amamoto, H., & Ishi-i, K. (1998). Effects of interference among three equidistantly arranged cylinders in a uniform flow. *Fluid Dynamics Research*, *22*(5), 297–315.

Tecplot. (2018). *Tecplot 360 ex user's manual* (2018 R2). Tecplot, Inc.

Tennekes, H., & Lumley, J. L. (1972). *A first course in turbulence*. MIT Press.

Thomas, N. L., Ullah, A. H., Suzen, Y. B., & Estevadeordal, J. (2021). Numerical simulations of flow past a three-cylinder rotating system using scale-adaptive simulation (sas) [Control ID 3455571]. *AIAA*.

Thompson, M., Hourigan, K., & Sheridan, J. (1996). Three-dimensional instabilities in the wake of a circular cylinder. *Experimental Thermal and Fluid Science*, *12*, 190–196.

Ullah, A. H., Fabijanic, C., & Estevadeordal, J. (2020). Advanced measurements and analyses of flow past three-cylinder rotating system [Reno NV (virtual)]. *AIAA Aviation*.

Ullah, A. H. (2020). *Advanced measurements and analyses of flow past three-cylinder rotating system* (Master's thesis). North Dakota State University.

White, F. M. (2006). *Viscous fluid flow* (3rd ed.). New York : McGraw-Hill.

Wilcox, D. C. (2006). *Turbulence modeling for cfd* (3rd ed.). DCW Industries.

Williamson, C. H. K., Wu, J., & Sheridan, J. (1995). Scaling of streamwise vortices in wakes. *Physics of Fluids*, *7*, 2307–2309.

Xiao, H., & Cinnella, P. (2019). Quantification of model uncertainty in rans simulations: A review. *Progress in Aerospace Sciences*, *108*, 1–31.

Zdravkovich, M. (1968). Smoke observations of the wake of a group of three cylinders at low reynolds number. *Journal of Fluid Mechanics*, *32*(2), 339–351.

Zilli, J., Sutton, D. M., & Lavoie, P. (2017). Effect of freestream turbulence on laminar separation bubbles and flow transition on an sd7003 airfoil at low reynolds number. *AIAA*, *0302*.